PHD DISSERTATION

Fracture Toughness of Thin Films Estimated by Rockwell C Indentation

by Mads Krabbe

AARHUS
UNIVERSITY

Fracture Toughness of Thin Films Estimated by Rockwell C Indentation

Fracture Toughness of Thin Films Estimated by Rockwell C Indentation

PhD Thesis by

Mads Krabbe

Aarhus University Department of Engineering, Denmark

AARHUS
UNIVERSITY
DEPARTMENT OF ENGINEERING

River Publishers

ISBN 978-87-93237-27-8 (e-book)

Published, sold and distributed by:
River Publishers
Niels Jernes Vej 10
9220 Aalborg Ø
Denmark

www.riverpublishers.com

Contents

Abstract

The work in this Ph.D. thesis focuses on analysis of indentation-induced fracture in hard, brittle thin films. A method for determining thin film fracture toughness from the cracking pattern arising from a Rockwell C indentation is proposed.

This thesis consists of three parts covering the work to develop the proposed fracture toughness test method.

Firstly, the stress in the film around the indentation is analysed. A number of theoretical solutions are investigated. The thin film stress state is determined by a finite element simulation of the indentation process. The simulation includes contact, nonlinear material behaviour, large strains and large displacements. The indentation process for both a bulk substrate and a film/substrate system is analysed. It is investigated if film bending has influence on the results. The influence of the indentation depth on the accuracy of the result is treated. Substrate plasticity and the effect of plasticity on the indentation depth and film stress state is also analysed.

Secondly, the driving mechanisms and important material parameters regarding crack propagation in thin films are described in detail. Relevant crack propagation models are presented and compared. The influence of substrate plasticity and crack spacing on crack propagation is investigated. During film cracking, bending of the film occurs. This effect is investigated and compared with literature models for crack spacing.

Thirdly, the indentation stress simulations and crack propagation models are coupled in order to create a model for determining the thin film fracture toughness. The influence of residual stress is described and illustrated. The model and the transition from crack propagation to crack arrest is illustrated. The model is tested on two different film/substrate systems, a TiN-ASP23 and an Al_2O_3-AISI 316L system. The crack patterns from these two systems are used to discuss the validity of the model.

Resumé

Denne Ph.D.-afhandling omhandler analyse af brud forårsaget af indentering i hårde, sprøde tyndfilm. I projektet foreslås en metode til at bestemme tyndfilmens brudsejhed ud fra det revnemønster, der opstår ved en Rockwell C indentering.

Afhandlingen består af tre dele, der beskriver processen med at udvikle den foreslåede test til bestemmelse af brudsejhed.

I den første del er spændingerne i filmen bestemt ved en finite element simulering af indeteringsprocessen i film/substrat-systemet. Simuleringen omfatter kontakt, ulineære materialeegenskaber, store tøjninger og store flytninger. Indenteringsprocessen er simuleret for to forskellige systemer; et homogent substrat og et film/substrat-system. Det er undersøgt, om bøjning af filmen har indflydelse på resultatet. Indeteringsdybdens indflydelse på nøjagtigheden af resultaterne er undersøgt. Det er undersøgt, om plasticitet i substratet har indflydelse på indenteringsdybden og spændingstilstanden i filmen.

Andel del består af en detaljeret beskrivelse og analyse af de bestemmende mekanismer og vigtige materialeparametre for revnevækst i tyndfilm. Relevante modeller for revneudbredelse er beskrevet og sammenlignet. Indflydelsen fra plasticitet i substratet og revneafstand på revnevæksten i filmen er undersøgt. Når filmen revner, opstår der bøjning i filmen. Dette fænomen er undersøgt og sammenlignet med modeller fra litteraturen.

I del tre er filmspændingerne og revnevækstmodellerne koblet for at konstruere den foreslåede model til bestemmelse af brudsejhed i tyndfilmen. Egenspændinger i filmen har indflydelse på resultatet og denne indflydelse er illustreret. Selve modellen og overgangen fra revnevækst til hvor revnen standser er illustreret. Modellen er testet på to forskellige film/substrat-systemer; en TiN film på et ASP23 værktøjsstål-substrat og en Al_2O_3 film på et AISI 316L rusfrit stål-substrat. Modellens gyldighed er diskuteret ud fra revnemønstret i disse to systemer.

Preface

This thesis is submitted in partial fulfilment of the requirements for obtaining the Ph.D. degree at the Department of Engineering, Aarhus University. The Ph.D. project is a part of the project *Optimal Mechanical Properties of Nano-Composite Hard Coatings*. The project is founded by the Danish Research Council for Technology and Production Sciences and carried out as a collaboration between the Department of Engineering (ENG) and the Interdisciplinary Nanoscience Center (iNANO) at Aarhus University in the period April 1 2010 to July 31 2014. The coordinator of the project is Henrik Myhre Jensen who is also the supervisor on the present Ph.D. project.

First of all, I would like to thank my supervisor, Henrik Myhre Jensen for invaluable guidance, support and motivation during my Ph.D. project. His door is always open and Henrik's advice on solutions and the aim for the project has been of great help.

Also thank you to Postdoc, Ph.D. Nis Dam Madsen, previously iNANO, for providing indentation micrographs for the work.

I would like to thank Professor Sc.D. Michael Thouless for giving me the opportunity to visit him at the Department of Mechanical Engineering at the University of Michigan. This stay was a big experience to me.

A big thank you to my colleagues and fellow Ph.D. students at the Department of Engineering, Aarhus University. A special thank to Søren Steffensen, Jens Wind and Per Hyldahl, who I have shared offices with. You have provided a friendly atmosphere and been the cause of many good talks, both of professional and social character.

Last but not least a very big thank you to my wife Bente for support and understanding during my project. All the support you have given me during long working hours, especially for the last six months, has been truly outstanding.

Aarhus, July 31, 2014
Mads Krabbe

List of symbols

Latin symbols

a	Crack length, plane strain crack
$b_0 \dots b_3$	Constants for radial displacement model
b_{beam}	Beam width
$b_{blister}$	Blister half-width
$\bar{b}$	Burgus vector
B	Blister field strength
c	Crack length, channelling crack
C_1	Nondimensional function of Dundur's parameters
D_δ	Dundurs' original 1st parameter
D_η	Dundurs' original 2nd parameter
E	Young's modulus
E_b	Beam Young's modulus
E_f	Film Young's modulus
E_s	Substrate Young's modulus
$E*$	Reduced Young's modulus
$\bar{E}_f$	Film plane strain Young's modulus
$f(\sigma_{ij})$	Yield surface isotropic hardening
F_{close}	Crack closure force
f_d	Densification factor
$f_1 \dots f_4$	Constants describing blister field strength
f_ω	Factor describing fracture toughness mode dependence
F	Film load
$g(\alpha, \beta)$	Nondimensional crack driving factor for elastic mismatch
G	Crack energy release rate
G_{tip}	Energy release rate for crack kinked out of interface
G_{ps}	Plane strain crack energy release rate
$\mathcal{G}_{del}$	Delamination crack steady state energy release rate
$\mathcal{G}_{ss}$	Channel crack steady state energy release rate
h	Film thickness, beam height
h_c	Critical film thickness
$h*$	Characteristic length for strain gradient plasticity
H	Indentation hardness
H_0	Infinite indentation depth hardness, strain gradient plasticity
H_v	Vickers hardness
k_t	Plasticity threshold value

K_I	Mode I stress intensity factor
K_{II}	Mode II stress intensity factor
l	Characteristic length for crack interaction, elastic mismatch
l_{huang}	Characteristic length for strain gradient plasticity
L	Crack spacing
L_0	Crack spacing at crack initiation
L_1	Crack spacing at crack arrest
$L_{min,yield}$	Minimum crack spacing, shear lag
L_{slip}	Slip length
L_{wafer}	Wafer length
m	Beam fundamental length
M	Film delamination moment
$M(x)$	Beam bending moment
n	Strain-hardening exponent in FEM power law
$\bar{n}$	Exponent describing load distribution, elastic contact
N	Strain hardening exponent in the Ramberg-Osgood relation
$p(r)$	Contact pressure
p_0	Indentation pressure at the edge of the contact
p_m	Mean contact pressure
P	Indentation force
q	Stress singularity exponent
R_i	Indentation radius
s_{crack}	Crack opening surface, VCCT
s_{ij}	Stress deviator
$\tilde{s}_{ij}$	Effective stress deviator
t	Factor describing residual stress
$T_{substrate}$	Substrate thickness
u_r	Radial displacement
u_θ	circumferential displacement
U	Strain energy
W	work done by uniform crack opning pressure
Z	Cracking number

Greek symbols

α	Dundurs' 1st parameter
β	Dundurs' 2nd parameter
γ_{ij}	Value of stress tensor in the centre of yield surface
Γ_2	Fracture toughness for bulk material
Γ_{del}	Interface fracture toughness
Γ_{del}^{I}	Mode I fracture toughness
Γ_f	Film fracture toughness
δ	Indentation depth
δ_c	Crack opening displacement
δ_{ij}	Kronecker delta
δ_n	Crack node opening displacement, VCCT
Δ	Integral of crack opening displacement
ϵ	Strain
ϵ	FEM output strain matrix
ϵ_{rr}	Radial strain, axisymmetric case
ϵ_{rz}	Shear strain, axisymmetric case
$\epsilon_{\theta\theta}$	Circumferential or hoop strain, axisymmetric case
ζ	Empirical factor, strain gradient plasticity
$\kappa_{analytical}$	Analytical wafer curvature
κ_{FEM}	FEM wafer curvature
λ_{equi}	Equilibrium crack spacing
λ_{min}	Minimum crack spacing
Λ	Ratio of shear moduli
$\mu_1, \mu 2$	Shear modulus for material 1 and 2
ν	Poisson's ratio
ν_f	Film Poisson's ratio
ν	substrate Poisson's ratio
ξ_1, ξ_2	Quantity describing Poisson's ratio, Dundurs' parameters
ρ	Indenter cone semi-angle
σ	Normal stress
$\sigma_{0,critical}$	Critical residual stress
σ_{arrest}	Crack arrest stress
σ_c	Buckling delamination critical stress
σ_f	Film stress, shear lag
σ_{ij}	Stress tensor
σ_r	Normal radial stress, line load
σ_{rr}	Radial stress, axisymmetric case
σ_y	Yield strength

σ_{xx}	normal stress x direction
σ_θ	Normal circumferential stress, line load
$\sigma_{\theta\theta}$	Circumferential or hoop stress, axiasymmetric case
$\tilde{\sigma}_{ij}$	Effective stress tensor
τ	Shear stress
$\tau_{r\theta}$	Shear stress, line load
τ_y	Interface shear yield stress
χ	Beam loading wavelength
$\hat{\chi}$	Wave length for stress distribution, shear lag analysis
ψ	Relation between K_I and K_{II}
ω	Mode mixture phase angle
Ω	Crack kink angle

Chapter 1

Introduction

1.1 Surface engineering

Surface treatment is a term that covers a wide range of surfaces produced by many different processes and techniques. The technological development has created a demand for surfaces with specialised properties. Modern surface technology has also made it possible to create structures in cheaper or more convenient materials and use surface treatment to create the specific desired properties. Modern surface treatment has also made it possible to detach the bulk material properties from the surface properties. This makes it possible to choose materials with favourable properties regarding manufacturing processes, price etc. and then choose an appropriate surface treatment to obtain the necessary properties regarding appearance, corrosion, wear, electrical or thermal insulation etc.

This approach where the surface of the component is an integrated part of the final part and its function is termed surface engineering and is a key competitive resource within numerous industries ranging from car production to electronic devices and chemical industry components.

Surface treatment is a common name for a larger number of different processes that satisfies very varying requirements. These treatments include, for instance (Møller, 2003; Møller and Pleth, 2013):

- Organic coatings including paint
- Chemical and electrochemical coatings
- Thermal spray coatings
- Hot-dip galvanizing coatings
- Diffusion coatings and hardened surfaces

- Physical and chemical vapour deposited coatings

1.2 Thin films

In this current thesis, thin films are seen as a subset of the general term surface coatings. Here, the term thin films is used to describe surface coatings with a thickness which typically lies in the range $0.01 - 100\mu m$. These types of coatings are typically produced by physical (pvd) and chemical vapour deposition (cvd) techniques or thermal spray techniques. These types of thin coatings have a broad range of applications and is crucial to the function of a wide range of different components.

A large area af application is the electronic industry. Technological development has created a demand for thin materials of high quality, reproducible properties and high reliability for use in miniature integrated electronic circuits. In these kinds of devises, correct confinement of electronic charges relies largely on interfaces between materials with different electronic properties. Thin films are integral parts of many micro-electromechanical systems (MEMS). Devices based on thin film technology are used as microphones in hearing aids, pressure sensors etc. Another common example is a normal computer hard disk. A hard disk is a multilayer system typically consisting of a aluminium disc coated with a nonmagnetical nickel-phosphor coating. On top of this is added a chrome layer followed by the actual magnetic storage layer and at the surface, a low friction amorphous carbon layer is added. A typical hard disk rotates with $5400 - 7200rpm$ and the reader head is moving at a distance of $50nm$ over the surface. This yields high demands for the tolerances and uniformity of the hard disk surface.

Thin film are also widely used to enhance the mechanical integrity or protect the underlying substrate. Thermal barrier coatings (TBC) is a major area of application. TBC's are used to isolate metallic structure from high surface temperatures and are for instance used to protect turbine blades in power plant gas turbines and aeroplane jet engines. The extremely high temperature gradients and constant temperature cycling between high and low temperature set high requirements to a wide range of coating properties (Freund and Suresh, 2004).

A broad range of different coatings are used to improve the mechanical strength of substrate materials. This is typically to enhance the wear properties of the final components. Types of applications are numerous. Cutting tools such as hard metal plates, drills, milling tools and punching tools are often coated to improve their lifetime. Plastic moulding tools can

also be target for considerable abrasive wear and the lifetime can be greatly enhanced by coating the tool. Specific types of thin films can be tailored to exhibit low friction coefficients. These films are used e.g. in deep drawing tools, shafts, bearings and in gears. These examples are areas where low friction coefficients are crucial to improve the performance or lifetime of the coated component.

For the two last mentioned examples, the mechanical properties of the coatings are of paramount importance to obtain the desired performance. It is of key interest to have accurate knowledge of the mechanical properties of the coatings in order to describe and optimize coating performance and production process parameters. To fully understand the wear properties of thin films, precise knowledge of both hardness, elastic properties and fracture toughness are of key importance. Extracting material properties of these thin films is not a simple task. Due to the small size scale of the films, normal material characterisation methods such as tensile testing and normal hardness measurement methods cannot be used. However, well-established and commonly used methods for determining hardness and elastic modulus has been established by (Oliver and Pharr, 1992). The thin films are often ceramic coatings, for instance titanium nitride (TiN), aluminium oxide (Al_2O_3) and chromium nitride (CrN) (Møller and Pleth, 2013). These types of coatings have properties similar to ceramic solids, meaning that they are brittle and often fail by the propagation of cracks. For that reason, the fracture toughness is an important parameter for the coating performance. It is a hypothesis that the wear properties are linked to the crack patterns that form during loading of the thin films. Thus, the focus of this thesis is to analyse the fracture mechanisms of thin, hard, brittle films.

1.3 Fracture toughness estimation

Fracture toughness measurement for bulk materials rely on well-established methods such as three- or four-point bending, tensile test of compact tension specimens etc. These conventional testing methods has proven not to be suitable for thin film testing due to the small size scale of the films and the fact that the thin film properties are dependent on the deposition parameters and the substrate properties.

A number of different methods to determine thin film fracture toughness has been proposed during the years. Recently, (Zhang and Zhang, 2012) has summarised most of these methods in a review paper.

As previously described, determination of Young's modulus and hardness is done by load and displacement sensing indentation at low loads. Experimental results has shown that the initiation and formation of a crack is traceable in the load-displacement curve of the indenter response. These traces are referred to as "kink" or "pop-in" events (Malzbender and de With, 2000; Weppelmann and Swain, 1996; Whitehead and Page, 1992). A sketch of a pop-in event is seen in figure 1.1. The general approach is to extract

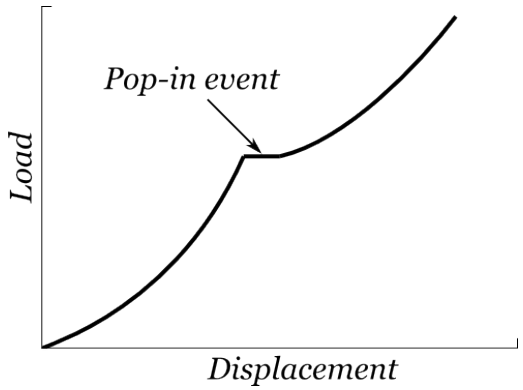

Figure 1.1: Sketch of pop-in event in load displacement curve from an instrumented nanoindentation

the energy dissipated by fracture and the crack area to obtain the fracture energy per fractured area which is the fracture toughness Γ_f. However, the extraction of the fracture energy is controversial and a number of approaches has been suggested, see for instance (Chen and Bull, 2009; Li et al., 1997; Michel et al., 2006). Furthermore, the discontinuity seen in figure 1.1 may not be present or may be difficult to identify. If a clear identification of the load plateau is not possible, this method cannot be used.

Most fracture toughness estimation methods for thin films are concentrated around fracture patterns caused by nano-indentations. Figure 1.2 shows two different examples of crack patterns arising from nanoindentations. A method for determining fracture toughness from radial cracks as seen on figure 1.2a has been proposed and established by (Evans and Charles, 1976), originally for bulk materials. This method has been investigated in numerous cases analysing different crack geometries, influence of film thickness, etc., see for instance (Jang and Pharr, 2008; Pharr, 1998; Thurn and Cook, 2004). Generally, it is difficult to obtain crack depths small enough compared to the thin film thickness. In general, the crack depth should be much less that 10% of the film thickness h in order to use the methods developed for bulk materials. Other difficulties are issues such

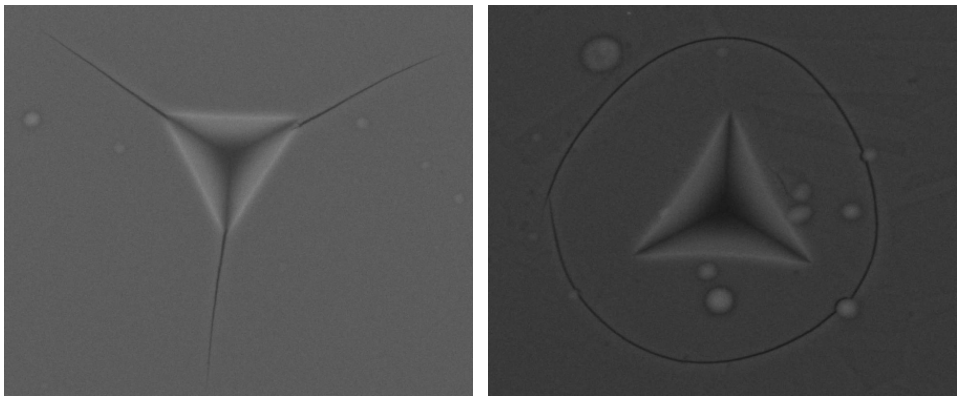

(a) Radial cracks (b) Circumferential crack

Figure 1.2: Top view of radial and circumferential cracks initiated during nanoindentation using a Berkovich and conical indenter respectively

as determination of crack geometry, substrate influence and the contact mechanics close to the indentation.

The crack pattern seen on figure 1.2b is not as widely investigated but has been examined by (Abdul-Baqi and Van der Giessen, 2002). Very recent work (Steffensen and Jensen, 2014; Steffensen et al., 2013) investigates this crack pattern further and shows promising results.

A different type of test where separate strips of thin film is deposited on the side of a beam is investigated by (Wang et al., 1998). By applying a four-point bending test on the beam, the film strips are exposed to different loads and the film fracture toughness can be determined.

1.4 Fracture toughness estimation from a Rockwell indentation

Common for all the mentioned methods is that they require specialised test samples or nanoindentation equipment. Specialised test samples must be prepared separately and require extra work in the deposition process. Nanoindentation equipment is sophisticated equipment that requires special skills to operate. Thus it is desirable to have methods that can be performed on standard metallurgical laboratory equipment.

The scope of this work is to develop and describe a method for determining fracture toughness of a hard, brittle coating on the basis of the fracture pattern caused by a Rockwell indentation of the film/substrate system. A

number of advantages by using a Rockwell indentation exists.

Rockwell indentation is today already an industry-used method for qualitatively characterisation of the adhesion of hard coatings, (Ver, 1992; Vidakis et al., 2003), see figure 1.3. Here, the adhesion is determined by

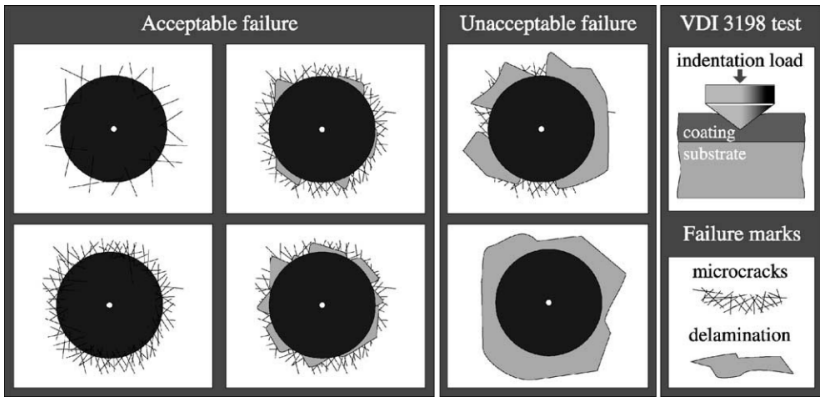

Figure 1.3: Principle of the VDI 3198 adhesion test

the failure image after a Rockwell C indentation. None or little spallation corresponds to an acceptable result. As can be seen on figure 1.3, the failure image for an acceptable failure contains microcracks spreading from the indentation crater edge. An example of theses cracks can bes seen on figure 1.4. Since Rockwell indentation is a well implemented part of

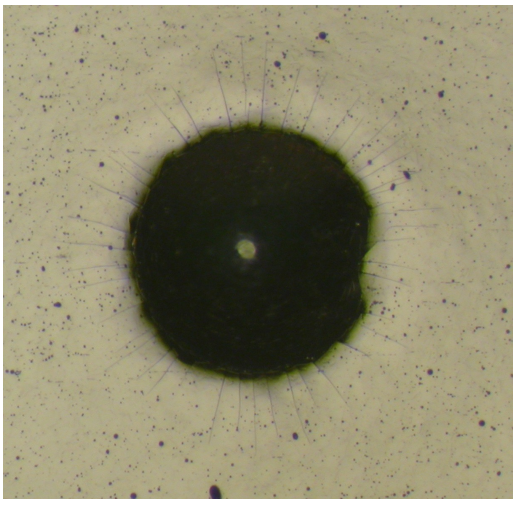

Figure 1.4: Indentation microcracks from a Rockwell indentation

the characterisation procedure for hard coatings, the equipment is already

widely used today. Also, a Rockwell indenter is standard equipment in metallurgical laboratories. Being able to use this simple equipment for fracture toughness determination would be a great advantage from the expensive and sophisticated nano indentation equipment used today.

The work necessary to implement this analysis method can be divided into three parts. These three parts form the overall structure of this thesis.

- Firstly, an accurate model for the stresses in the film is necessary. The analysed fracture pattern shows radial cracks spreading out from the indentation crater. The driving force for the thin films is thus caused by the circumferential or hoop stress in the film caused by the indentation. The model must be accurate in the range from $R_i \leq r \leq R_i + c$, where R_i is the radius of the indentation crater and c is the crack length. A number of relevant theoretical models are described to realise how accurate they are in the given situation. A numerical model based on the finite element method (FEM) for the indentation is described and used to obtain the thin film hoop stresses. The FEM model includes nonlinearities such as contact, large displacement, large strains and plasticity.

- Secondly, the fracture mechanics of long cracks in thin films is described. Governing cracking mechanisms is described and analysed. In a thin film system, the thin film and the substrate interacts and thus the material properties of both the film and the substrate must be taken into consideration, these factors are described. A key factor is the interaction of cracks propagating in dense, parallel arrays. The influence of these factors on the crack driving force is described and investigated further. A number of relevant models for crack propagation is described and compared.

- Thirdly, the indentation stresses and the crack driving mechanisms are combined in order to analyse the crack pattern arising from the Rockwell indentation crater. The influence of residual stresses in the film is discussed. The model stated is tested using experimental results and the validity of the model and the results is discussed.

Part I

Determination of film stresses

Chapter 2

Theoretical solutions for indentation stresses

2.1 Introduction

In this chapter, a number of theoretical models for stress and displacements around an indentation is covered to realise how accurate they are in the given situation.

2.2 Elastic solutions

2.3 Point loading of an elastic half-space

A first approach is to look at stresses and displacement in a semi-infinite, elastic half-space loaded by a normal point load. Firstly, an elastic half-space loaded by a line load is described. The boundary of the half-space lies in the $x - y$ plane and the z axis points into the solid. The loaded line lies parallel to the y axis as seen on figure 2.1. The expression presented here is on base of (Johnson, 1987) and (Timoshenko and Goodier, 1951). The problem was originally solved by (Flamant, 1892). Plane strain is assumed in the given expressions. Timoshenko and Goodier derives the solution from Airy's stress function. The solution is typically presented in a polar coordinate system as shown in figure 2.1. The stress in the half-space is given by

$$\sigma_r = -\frac{2P}{\pi}\frac{\cos\theta}{r} \tag{2.1}$$

$$\sigma_\theta = \tau_{r\theta} = 0 \tag{2.2}$$

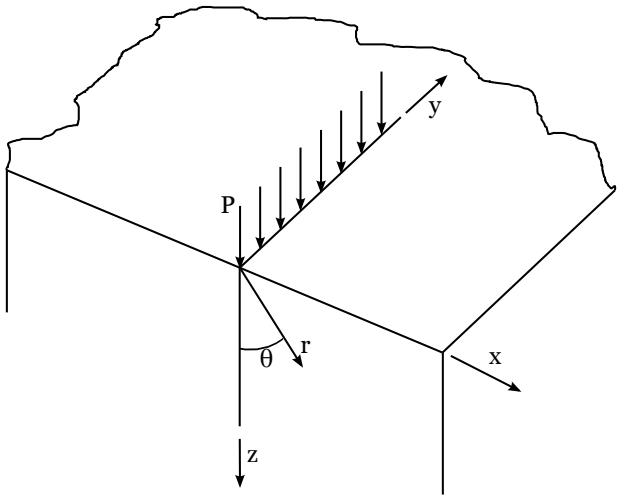

Figure 2.1: Line load of elastic semi-infinite half space

The stress distribution is this case is called a "simple radial distribution" and every point in the solid at a distance r from the point of application is subject to a simple compression in the radial direction given by equation 2.1. The stress has a $1/r$ dependence and thus decays when moving away from the point of application. The surface displacements in the horisontal x direction is given by

$$u_{r|\theta=\pi/2} = -\frac{(1-2\nu)(1+\nu)P}{2E} \tag{2.3}$$

$$u_{\theta|\theta=\pi/2} = -\frac{1-\nu^2}{\pi E} 2P \ln\left(\frac{r_0}{r}\right) \tag{2.4}$$

Where r_0 is the distance to a datum point on the surface (or the vertical axis below the load).

More relevant in this case is the axisymmetric case of a point load on a semi-infinite elastic half-space, see figure 2.2. The solutions given here is given from (Johnson, 1987) and (Timoshenko and Goodier, 1951). The problem was originally solved by (Boussinesq, 1885) who has given name to the problem: The Boussinesq problem or Boussinesq solution.

Timeshenko and Goodier finds a solution for Airy's stress function for the case of a point load in an elastic half-space. They use polar coordinates to describe the axi-symmetric stresses from a concentrated normal load acting on the surface on a linear elastic, isotropic half-space. At the surface

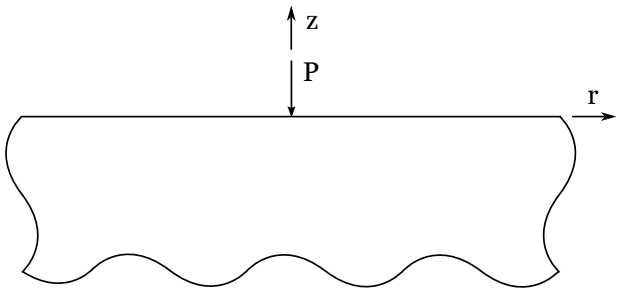

Figure 2.2: Sketch of the axisymmetric Boussinesq problem

the stresses are given by:

$$\sigma_{rr|z=0} = \frac{P}{2\pi}(1-2\nu)\frac{1}{r^2} \tag{2.5}$$

$$\sigma_{\theta\theta|z=0} = -\frac{P}{2\pi}(1-2\nu)\frac{1}{r^2} \tag{2.6}$$

$$\sigma_{zz|z=0} = 0 \text{ for } r \neq 0 \tag{2.7}$$

Where P is the normal load, ν is Poisson's ratio and r is the distance from the point load. This stress distribution is different from the distribution obtained by the plane strain case. Generally the stresses show a $1/r^2$ dependence instead of the $1/r$ dependence for plane strain. Also, at the surface, the radial stresses are positive. (Timoshenko and Goodier, 1951) derives the strains from the stresses and integrates to find the displacements. On the surface these are given by

$$u_{r|z=0} = -\frac{(1-2\nu)(1+\nu)}{2\pi E}\frac{P}{r} \tag{2.8}$$

$$u_{z|z=0} = \frac{(1-\nu^2)}{\pi E}\frac{P}{r} \tag{2.9}$$

The hoop stress distribution given by equation 2.6 can be seen on figure 2.3. As can be seen both from equation 2.6 and figure 2.3 the hoop stress approaches zero at a large distance from the load. The hoop stresses reaches a theoretically infinite negative value at the centre and is negative for all values of r.

Other elastic solutions for indentation

Stresses and displacements caused by normal pressure applied to a region instead of a simple point load are also considered. Two types of loading

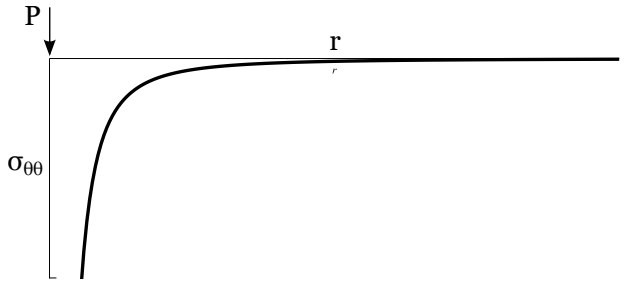

Figure 2.3: Hoop stress distribution from Boussinesq stress function

is analysed, uniform pressure and Hertz pressure. Both types of pressure distributiosn can be described by the expression (Johnson, 1987)

$$p(r) = p_0(1 - r^2/R_i^2)^{\bar{n}}, \quad r \leq R_i \tag{2.10}$$

For uniform pressure distribution $\bar{n} = 0$. The radial surface displacements within the loaded area are given by

$$u_{r|z=0} = \frac{(1-2\nu)(1-\nu)}{2E} p(r) \cdot r, \quad r \leq R_i \tag{2.11}$$

Where R_i is the radius of the loaded region. The total load of the loaded region P is, for a uniformly loaded region, given by $P = p_0 \pi R_i^2$. At the indentation boundary, $r = R_i$, and expressed in terms of P instead of p, $u_{r|z=0}$ is given by

$$u_{r|z=0,r=R_i} = -(1-2\nu)(1+\nu)\frac{P}{2\pi E R_i} \tag{2.12}$$

For Hertz contact conditions $\bar{n} = \frac{1}{2}$. Here, the radial displacements are given by

$$u_{r|z=0} = -\frac{(1-2\nu)(1+\nu)}{3E}\frac{R_i^2}{r} p_0 \left\{1 - \left(1 - \frac{r^2}{R_i^2}\right)\right\}, \quad r \leq R_i \tag{2.13}$$

The total load of the circular region can be expressed as $P = \frac{2}{3}\pi p_0 R_i^2$. At the edge of the contact region, $r = R_i$, and using that $p_0 = (3P)/(2\pi R_i^2)$, the radial displacements for $r = R_i$ ca be written as

$$u_{r|z=0,r=R_i} = -(1-2\nu)(1+\nu)\frac{P}{2\pi E R_i} \tag{2.14}$$

which is the same as for a uniform pressure, equation 2.11. This shows that for these two cases of elastically loaded circular region, the displacements of

the contact edge are identical to equation 2.8. This means that for uniform and Hertz pressure distribution, the radial displacements at the contact edge is the same as if the entire load was concentrated at the centre of the circle as given by the Boussinesq solution. By superposition it follows that this holds for all cases axisymmetric pressure distributions in the loaded circle. This is also true for the radial surface displacements outside the loaded area which are given by

$$u_{r|z=0} = \frac{(1-2\nu)(1+\nu)}{2E}\frac{P}{\pi r}, \quad r > R_i \tag{2.15}$$

With $P = p\pi R_i^2$ for a uniform pressure distribution and $P = \frac{2}{3}\pi p_0 R_i^2$ for Hertz pressure distribution.

The hoop stresses are linked to the radial displacements as shown i equation 2.6. Since the radial surface displacements outside the loaded area for all elastic cases can be expressed by equation 2.8, this means that the hoop stress distribution for all elastic cases is similar to figure 2.3. It can be seen that pure elastic theory states that the hoop stresses are negative at the surface for all values of r. For the case of radial cracks spreading from the indentation edge this is clearly not the case. Since the case is axisymmetric, the cracks must be formed by a positive $\sigma_{\theta\theta}$. This means that elastic contact theory is not suitable to describe the stress distribution in the indentation case.

Model for a beam lying on an elastic substrate

The film-substrate system can also be treated as an elastic beam resting on an elastic foundation with modulus E_b. The film is presented by a rectangular beam with height h and width b_{beam}. This system was investigated by (Biot, 1937). Here, the elastic foundation is treated as an continuous, elastic half-space. This differs from the simpler Winkler-foundation model in which the foundation is modelled as individual springs with a stiffness k. The Winkler foundation model assumes that the reaction of the foundation on the beam is dependent only of the local deflection in that specific point. The Biot model is more realistic since the reaction force at a specific point is a function of the deflection of all points at the foundation surface.

The solution method of the Biot problem is derived from the elementary solution of an elastic half-space loaded by a sine-wave load. A beam is considered and assumed to be loaded by two sine wave loads, a load on the top surface and a reaction load on the bottom surface. The reaction is then assumed to be caused by a sine-wave deflection of the substrate. Combining the solutions for the sine-wave loaded elastic half-space and the beam gives

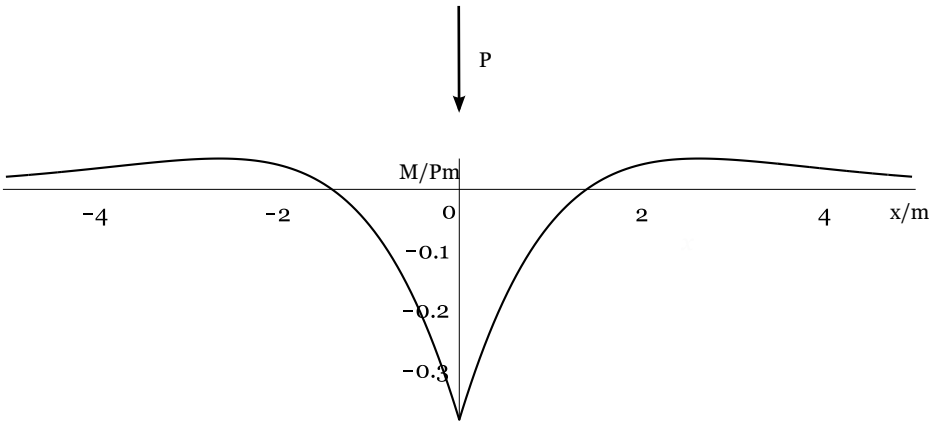

Figure 2.4: Moment distribution in a beam on an elastic foundation

the deflection and moment for the beam resting on the elastic half-space. To obtain the solution for a point load, the principle for the sine-wave loading is used and the point-load is represented by a Fourier-series. The beam bending moment is then given by

$$M(x) = Pm\frac{1}{\pi}\int_0^\infty \frac{\chi\cos\left(\chi\frac{x}{m}\right)}{\chi^3+1}d\chi \tag{2.16}$$

Here, m is a defined fundamental length of the beam. For a rectangular beam representing the film, m is given by

$$m = \left(\frac{1}{12}\right)^{1/3} h\left(\frac{E_b}{E_s}\right)^{1/3} \tag{2.17}$$

Where E_b and E_s is the Young's modulus of the beam and foundation respectively. The moment distribution can be seen in figure 2.4 and is radically different from the distribution for a point load on a simply supported beam. The moment has a local maximum at a distance $x/m \approx \pm 2.5$. For large absolute values of x/m the moment approaches zero. It is also seen that m is proportional to the film thickness h and to the cube root of the relation of the moduli of the beam and foundation. The local maximum for the bending moment is a very plausible location for a circumferential crack to propagate in the film due to the large bending. For low indentation depths, this may be used in a qualitative analysis of the location for this circumferential crack. In analyses of circumferential crack spreading at low indentation depths, the solution may be very useful. See for instance (Steffensen et al., 2013) for analysis of this type of cracks.

The Biot solution is not investigated any further for a number of reasons. The problem analysed in this work is for very large indentation depths and

information at the indentation crater edge and thus very close to the load is needed. The Biot solution does not represent this realistically. Also, for the very large indentation depths analysed in this work, bending is negligible. This is shown previously by (Drory and Hutchinson, 1996) and will be investigated further in the current work.

2.4 Fully plastic indentation

For most metals, the relation between Young's modulus and yield strength E/σ_y is large. When indenting material with large E/σ_y, the rigid-perfectly plastic indentation theory is typically used (Johnson, 1970a). The material is described as perfectly plastic above a threshold value k_t and rigid elsewhere. The plastic zone is assumed incompressible. To the describe this, the slip-line method is often used and the indentation problem has been described for a number of different geometries (Atkins and Tabor, 1965; Hill et al., 1947; Lockett, 1963). Focus in these analyses is on hardness determination on basis of the indentation mean pressure and indenter geometry. (Lockett, 1963) has solved the axisymmetrical problem of cone indentation. This solution gives values for the axial displacement of the piled-up area outside the indenter. The radial displacements are not treated in the solutions and no readily usable solution is available for the radial displacement.

2.5 Elastic-plastic indentation of cone

The most common used analytical model for describing elastic-plastic indentation is the "expanding cavity" model by (Johnson, 1970b). The model is based on the model of (Hill, 1950). The model describes the elastic-plastic indentation by describing the indenter to be enclosed in a spherical core with hydrostatic pressure. This plastic sphere replaces the spherical cavity described by Hill. Outside the hydrostatic stressed sphere is an infinite, elastic region. The hoop stress in the elastic-plastic region is here presented by the model proposed by (Yoffe, 1982). This model combines the displacement from the point load, (Boussinesq, 1885), with the displacements arising from a "blister field". The blister field represents the displacements and stresses arising from the plastic core. These combined gives:

$$u_{r|z=0} = \frac{-P}{2\pi Er}(1+\nu)(1-2\nu) + \frac{B}{Er^2}4(1+\nu)(1-\nu) \tag{2.18}$$

Using Hooke's law, the hoop stress can be expressed as

$$\sigma_{\theta\theta|z=0} = -\frac{P(1-2\nu)}{2\pi r^2} + \frac{B}{r^3}4(1-2\nu) \tag{2.19}$$

The first term with the $1/r$ dependence arises from the Boussinesq field and the second term with the $1/r^2$ dependence arises from the blister field.

It can be seen that far away from the indenter, the $1/r^3$ term vanishes and the solution converges towards the Boussinesq solution.

The quantity B describes the strength of the blister field, i.e. how much influence the plastic deformation has on the stress state in the indented solid. Yoffe determined that for a soda-lime glass and a cone semi-angle of 70°, $B = 0.06 p_m R_i^3$, where p_m is the mean contact pressure. However, the scope of the article by Yoffe was ceramic materials and the results are not directly applicable to ductile metals. Yoffe discusses the difficulty of ariving at a single value for the blister field strength.

(Cook and Pharr, 1990) also discuss the fracture mechanics of glass and ceramics by quantifying B. They propose the following expression for B

$$B = 0.026 f_d E \left(\frac{P}{H}\right)^{3/2} \tag{2.20}$$

Where f_d is a densinfication factor with $f_d = 0$ for the indentation volume completely accomodated by densification of the material and $f_d = 1$ for no densification. Again, the aim of the work is on cracking of ceramics and not ductile materials. Also, practical issues of determining the size of f_d arises.

(Bobji and Biswas, 1996) uses an energy argument to determine the blister field strength B. They propose that the energy put into the system by indentation can be separated in two parts. One part is dissipated in the plastic core giving rise to large-scale permanent deformations. The second part goes to elastically straining the elastic material outside the plastic core. Determining the size of these two parts and equation them to the total energy put into the system gives a expression for determining B:

$$\begin{aligned} f_4 \left(\frac{B}{HR_i^3}\right)^2 - f_3 \frac{B}{HR_i^3} + f_2 + f_1(2 - \cot(\alpha)) \\ -\frac{\pi^2}{3}\frac{1-\nu}{4}\frac{E}{2(1-\nu)H}\frac{\cot(\rho)}{\pi} = 0 \end{aligned} \tag{2.21}$$

Where ρ is the indenter cone semi-angle and H is the indentation hardness, $P/(\pi R_i^2)$. The constants $f_1 \ldots f_4$ are functions of ν. For $\nu = 0.33$, $f_1 = 0.13285$, $f_2 = 0.84744$, $f_3 = 2.80481$, $f_4 = 17.8426$.

2.6 Strain gradient plasticity

The indentation causes elastic-plastic response of the substrate. Conventional plasticity theories do not include material length scales (Fleck and Hutchinson, 1997). These theories associate the flow stress at a particular point with the strain exclusively in this point. It is unrelated to any strain gradient that might be present in the material.

When the size scale becomes very small, a size effect is observed and strain gradient effects cannot be neglected. A number of experiments demonstrate this phenomenon. (Fleck et al., 1994) performed tension and torsion experiments on pure copper wires with the diameter varying in the range from 12 to 170μm. In pure tension, no strain gradient is present in the wires. In torsion, the shear stress τ varies with the radius r from the centre of rotation and a strong size dependence was seen on the stress response of the twisted wires. In pure tension only minor size dependency in seen.

The influence of indentation depth on the measured hardness was investigated by (McElhaney et al., 1998). The work focused on the influence of pile-up and sink-in but a strong dependence on hardness by indentation depth is also observed. The results can be seen in figure 2.5 This phenom-

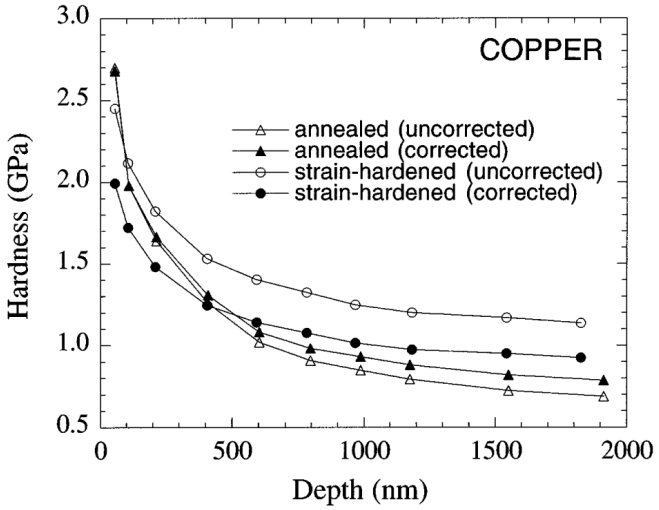

Figure 2.5: Hardness vs indentation depth for varius materials and correction terms (McElhaney et al., 1998)

ena is also observed by others, (De Guzman et al., 1993; Ma and Clarke, 1995).

(Nix and Gao, 1998) proposes a model for the depth dependence of indentation hardness

$$\frac{H}{H_0} = \sqrt{1 + \frac{h^*}{\delta}} \tag{2.22}$$

Where H is the hardness for a given indentation depth, H_0 is the hardness in the limit of infinite indentation depth and δ is the indentation depth The quantity h^* is a characteristic length depending on the indenter geometry, the shear modulus and H_0. The proposed model shows excellent correlation with earlier reported results from (Ma and Clarke, 1995; McElhaney et al., 1998).

(Nix and Gao, 1998) determines the characteristic length h^* for cold worked polycrystalline Cu to $h^* = 0.464\mu m$. Using this material constant and solving equation 2.22 for δ and setting $H/H_0 = 1.01$, i.e. the difference between H and H_0 to one percent, gives $\delta = 23\mu m$. This means that for indentation depths higher than $23\mu m$ strain gradient plasticity has no influence. The results shown in figure 2.5 implies that the influence of strain gradient plasticity may be negligible for much lower indentation depths.

(Huang et al., 2000) gives a characteristic material length for strain gradient plasticity

$$l_{huang} = 3\left(\frac{\zeta E}{2(1+\nu)\sigma_Y}\right)^2 \bar{b} \tag{2.23}$$

Where ζ is a empiric material constant in Taylor's dislocation model and $\bar{b}$ is the Burgers vector. For copper, typical values in equation 2.23 are $E/(2(1+\nu)\sigma_Y) = 200$, $\alpha = 0.4$, $b = 0.255nm$ and l_{huang} is approximately $5\mu m$. When the characteristic length of the deformation field (here the indentation depth) is much larger than l_{huang}, strain gradient plasticity is negligible.

In the present analysis, the indentation depth simulated is in the range of $100h$ meaning that δ has a size of hundreds om microns. This means that strain gradient plasticity is neglected in the present study.

Strain gradient plasticity may also play a role in other scenarios where large plastic strain gradients can be present, for instance at crack tips (Fleck et al., 1994). This phenomena is not investigated further in the current study.

Chapter 3

Numerical indentation model

3.1 Introduction

A numerical model has been created to analyse the contact problem of indentation in a substrate and a film/substrate system. Here, the general-purpose finite element code MSC.Marc is used. The indenter and crack pattern analysed is axisymmetric and thus an axisymmetric analysis is performed.

3.2 Literature models

Numerical analyses of film/substrate system have been widely used in order to understand the stress state in the film and the extend of the plastic zone beneath the indenter (Abdul-Baqi and Van der Giessen, 2002; Fischer-Cripps et al., 1996; Michler, 2001; Steffensen et al., 2013; Weppelmann and Swain, 1996). However, in analyses of film/substrate systems, the indentation depth is usually in same order of magnitude as the film thickness. In the present work, the indentation depth is much greater than the film thickness and results of the type stated are not applicable. FEM analyses of high-load indentation processes also exists. The Brinell indentation has been simulated by (Biwa and Storåkers, 1995; Hill et al., 1989). A closed-form polynomial approximation is given by (Hill et al., 1989), but not for the Rockwell indentation problem analysed here. A Brinell indentation of a film/substrate system is analysed by (Begley et al., 1999). The emphasis in the work by Begley et al. is on determination of the radial strain beneath the indenter which is not the focus for the current work. FEM analyses are also used for three-dimensional simulation of sliding contact, (Holmberg, 2008).

A numerical simulation of the Rockwell indentation process has been performed by (Drory and Hutchinson, 1996) to investigate delamination of a diamond-coated titanium alloy. The elastic-plastic material is described by a uniaxial Ramberg-Osgood relation given by

$$\epsilon = \frac{\sigma}{E_s} + \frac{3}{7}\frac{\sigma_y}{E_s}\left(\frac{\sigma}{\sigma_y}\right)^N \tag{3.1}$$

Where E_s is the substrate Young's modulus, σ_y is the yield stress and N is the strain hardening exponent. For the large indentation depth simulated, it is assumed that the influence of the film on the overall response of the indentation is negligible and the film is not simulated in the FEM calculations. It is also shown that film bending has insignificant influence on the results. Drory and Hutchinson gives a closed-form, polynomial approximation to the radial displacements in the film for a number of different material properties. The approximation is accurate in the range $2 \leq r/R_i \leq 5$ as this is the area of interest in the delamination analysis. In current project however, a detailed and accurate representation in the entire range from the indentation edge and outwards if necessary.

3.3 Present FEM model

Since existing solutions for surface displacements and stresses for a Rockwell indentation has proven insufficient to describe the problem in detail, an FEM model is developed to simulate the indentation problem. The general-purpose finite element code MSC.Marc is used. The indentation depth is set to 100 times the film thickness h. To capture this behaviour, a large deformation and large strain nonlinear procedure (updated Lagrangian) is used. This is done to capture the nonlinear effects that inevitable arise due to contact, large deformations and plasticity.

The substrate material is set to be elastic-perfectly plastic. Conventional plasticity theory is applied and no significant difference between kinematic and isotropic hardening is observed. This will be described in more detail.

A Rockwell C indenter geometry is chosen, that means a cone with a 120° cone angle and a 200 μm tip rounding.

An illustration of the model used can be seen in figure 3.1. The problem is analysed as an axisymmetric problem. A section of film with thickness h is bonded to the substrate. The contact radius denoted R_i and δ is the indentation depth. The constitutive models for the film-substrate system are chosen so the film is treated as perfectly elastic and the substrate is modelled as a elastic-perfectly plastic material. Both substrate and film are

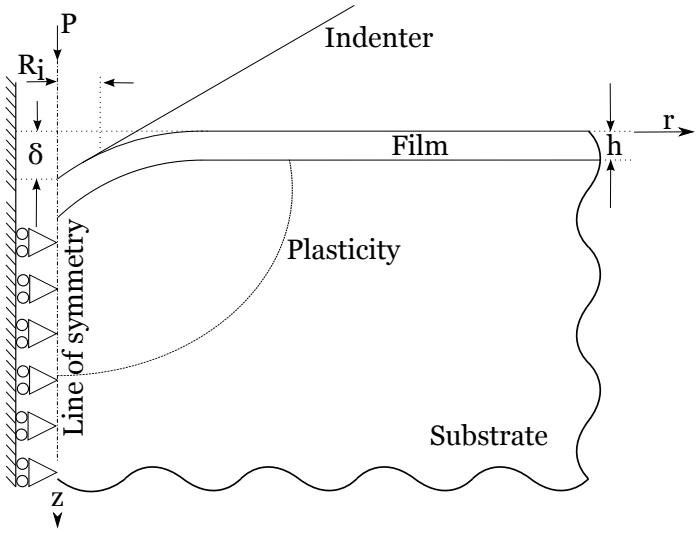

Figure 3.1: Illustration of the ued FEM model

treated as isotropic, without defects and with no residual stresses. Since delamination is not an object for investigation the film is perfectly bonded to the substrate in the analysis.

The elements used in the analysis are four-node, isoparametric, quadrilaterals for axisymmetric applications. Since geometry, loads and boundary conditions all are axisymmetric, nothing varies in the θ direction and the bimaterial system has radial, r, direction and axial z displacement only. Thus, the output strain matrix is

$$\boldsymbol{\epsilon} = \begin{bmatrix} \epsilon_{rr} & \epsilon_{rz} & 0 \\ \epsilon_{rz} & \epsilon_{zz} & 0 \\ 0 & 0 & \epsilon_{\theta\theta} \end{bmatrix} \tag{3.2}$$

The mesh is refined towards the indentation area in order to be able to capture the stress concentration near the indenter. In order to be able to get detailed informations of the through-thickness stress variations in the film, the film mesh is kept refined through the entire film length. Since very large indentation depths are simulated, an adaptive remeshing algorithm is implemented. This is done to avoid highly distorted or collapsed elements in the substrate beneath the indenter. The built-in Msc.Marc remeshing algorithm is used. Remeshing is done regarding to element distortion.

A convergence study is performed to ensure that element size does not affect the results. Also, a sensitivity study regarding boundary effects have

been conducted in order to ensure these effects do not influence the stresses in the areas of interest.

The typical indentation depth for the Rockwell indentation as seen in figure 3.2 is very large compared to the film thickness. Given this fact, it

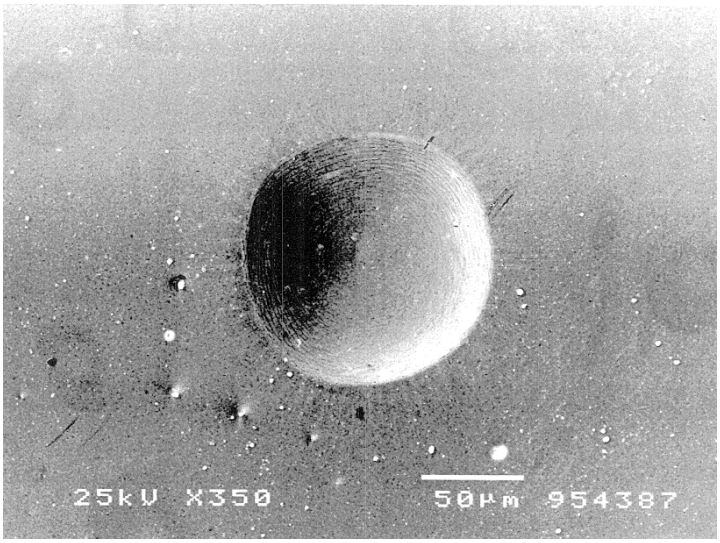

Figure 3.2: $10kg$ Rockwell A indentation of $2\mu m$ TiN on tool steel (ASP23) indentation radius is approx $60\mu m$ (Thomsen, 1998)

is assumed that the film thickness h is much smaller than the indentation radius R_i and the substrate thickness $T_{substrate}$. Under this assumption the circumferential stress can be calculated by

$$\sigma_{\theta\theta}(r) = \frac{E}{1-\nu^2}\left(\frac{u_r(r)}{r} + \nu\frac{du_r(r)}{dr}\right) \tag{3.3}$$

Where $u_r(r)$ is the radial displacement of the substrate at the interface. The displacement u_r is a function of r, the radial distance from the indentation centre. Two properties follow from the assumption $h \ll R_i$ and enables the use of the expression in equation 3.3 to describe the circumferential stress. Firstly, when the film is thin compared to the indentation radius and substrate thickness, it is a reasonable assumption that the displacement of the film equals the displacements of the substrate without the film. Secondly, the contribution to the elastic energy in the film caused by bending can be ignored (Drory and Hutchinson, 1996). Equation 3.3 determines the film stresses from the substrate displacements. This makes the method useful for systems with dissimilar stiffness for film and substrate. If there is no elastic mismatch between film and substrate, results for $\sigma_{\theta\theta}$ can also be used if available.

3.4 Results

Comparison and validation

As a validation, the newly developed FEM model is compared with (Drory and Hutchinson, 1996). The results from Drory and Hutchinson are reproduced with the given expression

$$\ln\left(\frac{u_r}{R_i}\right) = b_0 + b_1\left(\frac{r}{R_i}\right) + b_2\left(\frac{r}{R_i}\right)^2 + b_3\left(\frac{r}{R_i}\right)^3 \tag{3.4}$$

Where the constant $b_0 \dots b_2$ are given for different values of strain hardening exponent N and normalised yield strength σ_y/E. Here, the values chosen are $N = 10$ and $\sigma_y/E = 0.005$. The nonlinear material models in MSC.Marc does not directly include the option for choosing a Ramberg-Osgood relation. Instead, at perfect elatic-power law scheme is chosen. Here, the material is elastic up until the yield point. The post-yield strain hardening behaviour is described by a power law of the type

$$\sigma = \frac{\sigma_y}{(\sigma_y/E)^n)}\left(\sigma_y/E + \epsilon\right)^n \tag{3.5}$$

Where n is a parameter describing strain-hardening.

The results can be seen on figure 3.3. The results are very similar until

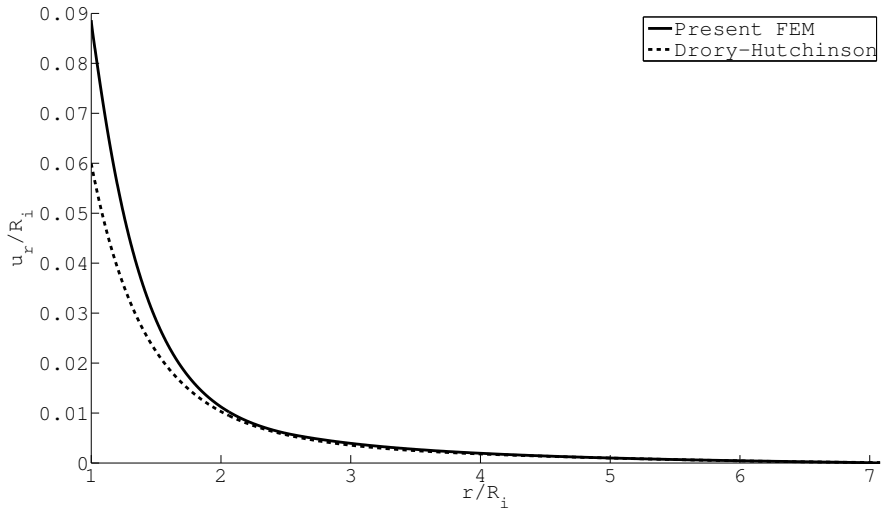

Figure 3.3: Radial displacement from (Drory and Hutchinson, 1996) and current FEM model

$r/R_i \lessapprox 2$ where the difference between the two results increases. This is expected since the expression in equation 3.4 which is only intended to be precise in the area $2 \leq r/R_i \leq 5$. The results from the new FEM analysis are precise in the entire range $1 \leq r/R_i \leq \infty$.

Indentation without film

Figure 3.4 shows the results for an elastic-perfectly plastic indentation without film. Figure 3.4 shows the radial surface displacements u_r. As it can

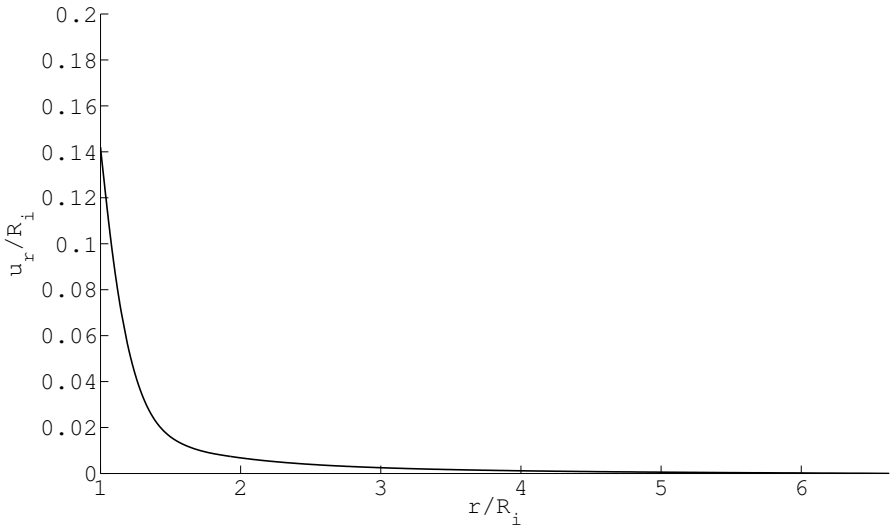

Figure 3.4: Radial surface displacement from Rockwell indentation of elastic-perfectly plastic solid with no film

be seen, they are qualitatively similar to the results shown in figure 3.3.

Figure 3.5 shows the circumferential stresses from the FEM analysis. The solid line is the hoop stress from the FEM analysis. The stress have a large negative value very close to the indenter. The plastic zone has an extent to $r/R_i \approx 1.8$. Near the indenter and the elastic-plastic transition edge, the stress is tensile while it is compressive in the middle of the plastic zone.

The circumferential stress outside the plastic zone is calculated by equation 2.21 and is plotted in the figure. Very good agreement with this expression is seen.

In the plastic zone, the obtained FEM values for $\sigma_{\theta\theta}$ are not identical to the film stress. The film is assumed linear elastic and thus the film stress must be calculated by equation 3.3. The dashed line in figure 3.5 shows the

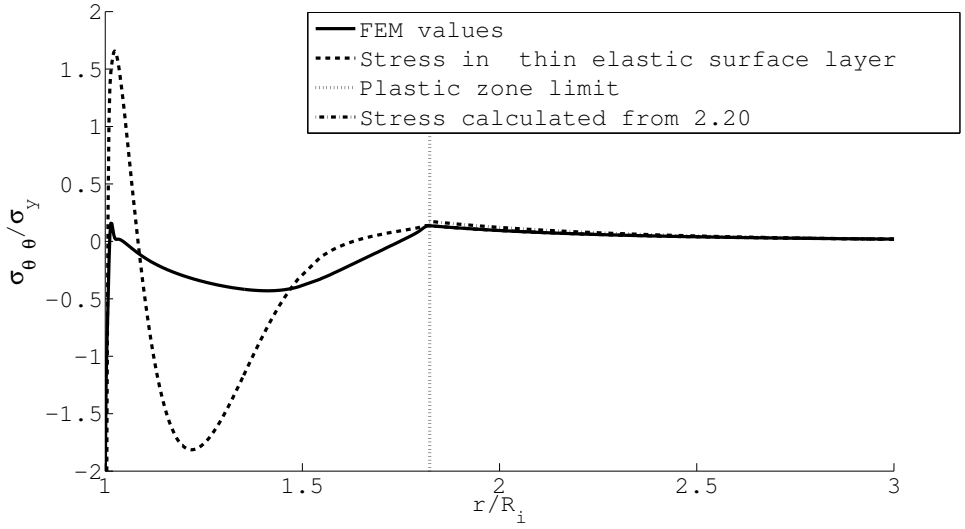

Figure 3.5: $\sigma_{\theta\theta}$ for conical indentation of elastic-perfectly plastic solid with no film

film hoop stress calculated from equation 3.3. The strains are also calculated in the FEM analysis. Since $u_r/r = \epsilon_{\theta\theta}$ and $du_r/dr = \epsilon_{rr}$ the strains from the FEM analysis are used instead of calculating the strains from the surface displacements. This calculated "elastic" stress differs significantly from the plastic stresses also shown. As expected, the two curves are identical in the elastic area.

As described, the "film" stresses approach a large negative value when approaching the indentation edge. This means that compressive hoop stresses should be present in the indented film very close to the indentation edge. This is not in correlation with experiments. Compressive stresses would contradict the fracture pattern seen since cracking would not occur with compressive stresses.

Indentation with film

Figure 3.6 shows $\sigma_{\theta\theta}$ in the film for a Rockwell indentation of a film/substrate system. The stresses have a large value at the indentation edge and then declines quickly away from the indenter. This picture is very different from the picture seen on figures 2.3 and 3.5 which shows negative circumferential stresses near the indenter. This behaviour of the stress-strain curve is more in correlation with what would be expected from the crack pattern seen in figure 3.2 where large circumferential stresses would cause cracking

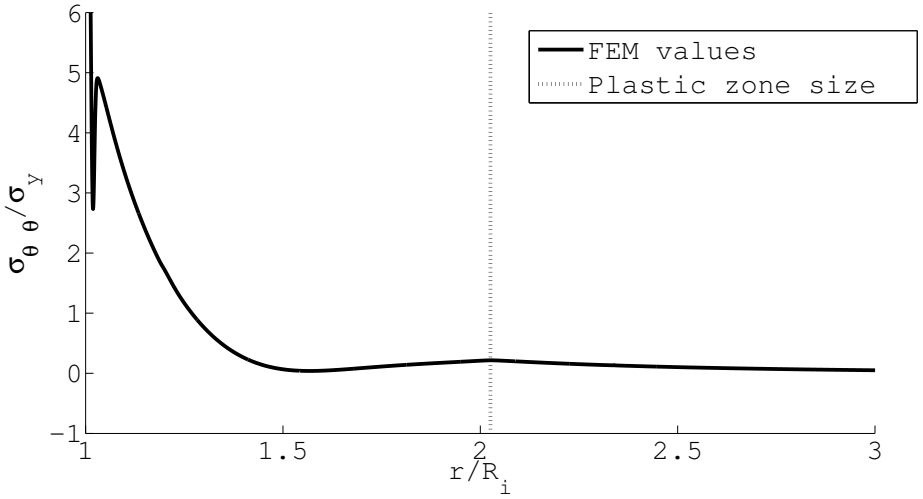

Figure 3.6: Hoop stress from indentation with film, $\delta/h = 100$

and the cracks arrest when moving away from the indenter. As for the case without film, a local maximum is seen at the elastic-plastic border.

Influence of indentation depth

In order to investigate the difference between the film hoop stress given as an output from the FEM analysis and the film hoop stress calculated from the substrate surface strains, the results are plotted for varying indentation depths. Figures 3.7 and 3.8 show the hoop stress, both the FEM output and the calculated, for different indentation depths. The results for the FEM output and the calculated stresses lie very close to each other. The graphs for different indentation depths show the same trend as explained above. The error is larger for the larger indentation depths but the stresses are also of larger magnitude so the relative error is still small.

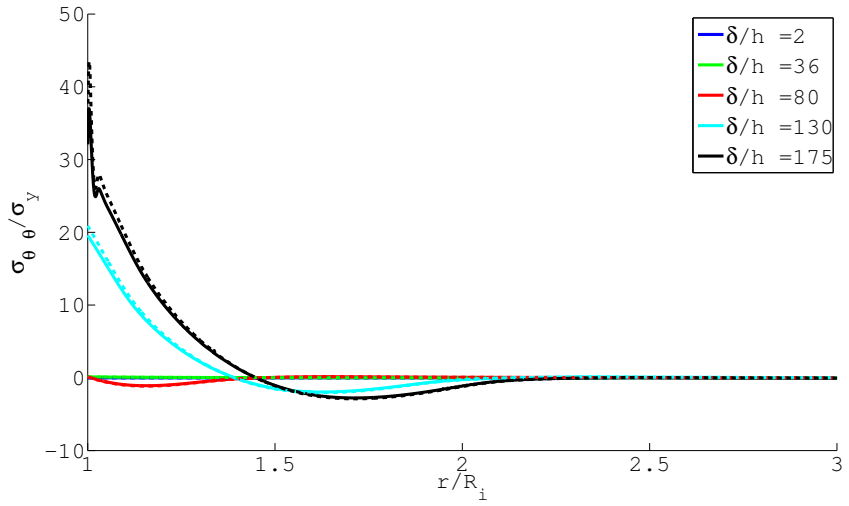

Figure 3.7: Circumferential stresses for varying δ/h. Solid line is the FEM output and dashed line is calculated from surface strains

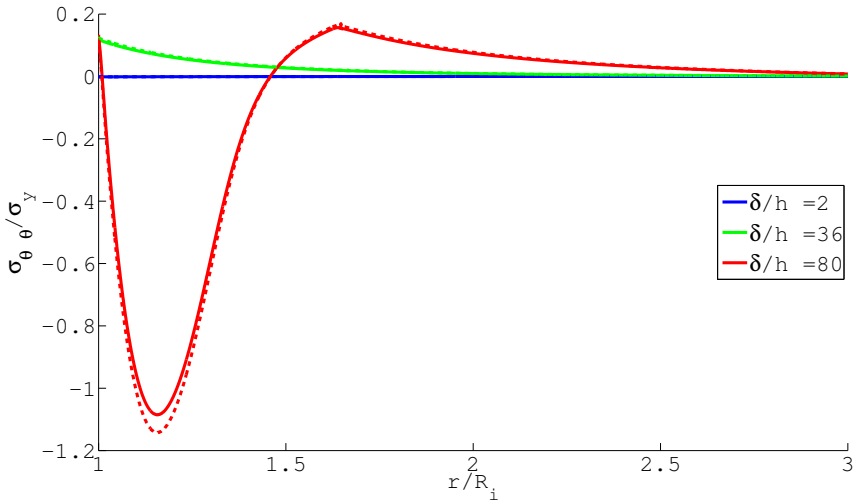

Figure 3.8: Circumferential stresses for varying δ/h, closeup. Solid line is the FEM output and dashed line is calculated from surface strains

Film bending influence

It is also investigated if film bending has an influence on the result. The through-thickness radial stress σ_{rr} is plotted at the location where σ_{rr} on the surface has maximum. The result is seen on figure 3.9. The circumferential

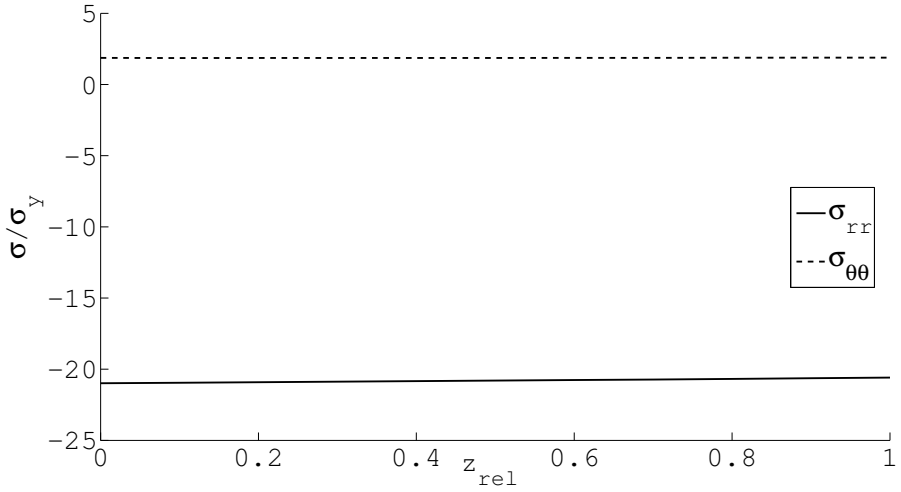

Figure 3.9: Through-thickness stress variations for radial and circumferential stress. $z_{rel} = 0$ is the film/substrate interface and $z_{rel} = 0$ is the film surface

stress, $\sigma_{\theta\theta}$, and the radial stress, σ_{rr}, are plotted as a function of the relative through-thickness z_{rel} position in the film. At the film/substrate interface, the $z_{rel} = 0$ and at the film surface, $z_{rel} = 1$. The radial stress, which should be varying linearly throughout the film thickness if the film was influenced by bending, is nearly constant throughout the film thickness. This implies that film bending has no significant influence on the film stress state. Also the circumferential stresses are constant throughout the film. This means that through-thickness cracks is a valid assumption. Also it can be seen that the radial stresses are much smaller than the circumferential stresses. This implies that the cracking pattern for the indentation will be radial cracks and not circumferential cracks as seen for smaller indentation depths. The results are similar to results from (Drory and Hutchinson, 1996) who came to the same conclusion from a analytical dimensional analysis of the elastic bending energy in the film.

Influence of substrate yield strength

Figures 3.10 and 3.11 shows the hoop stresses as a function of the substrate yield strength. The results shows that the hoops stress curves look very sim-

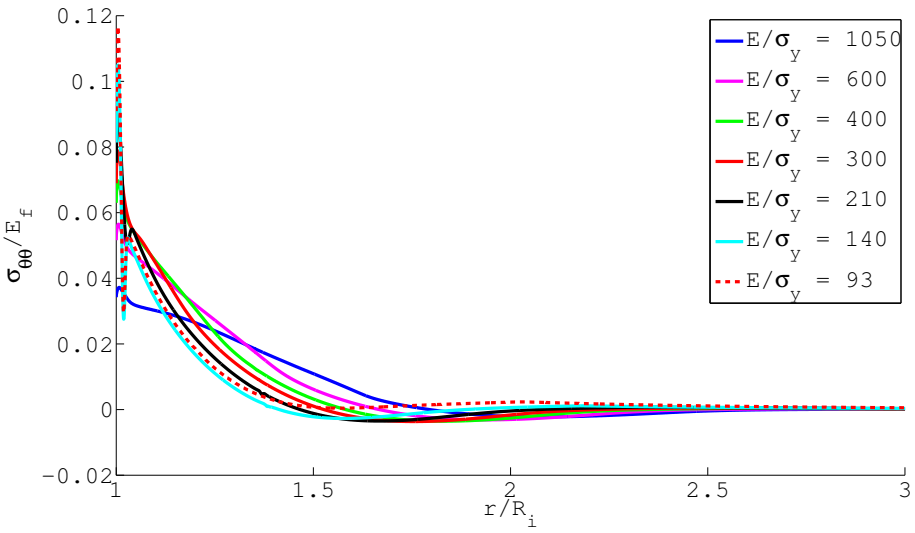

Figure 3.10: $\sigma_{\theta\theta}$ for varying yield strength. $\delta = 100h$

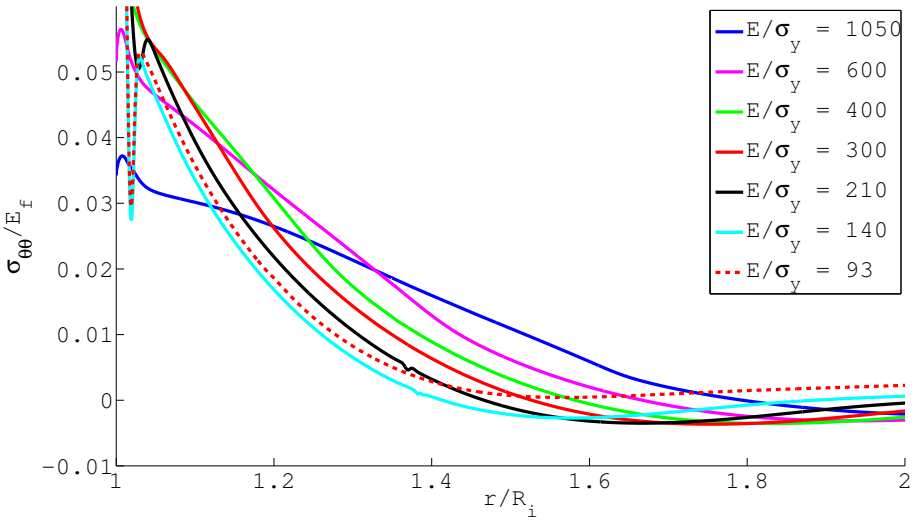

Figure 3.11: $\sigma_{\theta\theta}$ for varying yield strength, closeup $\delta = 100h$

ilar for all plotted values of E/σ_y. Only the low value of $E/\sigma_y = 1050$ has a

different course. This is in good agreement with intuition. The film stresses are determined by the displacements in the substrate. The substrate deformations are transferred to the film which is strained according to these displacements. When the indentation depth is held constant, the displacements are similar for all substrate material properties. For all other curves, the stress values are very close to each other. The current FEM analysis is displacement controlled and for all simulations the indentation depth is $\delta/h = 100$.

The results shown in figure 3.10 could imply that substrate yield strength has little influence on the stress state in the film. However, the indenter force necessary to reach this depth varies significantly with the substrate yield strength. Figure 3.12 shows the mean contact pressure p_m as a function of the varying yield strength for $\delta = 200h$. The mean pressure is calculated as

$$p_m = \frac{P}{\pi R_i^2} \tag{3.6}$$

Where P is the indentation force and R_i is the indentation radius. The

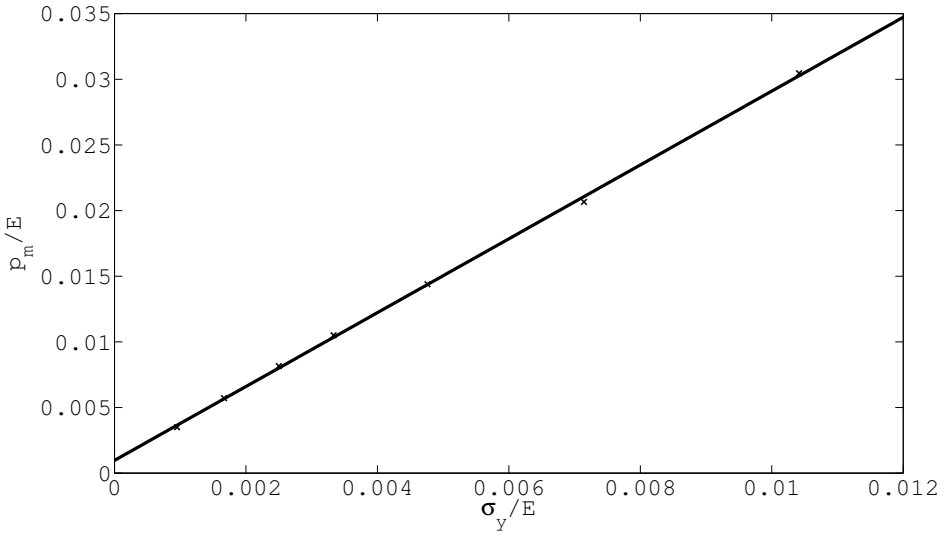

Figure 3.12: Mean indentation pressure as function of yield strength for $\delta = 100h$

indentation pressure increases linearly with increasing yield strength. A normal Rockwell indentation is force controlled and performed by applying a fixed force. This means that increasing yield strength will result in decreasing indentation depths.

Figure 3.13 shows the indentation radius R_i as a function of the substrate yield strength, again with a fixed indentation depth $\delta/h = 100$. The indetation radius R_i is normalised with the indentation depth δ. As it can

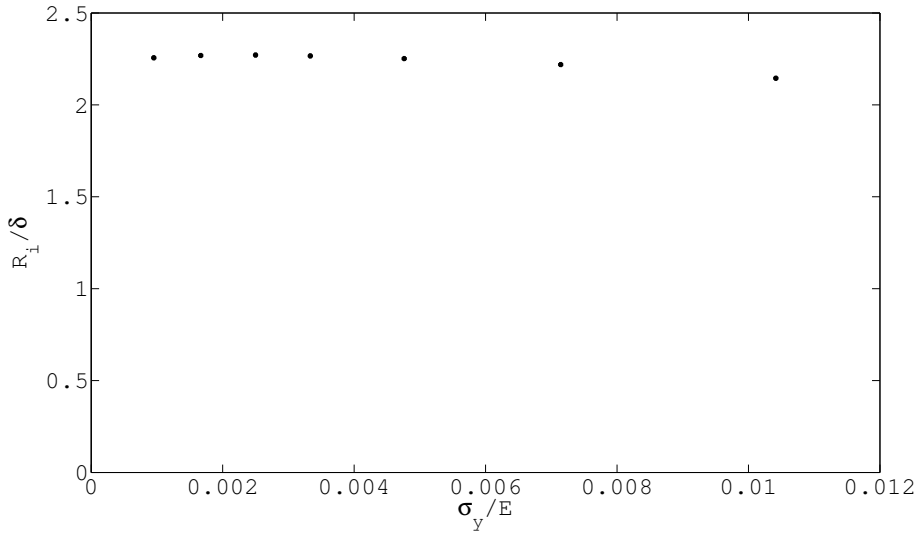

Figure 3.13: R_i as a function of substrate yield strength

be seen R_i varies very little for varying substrate yield strength. This implies that the indentation radius is a good measure for determining the film stress state.

Part II

Analysis of parallel crack arrays

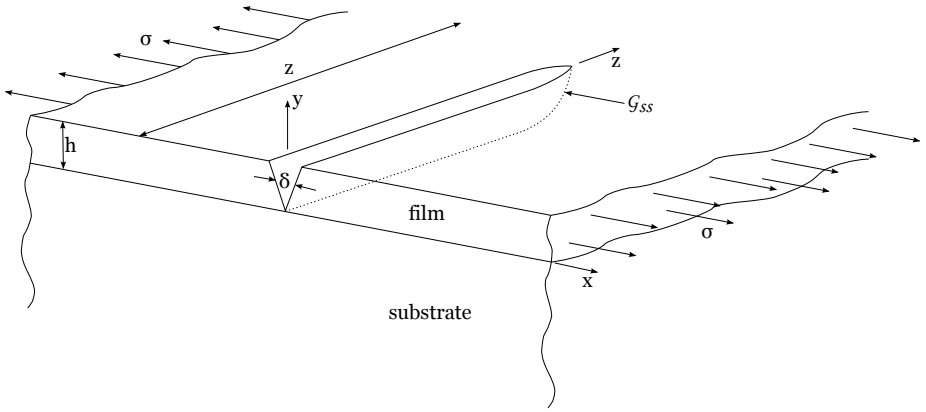

Figure 4.1: A 3D through-crack channelling across a film

Chapter 4

Crack mechanisms

A detailed description of the driving mechanisms for the cracking pattern seen at the indentation is of crucial importance in order to be able to determine fracture toughness. Relevant fundamental mechanisms and expressions for film cracking and crack patterns are outlined and explained.

4.1 Channelling cracks

A brittle coating under homogeneous tensile stress may fail by the extension of channelling cracks. Consider the 3D crack in figure 4.1. The crack is a through-thickness crack in a film reaching all the way through the film to the substrate. The film is loaded by a homogeneous tensile stress σ. The film thickness is denoted h. When the crack reaches a certain length, the energy release rate for the crack growth becomes independent of the crack length and conditions at the crack tip. The crack growth has then reached

steady state growth. (Xia and Hutchinson, 2000), amongst others cites the results from (Nakamura and Kamath, 1992) who investigated the three-dimensional crack growth. The results from this paper state that the crack reaches steady-state when the crack length is only a few times larger than the film thickness, see figure 4.2. This result is also confirmed by (Xia and Hutchinson, 2000) who has made a two-dimensional analysis of through-thickness cracks in thin films. For elastic identical film and substrate, (Xia and Hutchinson, 2000) concludes that steady-state is reached for $c/h \approx 4$ (c is the crack length) for a central crack. The investigation performed by (Nakamura and Kamath, 1992) studies only the case with an infinitely stiff substrate. Newer results performed by (Ambrico and Begley, 2002) investigates the propagation of a crack from an initial flaw towards steady-state crack growth for a through-thickness crack. The analysis is a three-dimensional finite-element analysis. Furthermore, Ambrico and Begley also investigates the effects of the elastic properties for the substrate. The results can be seen in figure 4.3. The elastic mismatch between the film and the substrate is described with the parameter α which is explained in detail in section 4.1. Shortly, $\alpha = -1$ corresponds to an infinitely stiff substrate and α increases with the relative film stiffness. For an infinitely stiff film, $\alpha = 1$. The original result from Nakamura and Kamath can be seen in the top left corner of the two figures for $\alpha = -1$ where it can be seen that steady-state is obtained for a crack length only a few times the film thickness. When α increases the steady-state length increases too. For $\alpha = 0$ which is a system with identical elastic properties for the film and substrate, the steady-state length is much longer. For an edge crack, an energy release rate of 90% is first obtained when the crack length is 15 times the film thickness.

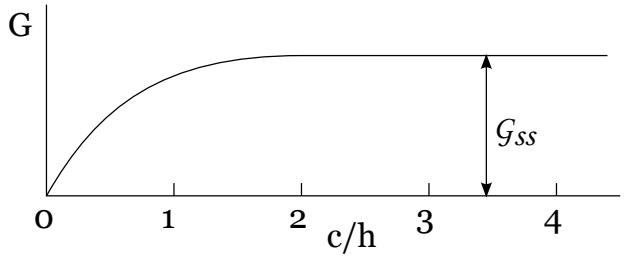

Figure 4.2: Qualitative approach to steady-state channelling, (Nakamura and Kamath, 1992)

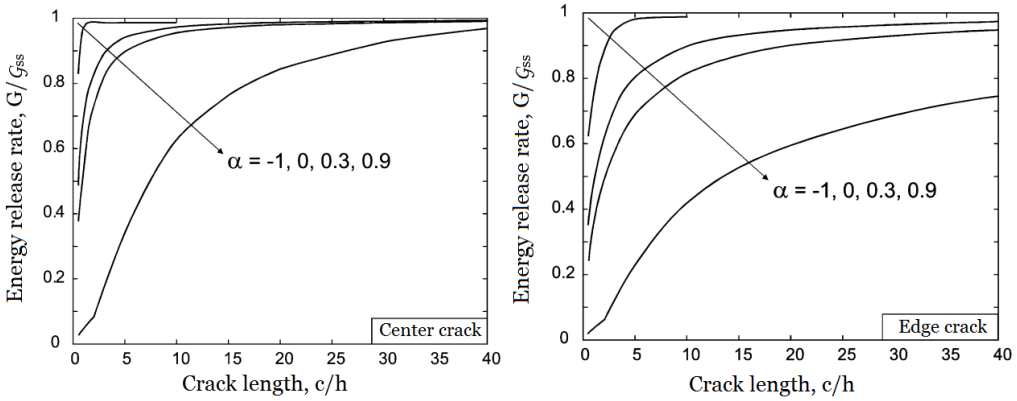

(a) Center cracks (b) Edge cracks

Figure 4.3: Energy release rate for elastic cracks in a single layer vs channelling crack length for different material mismatch, (Ambrico and Begley, 2002)

Basic expressions for channelling cracks

Under conditions of steady state cracking, the energy release rate can be evaluated without knowledge of the conditions at the crack front and the shape of the crack front. To obtain the energy release rate, two plane problems are examined. The strain energy in a slice of film with unit thickness far behind the crack front is subtracted from the strain energy in a unit slice far ahead the crack tip. One solution to this problem is

$$\mathcal{G}_{ss} = \frac{\sigma}{2h} \int_0^h \delta_c(y) dy \tag{4.1}$$

Where $\delta_c(y)$ is the displacement profile for a plane strain crack and σ is the film stress. An alternative formula is

$$\mathcal{G}_{ss} = \frac{1}{h} \int_0^h G_{ps}(a) da \tag{4.2}$$

Where $G_{ps}(a)$ is the energy release rate of a plane strain crack of depth a, see figure 4.4 (Beuth, 1992; Hutchinson and Suo, 1992). If the system is elastic homogeneous the corresponding plane strain problem is an edge crack in a half plane. This is a standard fracture mechanics problem and the solution is $G_{ps}(a) = 3.952\sigma^2 a/E$ (Tada et al., 2000). If this expression is inserted in equation 4.2 the result is

$$\mathcal{G}_{ss} = 1.976\sigma^2 \frac{h}{\bar{E}_f} \tag{4.3}$$

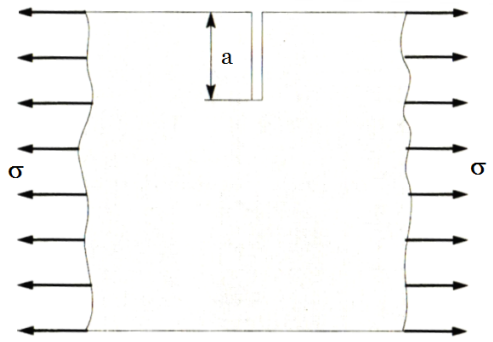

Figure 4.4: Edge crack in a half plane

Where $\bar{E}_f$ is the plane strain Young's modulus for the film, $\bar{E}_f = E_f/(1-\nu_f^2)$.

Elastic mismatch

The above expressions are only valid for an elastic homogeneous film/substrate system. For systems with different elastic properties for the film and substrate the situation is more complicated.

Dundurs' parameters

Dundurs (Dundurs, 1967, 1969) has showed that a wide class of plane problems of elasticity for bimaterials depends only on two (rather than three) parameters.

Using Airy's stress function to describe the stresses in an elastic, plane body loaded by surface tractions, the stresses and displacements depend on two elastic constant, namely the shear modulus μ and Poisson's ratio ν. In a composite body consisting of two isotropic and elastic materials, the stress field depends on three elastic parameters. The parameters can be chosen as the Poisson's ratio for each material, ν_1 and ν_2, and the ratio of the shear modulus for each material, $\Lambda = \mu_2/\mu_1$. If a number of assumptions are met, the stress field can be shown to depend only on two parameters which are combinations of the elastic constants for the two materials.

Plane deformation is assumed, either plane stress or plane strain. Linear theory must apply so that the stresses are proportional to the applied surface tractions. The composite body is loaded by prescribed surface tractions. For the bonded interface of interest in a film/substrate system, displacements and tractions must be continuous at the interface. With the latter two assumptions, boundary conditions for the free surfaces and the

interface of the composite body is given. By linear combinations of the equations giving the boundary conditions, it can be shown that only two (of four) combinations of the elastic constants can be varied independently. This postulation also holds for an ideally smooth interface and an interface with friction, (Dundurs, 1967).

Dundurs originally proposed, (Dundurs, 1967) the two parameters to be

$$D_\delta = \frac{\Lambda\xi_1 + 1}{\xi_2 + 1}, \qquad D_\eta = \frac{\Lambda + \xi_2}{\xi_2 + 1} \tag{4.4}$$

Where $\xi_i = 3-4\nu_i$ for plane strain and $\xi_i = (3-\nu_i)/(1+\nu_i)$ for plane stress. The indices $i = 1, 2$ corresponds two the two bodies of the composite body. Fo a film/substrate system 1 and 2 refers to respectively the film and the substrate.

The choice of the two parameters is not unique, and Dundurs later proposed two other parameters, (Dundurs, 1969) that now are known as the two Dundurs' parameters:

$$\alpha = \frac{\mu_1(\xi_1 + 1) - \mu_2(\xi_2 + 1)}{\mu_1(\xi_1 + 1) + \mu_2(\xi_2 + 1)}, \quad \beta = \frac{\mu_1(\xi_1 - 1) - \mu_2(\xi_2 - 1)}{\mu_1(\xi_1 + 1) + \mu_2(\xi_2 + 1)} \tag{4.5}$$

The α parameter can also be written as

$$\alpha = \frac{\bar{E}_1 - \bar{E}_2}{\bar{E}_1 + \bar{E}_2} \tag{4.6}$$

Where $\bar{E}_i = E_i$ in plane stress and $\bar{E}_i = E_i/(1-\nu_i^2)$ for plane strain. It can be seen from the above equation that α is a measure of the plane tensile modulus mismatch across the interface. For a very stiff film compared to the interface, α approaches 1 and for a very compliant substrate α approaches -1. Thus $-1 < \alpha < 1$.

In plane strain β can be written as

$$\beta = \frac{1}{2}\frac{\mu_1(1 - 2\nu_2) - \mu_2(1 - 2\nu_1)}{\mu_1(1 - 2\nu_2) + \mu_2(1 - 2\nu_1)} \tag{4.7}$$

If Poisson's ratio is assumed nonnegative, the physically admissible range for β with respect to α is then restricted to $|\alpha - 4\beta| \leq 1$. For most practical material combinations, the value of β typically lies between $\beta = 0$ and $\beta = \alpha/4$. Furthermore, β typically has only little influence on the results compared to the influence from α. For that reason, results are typically only presented for the two limiting values of β, $\beta = 0$ and $\beta = \alpha/4$ (Beuth, 1992). Values for α and β for a range of material combinations can be seen in figure 4.5. Note that the indices for the materials have been selected so material 1 is the stiffer of the two materials and thus $\alpha \geq 0$.

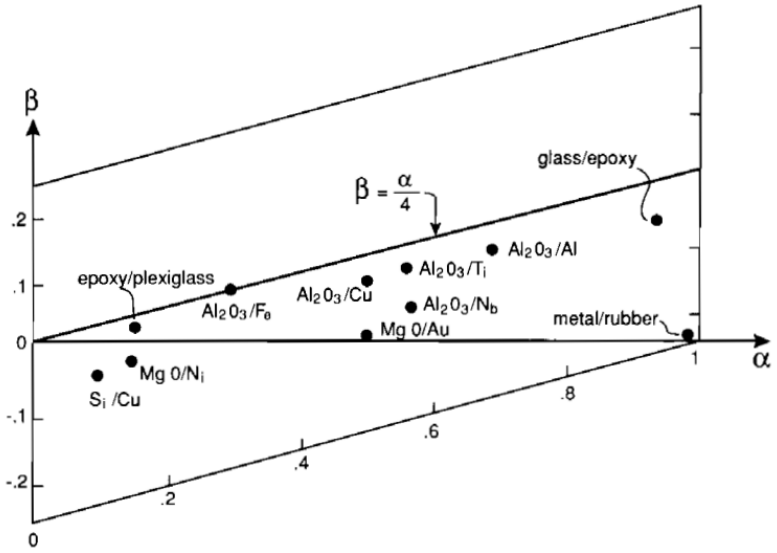

Figure 4.5: Values of Dundurs' parameters in plane strain for selected combination of materials (Hutchinson and Suo, 1992)

Channelling crack driving force for elastic mismatch

In (Beuth, 1992), the approach described in equation 4.3 is expanded to account for elastic mismatch. Beuth presents solutions to two problems. One is the fully cracked problem and the second is a partially cracked film. Only the fully cracked case is described.

Beuth determines the mode I stress intensity factor K_I for the fully cracked problem with the crack tip at the interface. A sketch of the problem can be seen in figure 4.6. For the fully cracked problem Beuth defines K_I

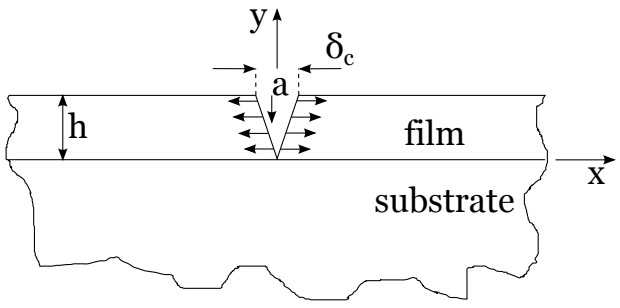

Figure 4.6: Crack problem investigated by Beuth (Beuth, 1992)

as

$$K_I \equiv \lim_{y \to 0^-} \left[(-2\pi y)^q \sigma_{xx}(0, y) \right] \tag{4.8}$$

The stress singularity exponent q is a function of the Dundurs parameters α and β and q satisfies the following equation derived by (Zak and Williams, 1963):

$$\cos(q\pi) - 2\frac{\alpha-\beta}{1-\beta}(1-q)^2 + \frac{\alpha-\beta^2}{1-\beta^2} = 0 \tag{4.9}$$

No elastic mismatch between film and substrate giving $\alpha = 0$ and $\beta = 0$ gives $q = 1/2$ and equation 4.9 corresponds to the classic definition of the mode I stress intensity factor for a crack in a homogeneous solid. The stresses just ahead of the crack tip in the y direction is given by

$$\sigma_{xx}(0, y) = C_1 \frac{\sigma h^q}{(-y)^q} \tag{4.10}$$

Where C_1 is a nondimensional function of α and β only. The detailed derivation of K_I and σ_{xx} is not given here.

To describe the steady state energy release rate, non-dimensional quantity $g(\alpha, \beta)$ is introduced

$$g(\alpha, \beta) = \frac{\int_0^h \delta_c(y)dy}{\pi \frac{\sigma}{\bar{E}_f} h^2} \tag{4.11}$$

The quantity g is a normalised integral of the crack opening displacement and is a function of the two Dundur's parameters. A plot of $g(\alpha, \beta)$ as a function of α can be seen in figure 4.7. The steady state energy release rate for a through-thickness channelling crack can then be expanded with $g(\alpha, \beta)$ to account for elastic mismatch. The argument from equation 4.1 can then be used to give the expression for the steady-state energy release rate for a through-thickness channelling crack for elastic mismatch.

$$\begin{aligned} \mathcal{G}_{ss} &= \frac{\sigma}{2h} \int_0^h \delta_c(y)dy \\ &= \frac{\sigma}{2h} g(\alpha, \beta) \frac{\pi h^2 \sigma}{\bar{E}_f} \\ &= \frac{1}{2} \frac{\sigma^2 h}{\bar{E}_f} \pi g(\alpha, \beta) \end{aligned} \tag{4.12}$$

Looking at elastically identical materials, it is recalled from equations 4.1 and 4.2 that the steady state energy release rate can be expressed in two ways:

$$\mathcal{G}_{ss} = \frac{\sigma}{2h} \int_0^h \delta_c(y)dy, \quad \mathcal{G}_{ss} = \frac{1}{h} \int_0^h G_{ps}(a)da \tag{4.13}$$

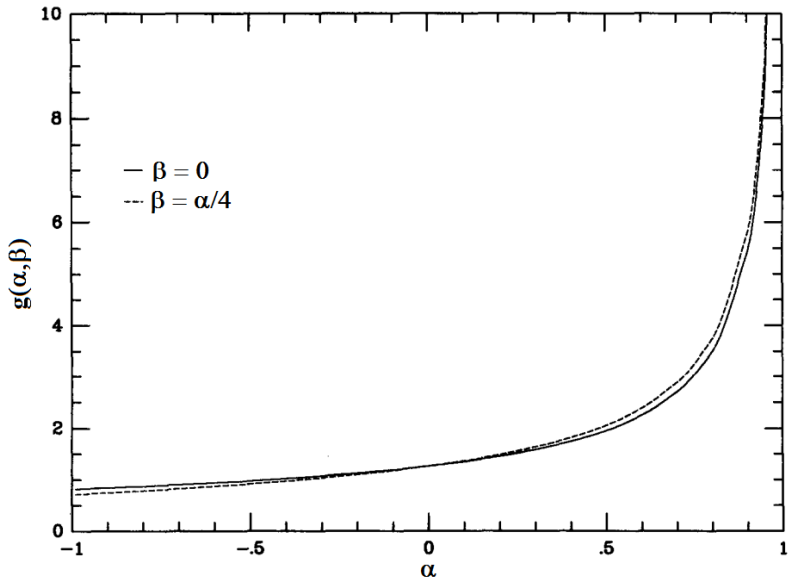

Figure 4.7: Plot of $g(\alpha, \beta)$ as a function of α for $\beta = 0$ and $\beta = \alpha/4$

Equating these two expressions and inserting $\int_0^h \delta_c(y)dy = g(\alpha, \beta)\pi\sigma h^2/\bar{E}_f$ from equation 4.11 and remembering that for linear elastic fracture mechanics $G = K_I^2/\bar{E}_f$ the following expression is derived

$$g(0, 0) = 1.1215^2 \tag{4.14}$$

For an edge crack in an homogenous half-plane $K_I = 1.1215\sigma\sqrt{\pi a}$ (Tada et al., 2000) . Inserting this value for $g(0, 0)$ in equation 4.13 gives $\mathcal{G}_{ss} = 1.976(\sigma^2 h)/\bar{E}_f$, which is the same as equation 4.2.

Plasticity in the substrate

Plasticity in the substrate has been addressed by (Beuth and Klingbeil, 1996). Here, Beuth and Klingbeil expands the work from (Beuth, 1992) to include effects of substrate yielding and strain hardening. The problem investigated is identical, but here the solution method is FEM-based. The key results of the work can be seen on figure 4.8 The analysis setup is identical to figure 4.6. Here the substrate constitutive relation is described by a Ramberg-Osgood relation. The results in figure 4.8 is on basis of a perfectly plastic material.

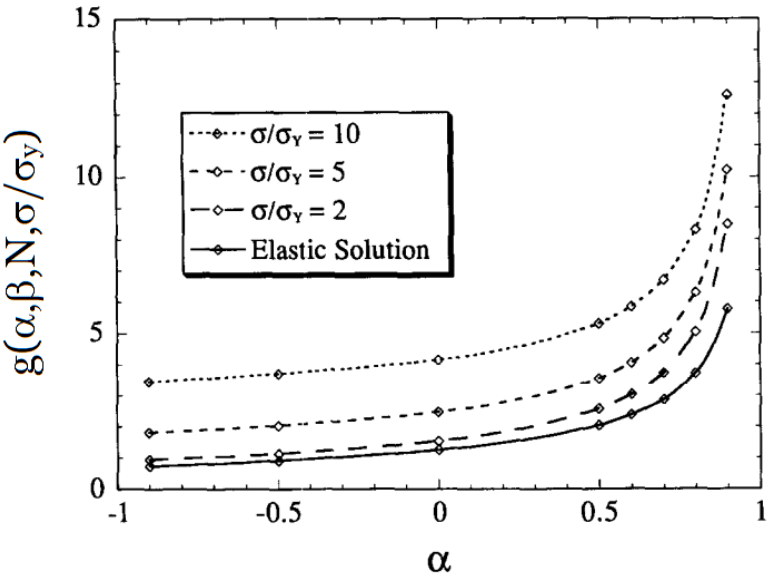

Figure 4.8: $g(\alpha, \beta, N, \sigma/\sigma_y)$ versus α for various values of σ/σ_y, $\beta = \alpha/4$ and $N = 100$, (Beuth and Klingbeil, 1996)

4.2 Crack interaction and spacing

When gradually increasing the stress in a film attached to a substrate and given that the interface fracture toughness is high enough to prevent delamination, the film will fail by the formation of a number of cracks propagating from the surface to the interface and subsequent channelling across the film.

A number of different models for the interaction and saturation of parallel channelling cracks exist.

An analysis for parallel cracking of a system with identical elastic properties of film and substrate is carried out by (Thouless, 1990). The cracks are assumed to be propagating simultaneously and have obtained steady-state.

The procedure to determine the energy release rate is the same as presented by (Hutchinson and Suo, 1992). The energy release rate is obtained by comparing the strain energy stored in a unit slice far ahead and far behind the front of parallel propagating cracks. As for the single crack this can be found by integrating a text book solution for an array of edge cracks, see figure 4.9.

$$\mathcal{G}_{ss} = \frac{1}{h} \int_0^h G_{ps}(y) dy \tag{4.15}$$

Where $G_{ps}(y)$ is the energy release rate for one crack for the problem in

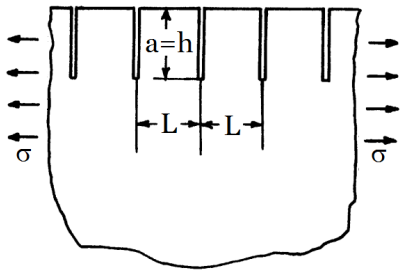

Figure 4.9: Fracture-mechanical problem used to compute the energy release rate (Tada et al., 2000)

figure 4.9. The solution to the integral is.

$$\mathcal{G}_{ss} \approx 1.98\frac{\sigma^2 h}{\bar{E}_f} \quad L \gtrsim 8h$$
$$\mathcal{G}_{ss} \approx \left[0.5\frac{L}{h} - 0.0316\left(\frac{L}{h}\right)^2\right]\frac{\sigma^2 h}{E} \quad L \lesssim 8h \tag{4.16}$$

It can be seen in equation 4.16 that for a crack spacing larger than $8h$ the cracks do not interact.

If the stress in the film is gradually increased, then, according to Thouless, an array of cracks will form when a critical stress is reached. This critical stress can be found by isolating σ in the first line in equation 4.16. The spacing of these initial cracks will be determined by the position of any existing flaws in the film but it will be larger than $8h$. If the stress is larger than this critical stress, minimum crack spacing will be given from isolating L/h in the second line in equation 4.16.

$$\frac{\lambda_{min}}{h} \approx 8\left(1 - \sqrt{1 - 0.5\frac{\Gamma_f \bar{E}}{\sigma^2 h}}\right) \tag{4.17}$$

Where Γ_f is the fracture toughness, the critical energy release rate, for the film. Note that this is a minimum crack spacing, the actual crack spacing may differ from this. The λ notation is used to emphasise that this is a material value for the specific film.

Hutchinson and Suo (Hutchinson and Suo, 1992) uses the same argument as (Thouless, 1990) to investigate the energy release rate for an array of cracks. They develop this approach to consider not only the simultaneously propagation but also the sequential propagation of an array of cracks, see figure 4.10. Consider a situation where a film is already cracked due to a certain loading σ. If the loading is increased, a new set of cracks is

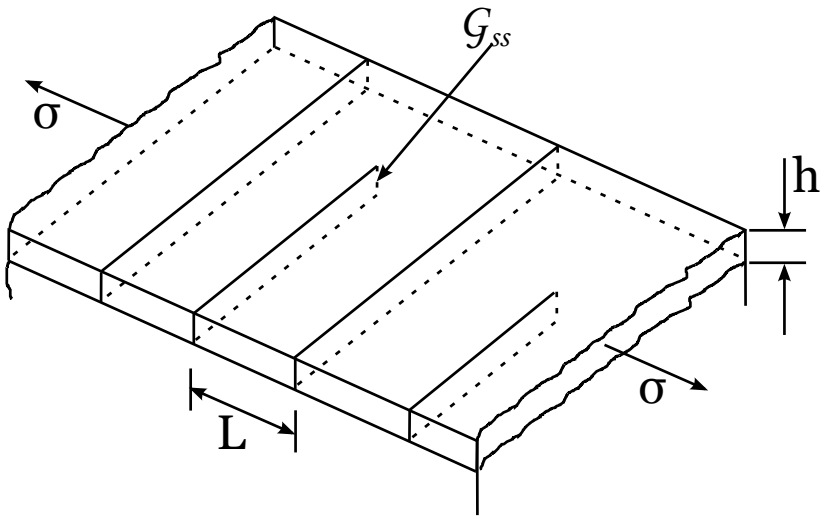

Figure 4.10: Sequential propagation of parallel cracks

nucleated and propagates halfway between the existing cracks. The energy release rate for this new set of cracks can be computed with the same argument as for a single crack. The strain energy far ahead and far behind the crack front for the new set of cracks is used to calculate the energy release rate for the new set of cracks. The strain energy in a unit slice containing one "old" and two "new" cracks is considered. Far behind the crack tip the crack spacing is L and there are two "new" cracks. Far ahead the crack tip there is one "old" crack with a spacing $2L$. Denoting the strain energy behind the crack tip U_L and the strain energy ahead of the crack tip U_{2L} the energy release rate can be calculated as

$$\mathcal{G}_{ss,seq} = (2U_L - U_{2L})\frac{1}{h} \tag{4.18}$$

Inserting the solution from equation 4.16 for $\mathcal{G}_{ss}$ for the simultaneously propagation the following expression for sequential propagation is derived.

$$\begin{aligned}
\mathcal{G}_{ss,seq} &= (2U_L - U_{2L})\frac{1}{h} \\
&= 2\left[0.5\frac{L}{h} - 0.0316\left(\frac{L}{h}\right)^2\right]\frac{\sigma^2 h}{\bar{E}_f} \\
&\quad - \left[0.5\frac{2L}{h} - 0.0316\left(\frac{2L}{h}\right)^2\right]\frac{\sigma^2 h}{\bar{E}_f} \\
&= 2 \cdot 0.0316\left(\frac{L}{h}\right)^2\frac{\sigma^2 h}{\bar{E}_f}
\end{aligned} \tag{4.19}$$

Delannay and Warren (Delannay and Warren, 1991) has carried out an analysis much similar to the above.

Thouless et. al. (Thouless et al., 1992) uses a different argument to look at the crack spacing than originally posted by (Thouless, 1990). Thouless et. al. uses an energy argument to derive an equilibrium crack spacing. The strain energy in the uncracked film is

$$U_0 = 0.5\frac{\sigma^2 h}{\bar{E}_f} \tag{4.20}$$

Using the result from equation 4.16 which gives the energy difference between the cracked and uncracked film, the strain energy in the cracked film can be found to be

$$U_L = 0.0316\frac{L}{h}\frac{\sigma^2 h}{\bar{E}_f} \tag{4.21}$$

The critical energy release rate Γ_f and the energy associated with the crack array can be related by

$$U_c = \Gamma_f \frac{h}{L} \tag{4.22}$$

The energy equilibrium crack spacing is found where the total energy of the film is minimised. The total energy can be expresses as

$$\begin{aligned} U_{total} &= U_L + U_c \\ &= 0.0316\frac{L}{h}\frac{\sigma^2 h}{\bar{E}_f} + \Gamma_f \frac{h}{L} \end{aligned} \tag{4.23}$$

The minimal total energy can then be found by finding the minimum for the expression in equation 4.23

$$\begin{aligned} \frac{\partial U_L}{\partial L} + \frac{\partial U_c}{\partial L} = 0 \Rightarrow \\ 0.0316\frac{\sigma^2 h}{\bar{E}_f}\frac{1}{h} - \frac{\Gamma_f h}{L^2} = 0 \Rightarrow \\ \frac{\lambda_{equi}}{h} = \sqrt{0,0316^{-1}} \cdot \sqrt{\frac{\bar{E}_f \Gamma_f}{\sigma^2 h}} \\ \approx 5.6\sqrt{\frac{\bar{E}_f \Gamma_f}{\sigma^2 h}} \end{aligned} \tag{4.24}$$

This expression gives a larger spacing for the same film properties than the expression stated in equation 4.17 which is the thermodynamically smallest possible spacing. The argument from equation 4.19 gives a spacing intermediate to these two. Another interesting difference is that equation 4.17

predicts that the absolute crack spacing L should decrease for increasing film thickness h. Equation 4.24 on the contrary states that L increases as $\sqrt{h}$. (Thouless et al., 1992) confirms the latter relation by experiments.

Elastic mismatch

A solution for the driving force for propagation of parallel cracks in an elastic inhomogenous system is presented by (Xia and Hutchinson, 2000). To implement the elastic mismatch, a characteristic length l is introduced

$$l \equiv \frac{\pi}{2} g(\alpha, \beta) h \tag{4.25}$$

Where $g(\alpha, \beta)$ is the nondimensional factor describing the elastic mismatch introduced by Beuth, (Beuth, 1992), see equation 4.11. For an elastic homogeneous system, $l = 1.976h$. By the use of the factor l, the energy release rate for the simultaneous propagation of a crack array can be expressed as

$$\mathcal{G}_{ss} = \frac{l\sigma^2}{\bar{E}_f} \tanh\left(\frac{L}{2l}\right) \tag{4.26}$$

It is seen, that the quantity $\tanh(L/(2l)$ describes the interaction distance, the distance at which cracks interact with each other. Like the expression developed by (Thouless, 1990), equation 4.16, equation 4.26 approaches the value for a single crack when the crack spacing is increased. By equating equation 4.12 and equation 4.26, it is seen that the only difference between the two expressions is the factor $\tanh(L/(2l))$. By solving the equation

$$\tanh\left(\frac{L}{h}\frac{1}{\pi g(\alpha, \beta)}\right) = 1 \tag{4.27}$$

the crack distance $(L/h)_\infty$ at which the cracks do not interact can be found. The solution is plotted in figure 4.11. Here, $(L/h)_\infty$ is taken as the value for 99% of the single crack value. The crack interaction distance depends on the elastic mismatch coefficient $g(\alpha, \beta)$. For stiff films, the elastic mismatch has a strong influence on the crack interaction distance and the cracks interact at much greater distances.

Using the argument from (Hutchinson and Suo, 1992), equation 4.18, the energy release rate for the sequential propagation of cracks cans be expressed as (Xia and Hutchinson, 2000)

$$\begin{aligned} \mathcal{G}_{ss} &= 2 \cdot G_{ss,L} - G_{ss,2L} \\ &= \frac{l\sigma^2}{\bar{E}_f}\left[2\tanh\left(\frac{L}{2l}\right) - \tanh\left(\frac{L}{l}\right)\right] \end{aligned} \tag{4.28}$$

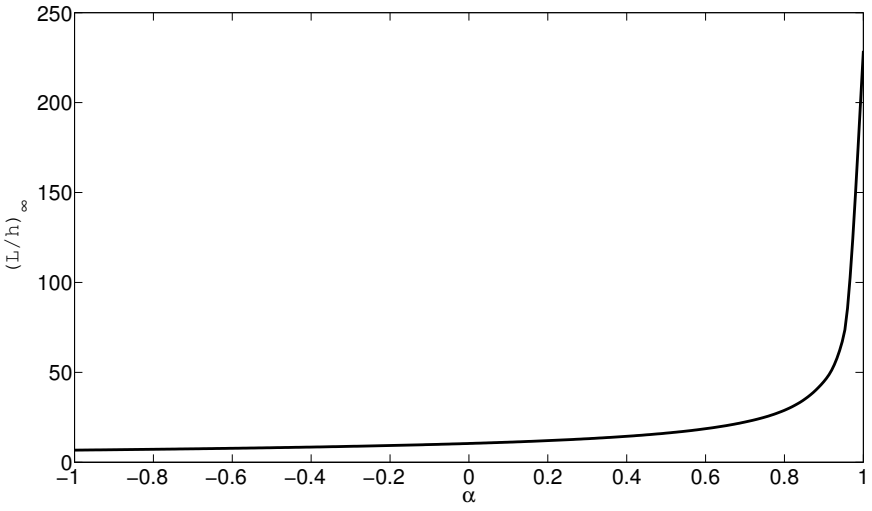

Figure 4.11: Crack spacing for no interaction for varying α

Crack spacing for yielding substrate

If the substrate is ductile, the crack spacing is dictated by the substrate yield stress. Crack spacing for a yielding substrate can be approximated by a simple shear lag analysis. The shear lag analysis for the film/substrate system is described by (Agrawal and Raj, 1989; Beuth and Klingbeil, 1996; Hu and Evans, 1989). The concept of the shear lag model is that the substrate yields at the surface. This results in a shear yield stress τ being transferred to the film from the substrate. (Hu and Evans, 1989) suggests a constant shear stress. It is assumed that a crack exists in the film. At the crack face the film is stress free. The stress in the cracked film can be found by considering a series of free body diagrams for different values of x. This gives:

$$\sigma_x^f = \frac{1}{h}\int_0^x \tau dx \Rightarrow \tag{4.29}$$

$$\sigma_x^f = \tau\frac{x}{h}, \quad (x < L_{slip})$$

$$\sigma_x^f = \sigma_f, \quad (x > L_{slip}) \tag{4.30}$$

Where x is the distance from the crack. L_{slip} is the slip length, the length necessary to "build up" the film stress σ^f, see figure 4.12. Enforcing equilibrium in the film gives a relation for the slip length

$$L_{slip} = \frac{\sigma h}{\tau} \tag{4.31}$$

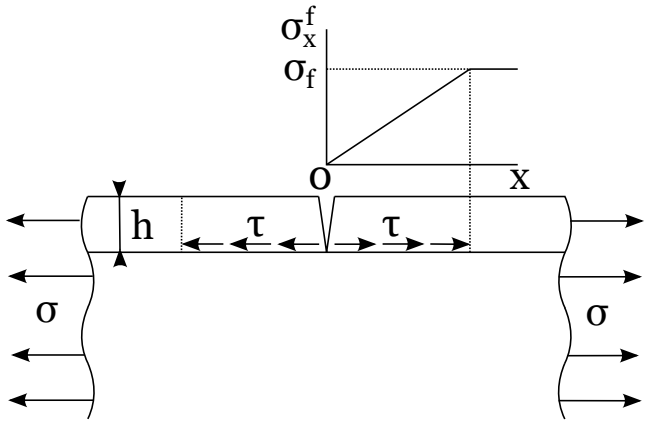

Figure 4.12: An illustration of the shear lag behaviour

For the shear lag case, minimum or saturation crack spacing $L_{min,yield}$ is typically determined to be of the order $L_{slip} < L_{min,yield} < 2L_{slip}$. This is because crack spacing larger than $2L_{min,yield}$ leaves segments of film which satisfies the cracking condition. On the other hand, for crack spacings smaller than $L_{min,yield}$ the critical crack condition is not satisfied in this range. Using that $\tau_y = \sigma_y/\sqrt{3}$ gives the following condition for the crack spacing for a yielding interface (Hu and Evans, 1989):

$$\sqrt{3}\frac{\sigma_f}{\sigma_y} < \frac{L_{min,yield}}{h} < 2\sqrt{3}\frac{\sigma_f}{\sigma_y} \tag{4.32}$$

Agrawal and Raj (Agrawal and Raj, 1989) assumes that the shear stress transferring the load to the substrate has a sinusoidal distribution instead.

$$\tau = \tau_y \sin\frac{2\pi x}{\hat{\chi}}, \quad 0 \le x \le \frac{\hat{\chi}}{2} \tag{4.33}$$

Where $\hat{\chi}$ is the wave length for the sine function in equation 4.33. The relation between $\hat{\chi}$ and the slip length L_{slip} is $\hat{\chi} = 2L_{slip}$. Using this expression in equation 4.29 gives the following expression for the shear lag crack spacing

$$\pi\sqrt{3}\frac{\sigma_f}{\sigma_y} < \frac{L_{min,yield}}{h} < 2\pi\sqrt{3}\frac{\sigma_f}{\sigma_y} \tag{4.34}$$

Comparison of crack spacing models

The plot in figure 4.13 shows a comparison of the crack spacing as a function of normalised film stress $(\sigma^2 h)/(\Gamma_f \bar{E}_f)$. For comparison, all the plots are for an elastic homogeneous system. For a fixed value of the film toughness, Γ_f,

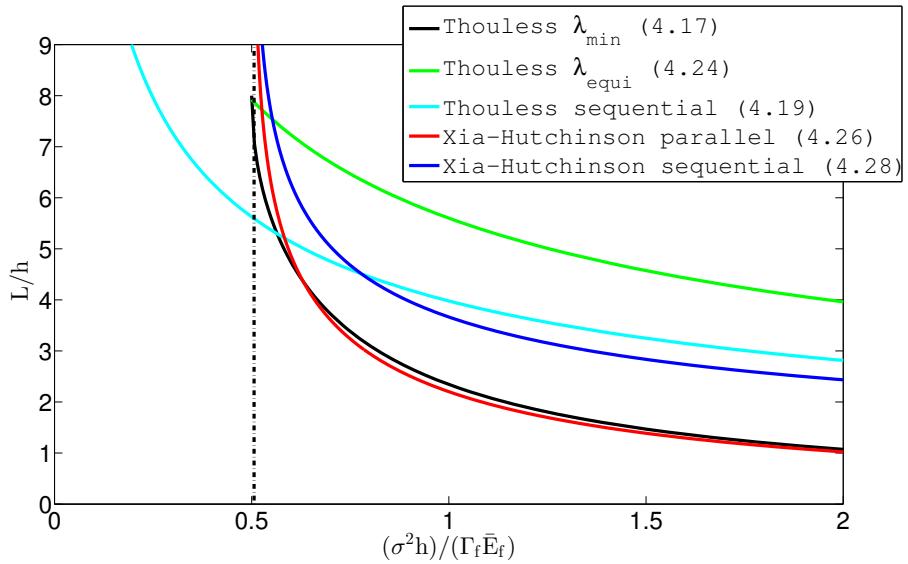

Figure 4.13: Comparison of expression for crack interaction

figure 4.13 shows the predicted crack spacing as a function of the normalised film stress. For a given film stress , the figure shows the crack spacing given by the various models. The model by (Thouless, 1990) dictates the lowest crack spacing. This spacing is given by the expression for the energy release rate for an array of cracks. The crack spacing given by (Thouless et al., 1992) is based on an energy argument and results in an equilibrium crack spacing. The argument accounts for the sequential propagation of cracks, that a new set of crack will form between existing cracks when the film stress is increased. This argument, equation 4.24, gives a higher spacing than the minimal possible spacing given by equation 4.17. Intermediate to these two crack spacings is the argument for the energy release rate for sequential crack propagation presented by (Hutchinson and Suo, 1992). This argument is presented by two curves. One for equation 4.19 which is the argument from equation 4.18 used on equation 4.16. And one calculated from equation 4.28. These two curves should be equal but this is not quite the case. The reason for this is not clear, but a reason might be that equation 4.19 is based on equation 4.16 which is not an exact solution. The two expressions giving the crack spacing for a parallel array, equation 4.17 and equation 4.26 are nearly coincident as expected. The vertical dash-dot line indicates the critical normalised stress for a single channelling crack. All the models except equation 4.28 either crosses the line or are very close to the line at $L/h = 8$ which is the spacing at which the cracks do not interact. For a given crack spacing and normalised film stress, being above

and left to the lines would indicate crack propagation.

4.3 Delamination

The adhesion of thin films on a substrate is an important parameter and delamination is a very common failure mode for thin films. Delamination is described in detail by for instance (Drory and Hutchinson, 1996; Freund and Suresh, 2004; Hutchinson and Suo, 1992; Suo and Hutchinson, 1990)

If linear elastic fracture mechanics is used, the problem of delamination can be solved by a superposition argument by considering the geometry given in figure 4.14. Here the substrate, material 2, is assumed very thick

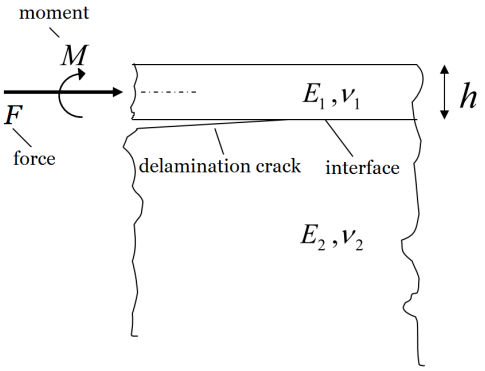

Figure 4.14: Cracking situation for delamination crack

compared to the film so that $h/T_{substrate} \to 0$, where $T_{substrate}$ is the substrate thickness. The steady-state energy release rate for delamination $\mathcal{G}_{del}$ can be evaluated by taking the difference between the strain energy in the system far ahead and far behind the crack front. Far ahead of the crack tip, the strain energy is zero. In this situation the steady-state energy release rate for delamination can be derived by the use of beam theory (Hutchinson and Suo, 1992)

$$\mathcal{G}_{del} = \frac{1-\nu_f^2}{2E_f}\left(\frac{F^2}{h} + 12\frac{M^2}{h^3}\right) \tag{4.35}$$

For a number of different film cracking scenarios including delamination, a unifying dimensionless cracking number Z can be introduced

$$Z = \frac{\mathcal{G}\bar{E}_f}{\sigma^2 h} \tag{4.36}$$

For steady-state film delamination of a film loaded with a through-thickness uniform stress, the applied moment is $M = 0$ and $F = \sigma h$. From equa-

tion 4.35 it follows that $Z = 0.5$. This means that a critical thickness h_c can be identified (Hutchinson and Suo, 1992):

$$h_c = \frac{1}{2}\frac{\Gamma_{del}\bar{E}_f}{\sigma^2} \tag{4.37}$$

For film thicknesses under this value, film delamination will not occur. When producing thin films, a large residual stress may rise from for instance mismatch in the thermal expansion of the film and substrate. Violating the critical values for either of the components in equation 4.37 means that spontaneous delamination of the film may occur.

The stress field at the interface crack tip depends on the elastic properties of the film and interface. The elastic mismatch between the film and substrate can be expressed by the two Dundurs' parameters, α and β. These are explained in section 4.1. The influence of β is negligible in virtually all realistic scenarios. Furthermore, setting $\beta \neq 0$ complicates the calculations significantly by introducing a so-called oscillatory singularity instead of the normal $r^{-1/2}$ singularity that applies in fracture mechanics for homogeneous materials. For those reasons $\beta = 0$ is normally used and in most cases error introduced by this is negligible (Hutchinson and Suo, 1992). For the rest of this section, the assumption $\beta = 0$ is used.

The relation between the energy release rate and the stress intensity factors for the problem showed in figure 4.14 is given by (Hutchinson and Suo, 1992)

$$\mathcal{G}_{del} = \frac{1-\beta^2}{2}\left(\frac{1}{\bar{E}_f} + \frac{1}{\bar{E}_s}\right)\left(K_I^2 + K_{II}^2\right) \tag{4.38}$$

Where K_I and K_{II} are given by

$$\begin{aligned} K_I &= \frac{1}{\sqrt{2}}\left(Fh^{-1/2}\cos\omega + 2\sqrt{3}Mh^{-3/2}\sin\omega\right) \\ K_{II} &= \frac{1}{\sqrt{2}}\left(Fh^{-1/2}\sin\omega + 2\sqrt{3}Mh^{-3/2}\cos\omega\right) \end{aligned} \tag{4.39}$$

Here ω is the phase angle describing the mode mixture, which is the relation between mode I and mode II cracking. This is generally defined by ψ. For $\beta = 0$, the mode mixture is a function of α and given by

$$\psi = \omega(\alpha) = \tan^{-1}\left(\frac{K_{II}}{K_I}\right) \tag{4.40}$$

The relation between α and ω can be seen in figure 4.15

The mode mixture also plays a significant role in the toughness of the interface. Figure 4.16 shows the influence of phase angle on interface toughness for an expoxy/glass interface (Liechti and Chai, 1992). It shows signif-

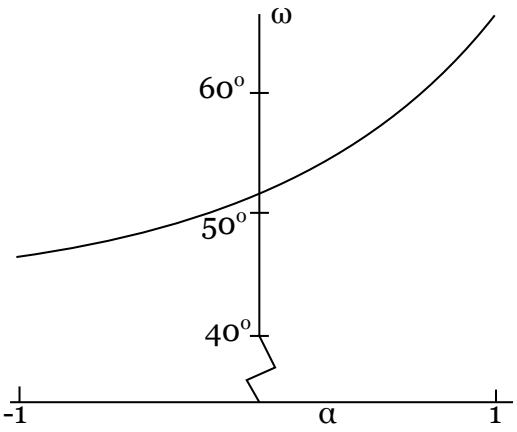

Figure 4.15: Relation between α and ω, (Hutchinson and Suo, 1992)

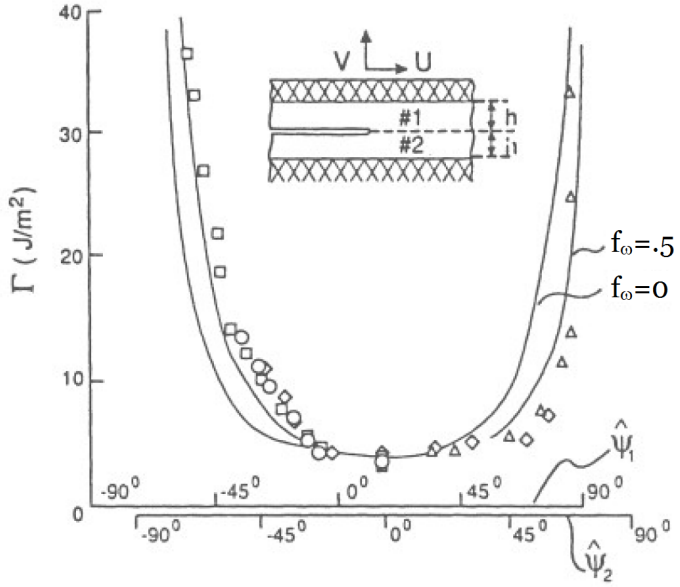

Figure 4.16: Mode mixity dependence on a glass/epoxy interface. Data from (Liechti and Chai, 1992)

icant mode dependence on the interface toughness. The mode dependence on toughness can be described in a simple way by a single parameter f_ω which enters the expression

$$\Gamma_{del}^{I} = \frac{1}{\bar{E}} \left(K_I^2 + f_\omega K_{II}^2 \right) \tag{4.41}$$

The limit $f_\omega = 1$ corresponds to the "ideally brittle" case as used in normal linear elastic fracture mechanics of homogeneous solids and the limit of

$f_\omega = 0$ corresponds to the case where crack advance only depends on mode I components. For all values of f_ω, Γ^1_{del} is the pure mode I delamination toughness. A phenomenological law of the mixed-mode interface toughness dependence of f_ω equivalent to equation 4.41 is given by (Jensen et al., 1990)

$$\Gamma_{del}(\psi) = \Gamma^I_{del}\left[1 + (f_\omega - 1)\sin^2\psi\right]^{-1} \tag{4.42}$$

Where Γ^I_{del} is the pure mode I toughness. A number of alternative toughness functions are suggested in (Hutchinson and Suo, 1992).

An advancing interface crack may also kink out into either the film or substrate. Consider figure 4.17, where a crack has kinked out of the interface. The kink angle Ω is angle between the advancing crack and the

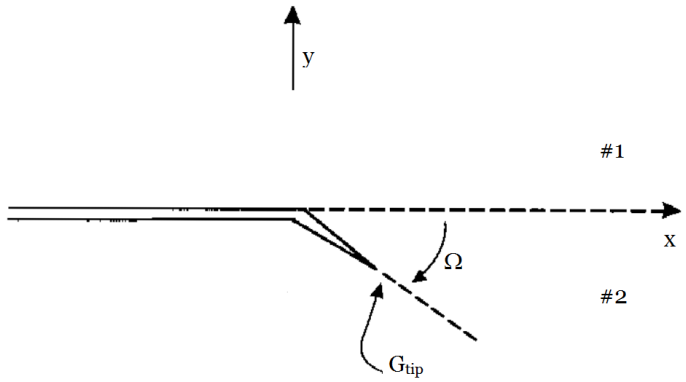

Figure 4.17: Sketch of a kinked crack

interface. Normally, material 1 refers to the film and material 2 to the substrate but in this case, the numbers designated for the material switches depending on the sign of the mixed mode phase angle ψ. The material numbers are chosen so that for $\psi > 0$, the crack kinks into material 2. If ψ is negative, the numbers are switched. A reasonable assumption is that the energy release rate at the tip of the kinked crack G_{tip} is maximised if Ω is oriented so the crack advances in pure mode I. The only exception from this is if the material that the crack kinks into is much stiffer that the other material ($\alpha < -0.67$). The relation for whether the crack kinks or not can be written as (He and Hutchinson, 1989)

$$\frac{\mathcal{G}_{del}}{G_{tip}} < \frac{\Gamma_{del}(\psi)}{\Gamma_2} \tag{4.43}$$

Where G_{del} is the energy release rate for the interface crack, G_{tip} is the energy release rate for the kinked crack and Γ_2 is the toughness of material

2 that the crack kinks into. The relation G_{del}/G_{tip} depends on the elastic mismatch parameter α and the mixed mode phase angle ψ. Depending on ψ and α, the kinked crack energy release rate can be twice as high as the interface energy release rate (He and Hutchinson, 1989). Whether the crack kinks out of the interface, and into which material it kinks, thus depends on the mixed mode phase angle, the material toughness and interface mixed mode toughness.

Buckling-driven delamination

When a film is loaded by compressive stresses, which often arise from thermal coefficient of expansion mismatch, the film may buckle when initially de-bonded.

The simplest solution is that for a straight-sided blister. The situation is sketched in figure 4.18 If the film buckles up, the compression is partially

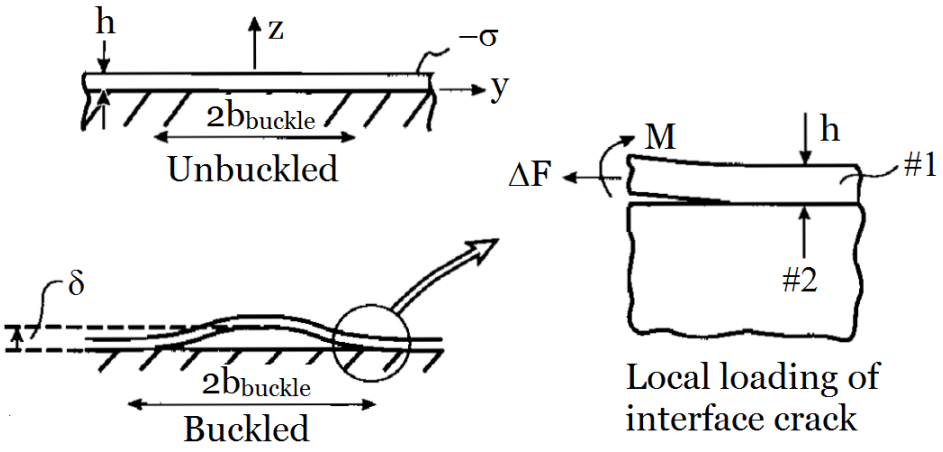

Figure 4.18: Geometry for the straight-sided blister, (Hutchinson and Suo, 1992)

relieved and a moment M develops. The stress release is denoted ΔF according to figure 4.18. To obtain the energy release rate for the interface crack $\mathcal{G}$, plate theory is used to derive M and ΔF, (Hutchinson and Suo, 1992).

$$G = \frac{(1-\nu_f^2)h}{2E_f}(\sigma - \sigma_c)(\sigma + 3\sigma_c) \tag{4.44}$$

Where

$$\sigma_c = \frac{\pi^2}{12}\frac{E_f}{1-\nu_f^2}\left(\frac{h}{b_{buckle}}\right)^2 \tag{4.45}$$

Where b_{buckle} is the width of the blister. If $\sigma < \sigma_c$ the film does not buckle. It can be seen from equation 4.44, if $\sigma \gg \sigma_c$ the energy release rate converges to the value given in equation 4.36 and the influence from buckling diminishes.

Buckling-driven delamination is very mode dependent. As previously mentioned the mode-dependence can be described by the value f_ω Without this mode dependence, f_ω, a blister would completely delaminate the film once propagation started. This very strong mode dependence, along with other properties, give cause to some very unusual blister morphologies, some of which can be seen in figure 4.19.

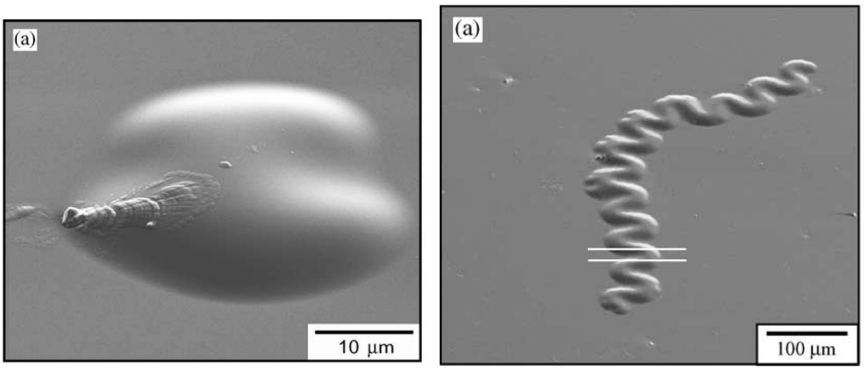

(a) (Moon et al., 2002a) (b) (Moon et al., 2002b)

Figure 4.19: Different delamination blister geometries

Indentation-induced delamination

An indentation test can be used to determine the interfacial toughness of a film/substrate system, (Drory and Hutchinson, 1996). In this work, the adhesion of a film on a substrate is determined by analysing the delamination that occurs from the stress field caused by a deep Rockwell indentation into the film/substrate system. The delamination process can be divided into three different schemes:

a) Delamination followed by breaking of the delaminated film such that only a narrow strip of film is left behind the crack tip.

b) Delamination with a long plate of non-buckling film left behind the crack tip.

c) As above, but with buckling of the film.

The crack driving force given in equation 4.36 corresponds to situation a) described above. The film stress σ used in this expression is then the sum of the radial stress caused by the indentation and the residual stress in the film. Situation b) with an unbuckled plate of film left behind the crack would cause a constraint on the film cracking and thus reducing the crack driving force $\mathcal{G}_{del}$. This effect increases with the size of the region of intact film behind the crack front. However, for a region of intact film covering as much as half of the delaminated area, this effect is very limited (Drory and Hutchinson, 1996). Film buckling as in situation c) would increase the driving force compared to situation a) as seen in equation 4.44 (this equation is not the exact description of this situation). However, this mechanism is assumed to cancel out any effect of situation b) and is not pursued any more in the paper.

Other studies to determine thin film delamination properties by indentation take buckling into account (De Boer and Gerberich, 1996; Marshall and Evans, 1984). These analyses uses indentation on a much smaller scale than (Drory and Hutchinson, 1996) and the present study.

In the analyses in this work, the interface toughness is assumed to be of much larger magnitude than the film toughness. Interface delamination is thus not analysed any further in the present work.

Chapter 5

Investigation of substrate plasticity and crack spacing

5.1 Introduction

The stress state in the film-substrate system where film cracking occurs is complex. The film is loaded through the displaced substrate. As a result of the high-load indentation, large-scale yielding occurs in the substrate. An FEM study is performed to investigate the steady state channel crack energy release rate $\mathcal{G}_{ss}$ in this situation.

The applied FEM model is developed from the model described in section 3.3. Instead of an indentation problem, a parallel crack array is investigated. A sketch of the model can be seen on figure 5.1 The calculations are made using the commercial FEM code MSC.Marc. Both film and substrate are modelled as elastically isotropic. The film is modelled as ideally elastic and the substrate is treated as an elastic-perfectly plastic material. As it will be demonstrated, no significant difference between isotropic and kinematic hardening is observed. The situation is analysed as a plane strain problem and four-node, plane strain quadrilaterals are used. Since plane strain conditions are applied, the output strain matrix is

$$\boldsymbol{\epsilon} = \begin{bmatrix} \epsilon_{xx} & \epsilon_{xy} & 0 \\ \epsilon_{xy} & \epsilon_{yy} & 0 \\ 0 & 0 & 0 \end{bmatrix} \tag{5.1}$$

The mesh is refined towards the crack. At the crack path, the element size is set to $h/100$ in order to obtain detailed information of the crack energy release rate. Convergence studies are performed in order to ensure the chosen mesh resolution accurately captures the results.

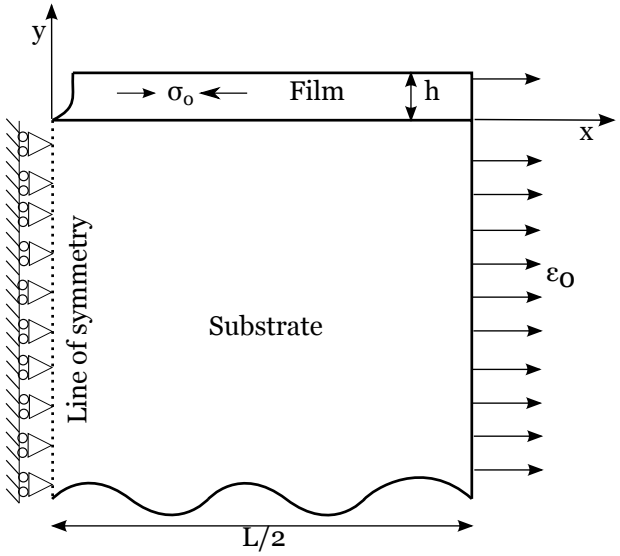

Figure 5.1: Illustration of the array FEM model

A film with thickness h is perfectly bonded to the substrate. The load can be applied with two different methods. Firstly, the structure can be loaded with a uniform strain, ϵ_0. Secondly, a built-in feature in the FEM code is used to apply a residual stress σ_0 in the film. This is beneficial since much existing work is made to investigate residually stresses films, (Beuth, 1992; Beuth and Klingbeil, 1996; Delannay and Warren, 1991; Xia and Hutchinson, 2000). Loading the film with a residual stress makes direct comparison with existing solutions easier. The residual stress feature has been verified by comparison with analytical wafer bending models and captures the behaviour accurately.

A crack is stepwise introduced at the left symmetry line to simulate a growing crack. The energy release rate for the crack is then calculated as it grows through the film. The energy release rate for the crack growing towards the film-substrate interface is calculated with a build-in feature in Msc.Marc. Msc.Marc calculates the energy release rate with the virtual crack closure technique (VCCT), (Krueger, 2004; MSC, 2012). The principle of VCCT can be seen on figure 5.2. The mode I energy release rate $G_{\mathrm{I,ps}}$ is calculated from the product of the crack closure force F_{close} and the opening displacement of the nearest nodes δ_n divided by the crack opening surface s_{crack}:

$$G_{\mathrm{I,ps}} = \frac{F_{close}\delta_n}{2s_{crack}} \tag{5.2}$$

The VCCT method is compared with textbook solution to standard fracture

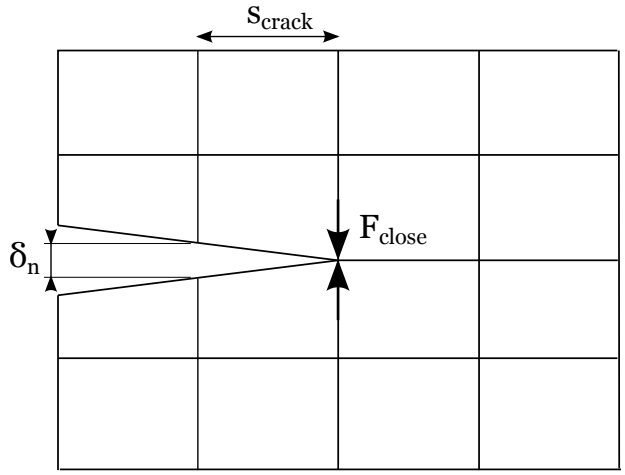

Figure 5.2: Principle of the VCCT method

mechanical problems (Tada et al., 2000) to ensure the correctness of the method. The VCCT results are also compared with a built-in J- integral method. The VCCT and J-integral methods give identical results.

The steady state channel crack energy release rate $\mathcal{G}_{ss}$ can the be calculated from the second expression in equation 4.13.

$$\mathcal{G}_{ss} = \frac{1}{h}\int_0^h G_{ps}(a)da \tag{5.3}$$

The crack is grown incrementally through the film, thus $\mathcal{G}_{ss}$ for all crack depths a/h is calculated.

5.2 Model verification

Verification of residual stress function

In order to verify the residual stress function used to apply the loads, at wafer bending simulation is performed. The simulation is performed as a wafer bending test. The setup of the test can be seen on figure 5.3 The analysis is performed with four-node, axisymmetric quadrilaterals and is linear elastic. Small displacements are assumed in order to fit better with the theory for wafer bending.

Identical elastic and geometrical properties are chosen for the top and bottom body, $E_1 = E_2$, $\nu_1 = \nu_2$, $h_1 = h_2$. The length of the structure L_{wafer} i set to $L_{wafer}/h = 1000$ in order to assure the structure is long compared to the thickness. The top part of the structure is loaded with a

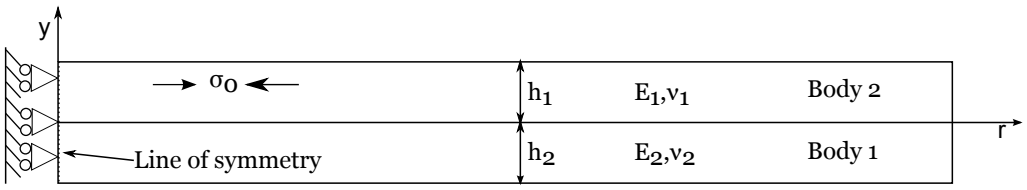

Figure 5.3: analysis set up for wafer bending simulation

compressional, equi-biaxial residual stress σ_0. The residual stress is chosen to $E/\sigma_0 = 200$.

The curvature in a bi-material where $h_1 = h_2$, $E_1 = E_2$ and $\nu_1 = \nu_2$ is given by (Freund and Suresh, 2004, p 100)

$$\kappa_{analytical} = \frac{3}{4}\frac{\sigma_0(1-\nu_2)}{h_2 E_2} \tag{5.4}$$

The mid-plane deflection of the structure can be see on figure 5.4 The

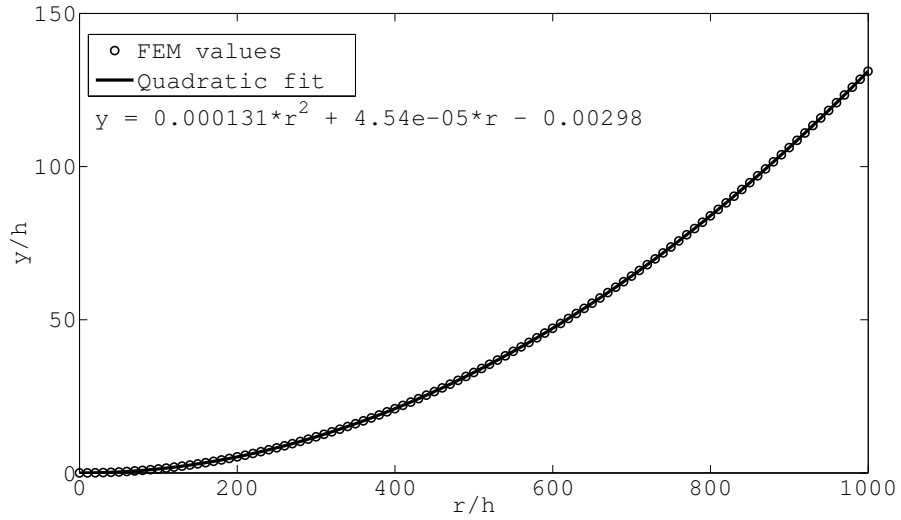

Figure 5.4: Displacement

equation shown is a quadratic polynomial fit for the plotted displacements. The curvature can be calculated from the deflection, y, by

$$\kappa_{FEM} = \frac{d^2 y}{dr^2} \tag{5.5}$$

From equations 5.4 and 5.5 the curvature is calculated as:

$$\begin{aligned} \kappa_{analytical} \cdot h &= 2.63 \cdot 10^{-4} \\ \kappa_{FEM} \cdot h &= 2.62 \cdot 10^{-4} \end{aligned} \tag{5.6}$$

Comparison of isotropic and kinematic hardening

In plasticity theory generally two different hardening theories are used, isotropic and kinematic hardening, (Tvergaard, 2001).

Isotropic hardening is decribed in the J_2 flow theory. Upon loading, the initial yield surface is shaped as a Von Mises yield surface. An example of a Von Mise yield surface can be seen in figure 5.5. Von Mises yield surface

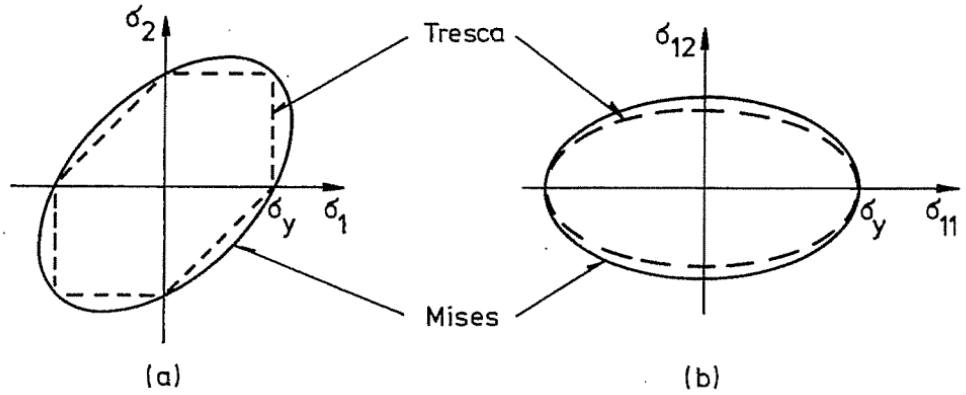

Figure 5.5: Mises yield surface. (a) σ_1 and σ_2 are principal stresses, $\sigma_3 = 0$. (b) σ_{11} and σ_{12} are nonzero as in bending/torsion of a tube

is defined by

$$\sigma_e = \sigma_y \quad , \quad \text{for} \quad \sigma_e^2 = \frac{3}{2} s_{ij} s_{ij} \tag{5.7}$$

Where the stress deviator s_{ij} is given by

$$s_{ij} = \sigma_{ij} - \delta_{ij} \frac{\sigma_{kk}}{3} \tag{5.8}$$

and δ_{ij} is the Kronecker delta.

When the load is increased, the yield surface increases and the yield surface is given by the expression

$$f(\sigma_{ij}) = (\sigma_e)^2_{max} \tag{5.9}$$

Where $(\sigma_e)_{max}$ is the maximal value the von Mises stress has reached so far in the deformation theory.

In kinematic hardening theory, the yield surface does not expand during loading higher than the initial yield surface. Instead it keep its original size and translates in the stress space, see figure 5.6 The value of the stress

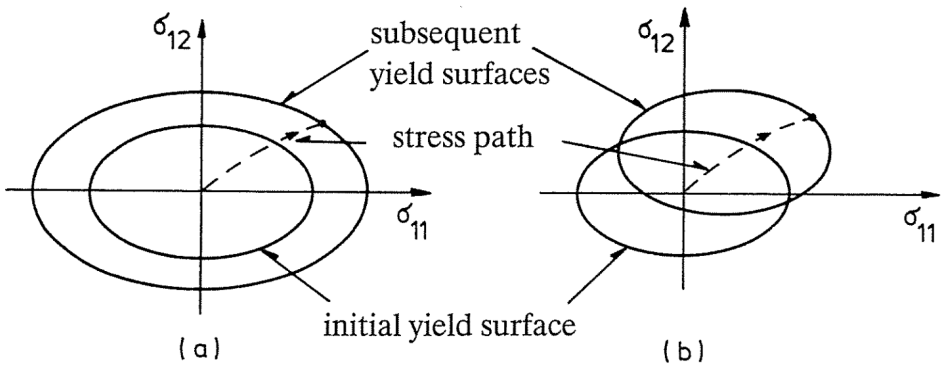

Figure 5.6: Behaviour of yield surfaces upon loading. (a) isotropic hardening, (b) kinematic hardening

tensor in the centre of the yield surface is denoted γ_{ij}, and in the initial state $\gamma_{ij} = 0$ i.e. initially, the yield surface has centre in the origin of the stress space as for isotropic hardening. The yield surface is assumed to be given by the expression

$$f(\sigma_{ij}, \gamma_{ij}) = \frac{3}{2}\tilde{s}_{ij}\tilde{s}_{ij} = \sigma_y^2 \tag{5.10}$$

where $\tilde{\sigma}_{ij} = \sigma_{ij} - \gamma_{ij}$ and $\tilde{s}_{ij} = \tilde{\sigma}_{ij} - \delta_{ij}\tilde{\sigma}_{kk}/3$.

If uniaxial tension is followed by uniaxial compression, J_2 flow theory describes that the compressive yield strength increases in size equal to the tensional yield strength. Kinematic hardening describes that the compressive yield strength decreases when the tensile yield strength is increased by plastic hardening. This is known as the Bauschinger effect. The principle of this can be seen in figure 5.7. It can also be seen that as long as cyclic loading does not occur, the two hardening schemes behave much alike, especially when there are no abrupt changes of the load path.

The difference between isotropic and kinematic hardening is investigated. The results are checked with two methods. Firstly, the extent of the plastic zone is compared for the two hardening behaviour models and secondly, G_{ps} for the two different cases are compared. The results can

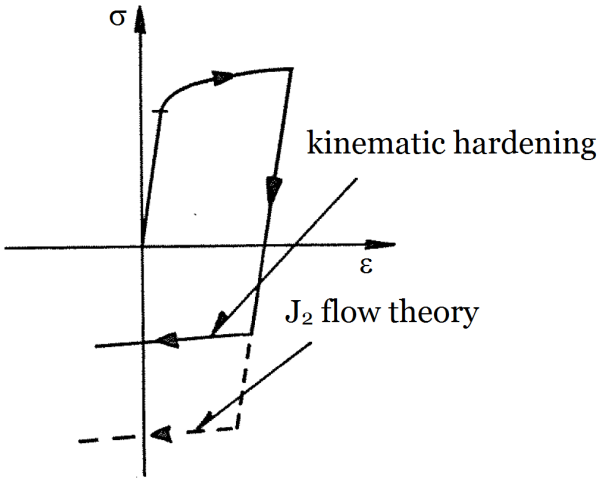

Figure 5.7: Difference between isotropic and kinematic hardening in uniaxial tension - and compression test

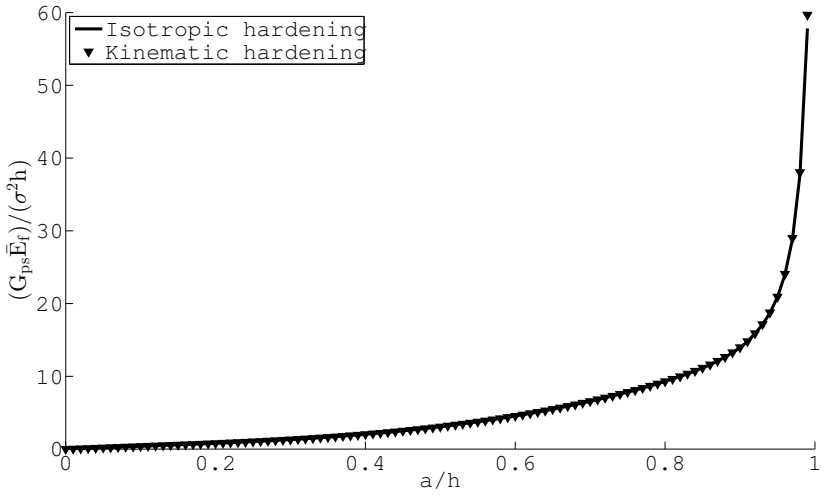

Figure 5.8: Comparison of isotropic and kinematic hardening

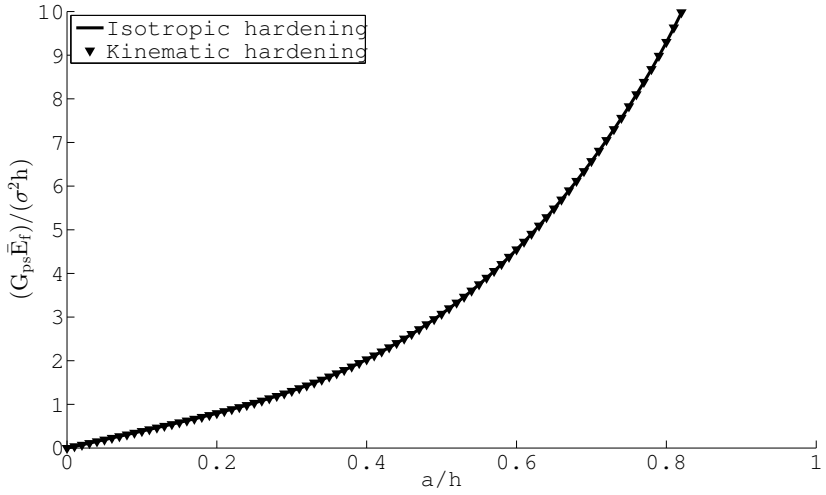

Figure 5.9: Comparison of isotropic and kinematic hardening, closeup

be seen in figures 5.8 and 5.9. The figure shows the plane strain crack driving force G_{ps} for varying crack depths a/h. The calculations are made for an elastic homogeneous system loaded with a residual stress σ_0. The yield strength of the substrate is chosen to $\sigma_0/\sigma_y = 50$ as is is assumed that the difference between the two methods are most significant for large-scale yielding.

The results shows no significant differences between isotropic and kinematic hardening.

Comparison of J-integral and VCCT results

MSC.Marc is capable of calculating the energy release rate with two methods, the J-integral method and the VCCT method. The two methods are compared, see figures 5.10-5.11. The two methods give results that are very close to each other. For results very close to the interface, the results differ. The behaviour of the VCCT curve is in better correlation with litterature, (Beuth, 1992; Shenoy et al., 2001), than the J-integral results. For that reason, the VCCT method is chosen.

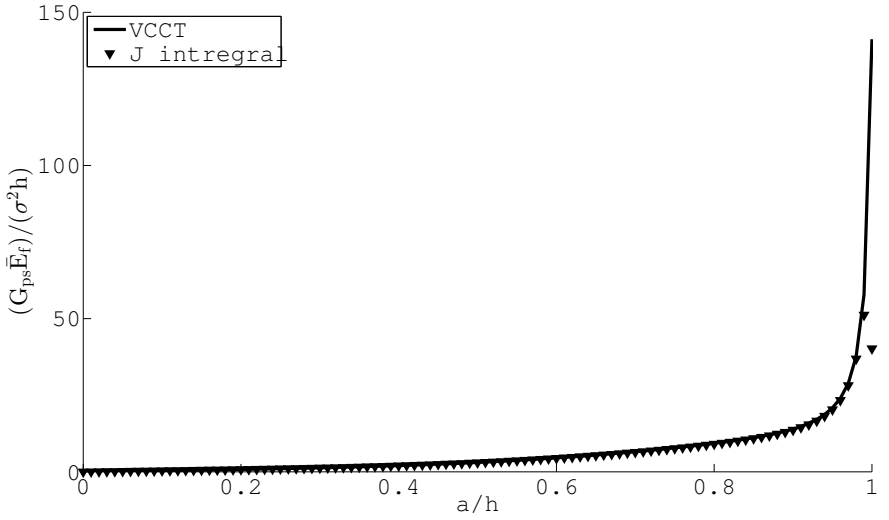

Figure 5.10: Comparison of isotropic and kinematic hardening

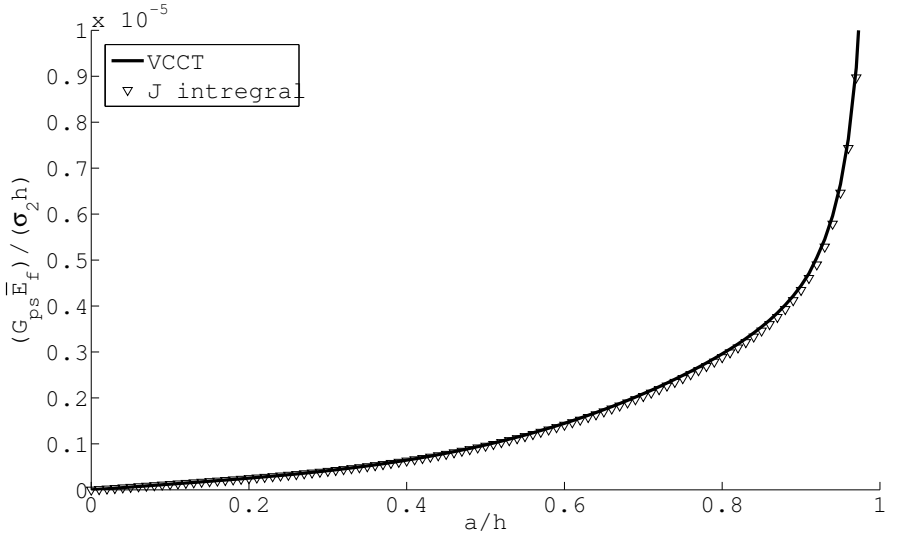

Figure 5.11: Comparison of isotropic and kinematic hardening, closeup

Comparison with literature

In order to verify the model, results are compared with results from the literature. The channel crack problem is described in (Beuth, 1992; Hutchinson and Suo, 1992; Shenoy et al., 2001; Thouless, 1990; Thouless et al., 1992). However, substrate plasticity is not included in the majority of these investigations. The pioneer work of channelling cracks involving plasticity is done by (Beuth and Klingbeil, 1996). The situation analysed by Beuth and Klingbeil is the pressurised crack problem sketched in figure 5.12. The stress state at the crack tip in this problem corresponds to the problem of a film under residual stresses analysed in (Beuth, 1992). A normalised crack

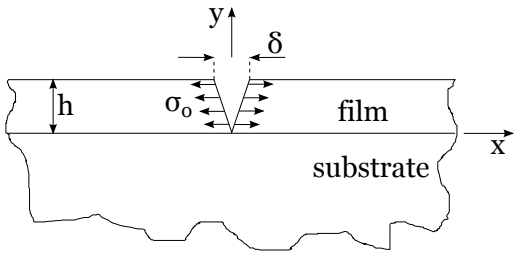

Figure 5.12: Principle of the pressured crack problem

driving force $g\left(\alpha, \beta, N, \sigma/\sigma_y\right)$ is introduced. This can be calculated from $\mathcal{G}_{ss}$ from

$$g\left(\alpha, \beta, N, \frac{\sigma_0}{\sigma_y}\right) = \frac{\mathcal{G}_{ss} 2\bar{E}_f}{\pi \sigma_0^2 h} \tag{5.11}$$

Where α and β are Dundurs' parameters, N is the strain hardening exponent from a Ramberg-Osgood material model (see e.g. equation 3.1) and σ_y is the yield strength of the substrate. The steady state channel crack driving force $\mathcal{G}_{ss}$ is obtained by a through-thickness integration of G_{ps}, the plane strain crack driving force found by the VCCT method in the FEM analysis, see equation 5.3.

As a validation of the current FEM model, the results are compared with the result given by Beuth and Klingbeil. The results can be seen in figure 5.13. The graph shows the normalised crack driving force g as a function of the stress ratio σ_0/σ_y. As it can be seen, the results differ from each other very significantly. For the elastic case, the results are very similar but when yielding occurs, the results differ significantly.

The current analysis and the analysis made by Beuth and Klingbeil are conducted differently. Firstly, the material in Beuth and Klingbeil is modelled by a Ramberg-Osgood relation and by an elastic-perfectly plastic model in the current FEM model. However, for the chosen value of

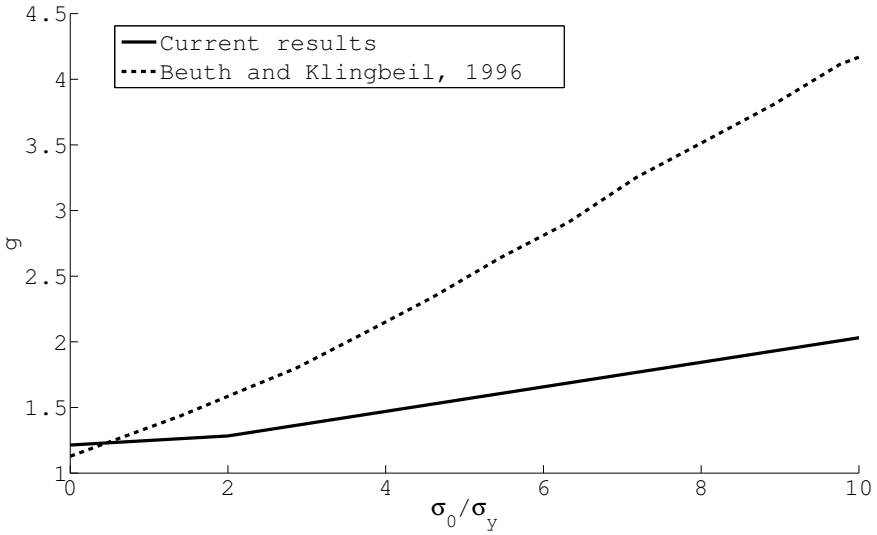

Figure 5.13: Comparison of current FEM model and (Beuth and Klingbeil, 1996)

hardening exponent, the Ramberg-Osgood relation behaves so close to an elastic-perfectly plastic model that this cannot explain the difference.

Secondly, the model in (Beuth and Klingbeil, 1996) is analysed by a pressurised crack instead of the a residual stress applied directly to the film. When choosing the residual stress method for the analysis, comparisons between the pressurised crack and the residual stress models were made, and no significant difference were seen.

Thirdly, in the analysis made by Beuth and Klingbeil, g was obtained in a different manner than for the current model. In (Beuth and Klingbeil, 1996), a through-thickness crack is modelled and the load is ramped up in order to obtain a σ_0 vs Δ graph. The definition of Δ is the integral of the crack-opening displacements through the film:

$$\Delta = \int_0^h \delta_c(y)dy \tag{5.12}$$

The $\sigma_0(\Delta)$ function is integrated in order to obtain the work W done by the uniform pressure σ_0

$$W = \int_0^\Delta \sigma_0(\Delta)d\Delta \tag{5.13}$$

The normalised crack driving force g is then given by

$$g = \frac{\sigma_0\Delta}{\frac{\pi}{2\bar{E}_f}(\sigma h)^2} \tag{5.14}$$

This method is also implemented in order to compare the results. The method gives results similar to using equation 5.3 but they still differ significantly.

A substantial amount of work is done in order to assure the correctness of the currently used FEM model. A number of possible causes for the differences between the current model and the model made by Beuth and Klingbeil has been investigated but none of these can explain the different results.

5.3 Substrate yield strength

The influence of the substrate yield strength σ_y on the plane strain crack driving force G_{ps} and thus $\mathcal{G}_{ss}$ is investigated. The investigation is made by introducing a uniaxial residual stress σ_0 acting on the film. A crack is then gradually grown through the film towards the interface and and G_{ps} is calculated for each crack opening step. The elastic properties of the film and substrate are chosen to be identical in order to isolate the effect of substrate plasticity, thus $E_f/E_s = 1$ and $\nu_f/\nu_s = 1$. The substrate yield strength is varied from the elastic case $\sigma_0/\sigma_y = 0$ to $\sigma_0/\sigma_y = 100$.

The results can be seen in figures 5.14 and 5.15. It can be seen that

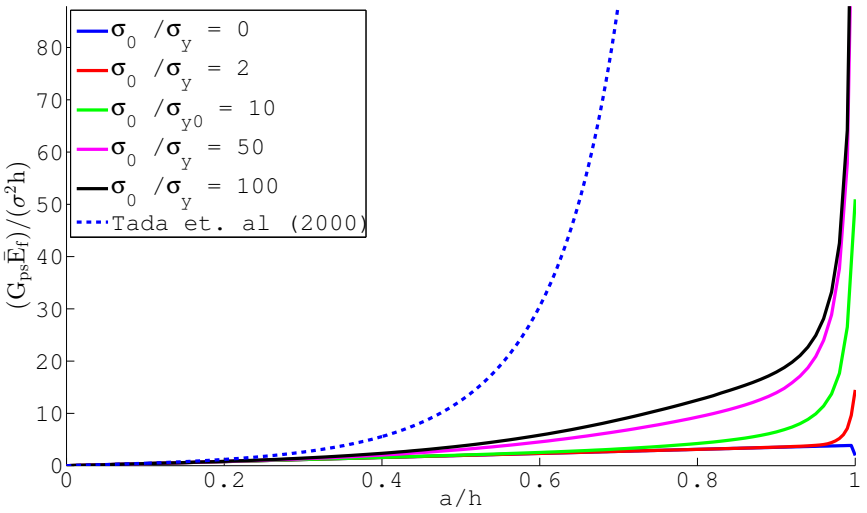

Figure 5.14: Driving force for plane strain crack growing towards the interface for varying substrate yield strength

the crack driving force increases with the crack length as the crack grows

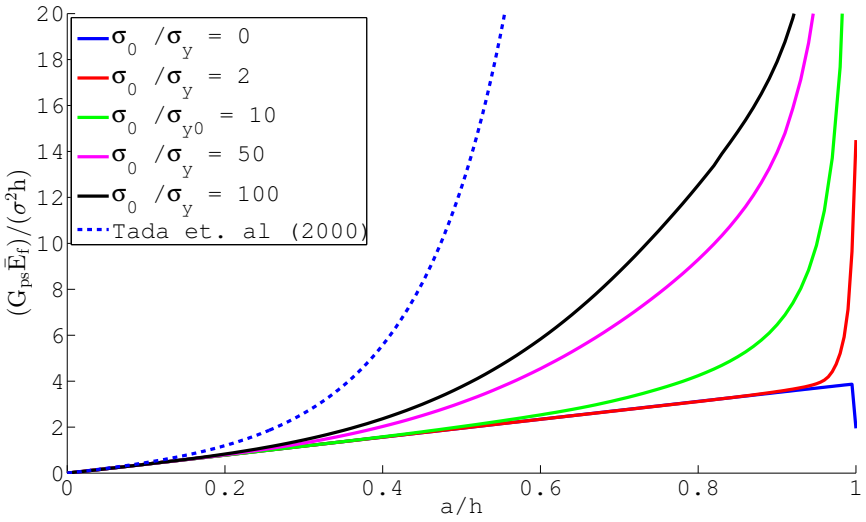

Figure 5.15: Driving force for plane strain crack growing towards the interface for varying substrate yield strength, closeup

towards the interface. For the linear case, $\sigma_0/\sigma_y = 0$, G_{ps} has a linear dependence of a/h. When the substrate yields, the driving force grows faster than a linear dependence. For a moderately yielding substrate, $\sigma_0/\sigma_y = 2$ the crack is close to the interface before the driving force starts to increase faster than the linear case. For higher value of σ_0/σ_y the crack driving force diverges from the elastic case for low crack depths. The crack driving force is also of larger magnitude for low substrate yield strengths.

This is somewhat in opposition to intuition. When a crack in a homogeneous material approaches a plastic zone, this zone shields off the crack driving force by dissipating the energy that otherwise would go to crack propagation and thus causes the driving force to decrease. Here, the opposite happens. This can be explained by interpreting that a decrease in yield strength will decrease the constraint effect from the substrate on the film thus causing the film to displace more freely.

In figure 5.14 the expression for a crack in a single edge notch test specimen is plotted, see figure 5.16. This is a standard fracture mechanical test geometry with a handbook solution, for instance (Tada et al., 2000).

Even for a very low value for the yield strength, $\sigma_0/\sigma_y = 100$ the resulting crack driving force still differs significantly from the results for the single edge notch test specimen which corresponds to a system where the substrate does not constraint film cracking at all. It is also very clear from figure 5.14 that a low substrate yield strength give lower constraint on the

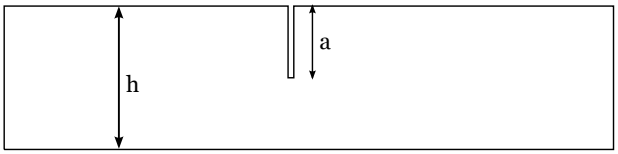

Figure 5.16: Single edge notch test specimen layout

film and thus a higher crack driving force.

The direct influence of σ_0/σ_y on $\mathcal{G}ss$ can be seen on figure 5.17. As

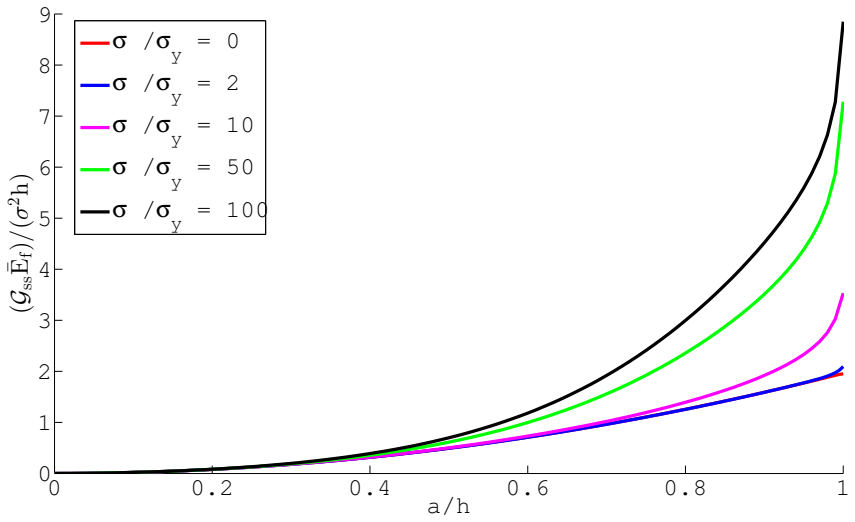

Figure 5.17: Driving force for steady state crack growing towards the interface for varying substrate yield strength

expected from figure 5.14, $\mathcal{G}ss$ increases with decreasing yield strength of the substrate.

5.4 Crack spacing

The influence of crack spacing on the crack driving force is investigated. (Shenoy et al., 2001; Thouless, 1990; Thouless et al., 1992; Xia and Hutchinson, 2000) states that parallel arrays of cracks "shields" off each other so that the driving force decreases for cracks close to each other. However, none of these investigations include yielding. In the current analysis, the model is loaded by a uniaxial residual stress σ_0. The yield stress is fixed at $\sigma_0/\sigma_y = 5$ in order to focus on the effect of crack spacing. The model is

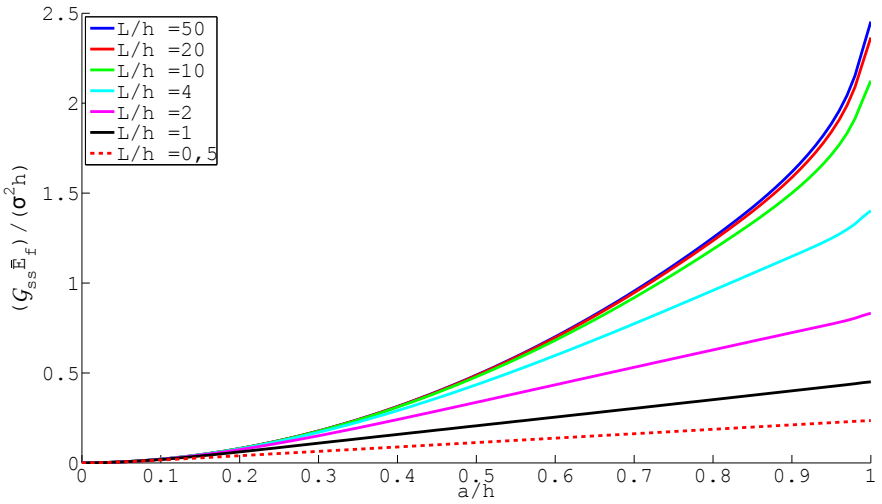

Figure 5.18: Crack driving force as a function of depth for different crack spacings

identical to the model sketched in figure 5.1. The crack spacing L is varied from $L/h = 0.5$ to $L/h = 50$ in order to investigate the influence of crack yielding. Only half the area between two neighbouring crack is modelled and symmetry boundary conditions are applied at the right boundary. The elastic properties of film and substrate are identical, $\bar{E}_f/\bar{E}_s = 1$, $\nu_f/\nu_s = 1$ again to isolate the crack spacing effect. The normalised channel crack driving force $(\mathcal{G}_{ss}\bar{E}_f)/(\sigma^2 h)$ as a function of crack spacing L/h can be seen on figure 5.18. The channel crack driving force for crack in an parallel array at varying depths has been investigated by (Shenoy et al., 2001). The results can be seen in figure 5.19. Shenoy et al. shows that for decreasing crack spacing the crack driving force also decreases. This is in good correlation with (Huang et al., 2013; Thouless, 1990; Thouless et al., 1992; Xia and Hutchinson, 2000) that comes to the same qualitative result. Figure 5.19 also shows that for large spacings, the $\mathcal{G}_{ss}$ vs a/h curve is close to linear. For closer spacings, $\mathcal{G}_{ss}$ increases slower than linear with increasing a/h. The slope decreases more for small crack spacings and for $L/h = 1$ the driving force is nearly constant for $a/h \gtrapprox 0.5$ This means that the channelling crack is not very likely to grow to a through-thickness crack for close spacings since a maximum on the crack driving force curve means that the channelling crack does not grown deeper than the place for this maximum.

The present results in figure 5.18 shows a different trend. The driving force for high spacings increases rapidly and not linear like the elastic results

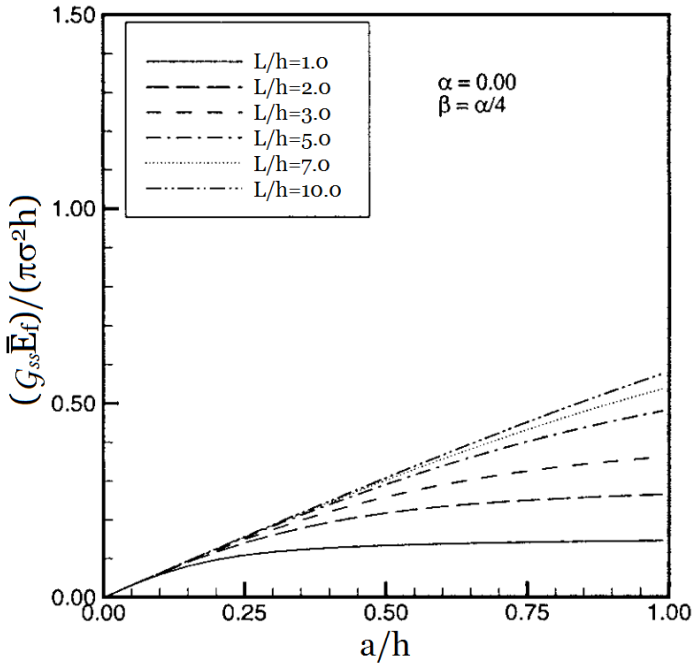

Figure 5.19: Crack driving force for different crack spacings, elastic substrate, (Shenoy et al., 2001)

from Shenoy et al. For narrower spacings, the trend is more like the elastic solution. This implies that for more dense crack arrays, substrate yielding has lesser influence. This is also in good correlation with the common understanding from (Hutchinson and Suo, 1992; Thouless, 1990; Thouless et al., 1992) that closely spaced crack shields off each other.

If the stresses in the film at tip and in front of the crack is of smaller magnitude, the substrate yielding would be less profound. Figure 5.20 shows the size of the plastic zone for $L/h = 50$ and $L/h = 0.5$ The plastic zone on figure 5.20b is much smaller than for the large spacing shown in figure 5.20a. The investigation in section 5.3 showed that plastic yielding decreases the substrate's constraining effect on the film. A small plastic zone gives more constraint on the film and the result thus is similar to the elastic case.

The classic solution for an array of cracks in an elastic homogeneous system (Thouless, 1990), equation 4.16, states that for an spacing larger that $L/h \approx 8$, no crack interaction occurs and the solution for $\mathcal{G}_{ss}$ is the same as for a single channelling crack. In figure 5.18, the driving force curves are nearly identical for $L/h \geq 10$.

The normalised channel crack driving force as a function of crack spacing

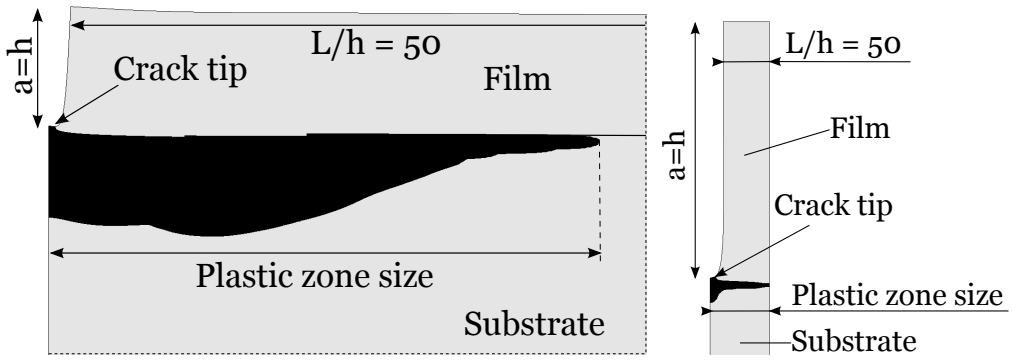

(a) $L/h = 50$ (b) $L/h = 0.5$

Figure 5.20: Plastic zone size for $L/h = 0.5$ and $L/h = 50$. For $L/h = 50$, figure (a) does not show the entire model width

L/h can be seen on figure 5.21. The graph shows that the driving force does

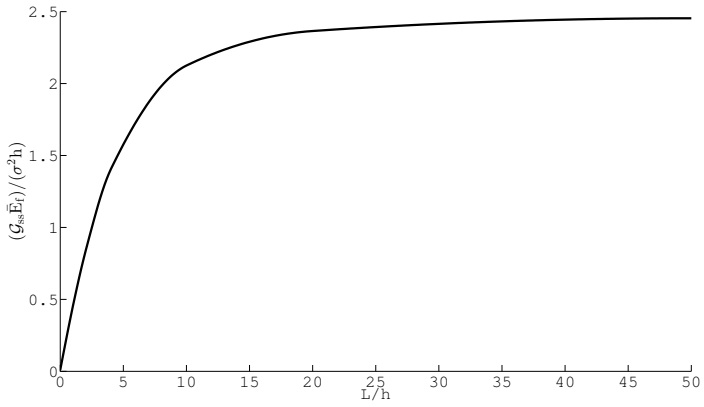

Figure 5.21: Crack driving force as function of crack spacing

not increase for L/h greater that approximately 10 to 15. The exact location is not accurately captured on the figure.

5.5 Film bending

The stresses in the film in the area away from the crack edge are also investigated.

Figure 5.22 shows the displaced film at the crack edge for a fully grown crack, i.e. $a/h = 1$. It shows that the film is bent upwards during cracking.

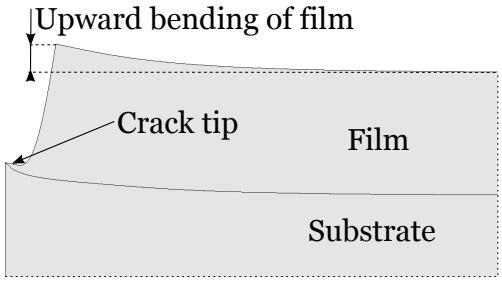

Figure 5.22: Contour of displaced fem analysis geometry (exaggerated)

For that reason, the stresses caused by bending of the film is investigated. Bending stress causing the film to bend upwards causes tensile stresses at the crack tip normal to the interface and thus delamination might occur. In the following analysis, the film is assumed perfectly bonded to the substrate and delamination is not investigated any further. Figure 5.23 shows the stresses in the film at the top and bottom. The plot shows that close to the

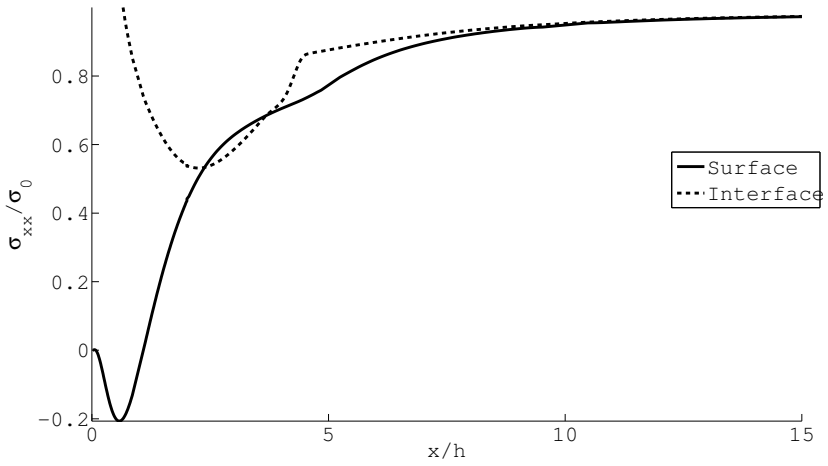

Figure 5.23: Stresses in the film at the film surface and at the film/substrate interface, $\sigma_0/\sigma_y = 5$, $L/H = 50$

crack tip, the stresses at the top of the film is compressive while at the film-substrate interface, the stresses shows quite large tensile value. This implies that bending of the film plays a significant role in the film stress state close to the crack edge. When moving away from the crack edge the bending influence on the film stresses decreases and for a distance at $x/h \approx 7 - 8$ the effect is negligible.

Surface stresses at different crack spacings

To get a more direct view on, how the crack shields off each other at close crack spacings, the surface stresses σ_{xx} in the area between two crack faces are plotted in figures 5.24-5.25. For the larger crack spacings, $L/h \geq 4$,

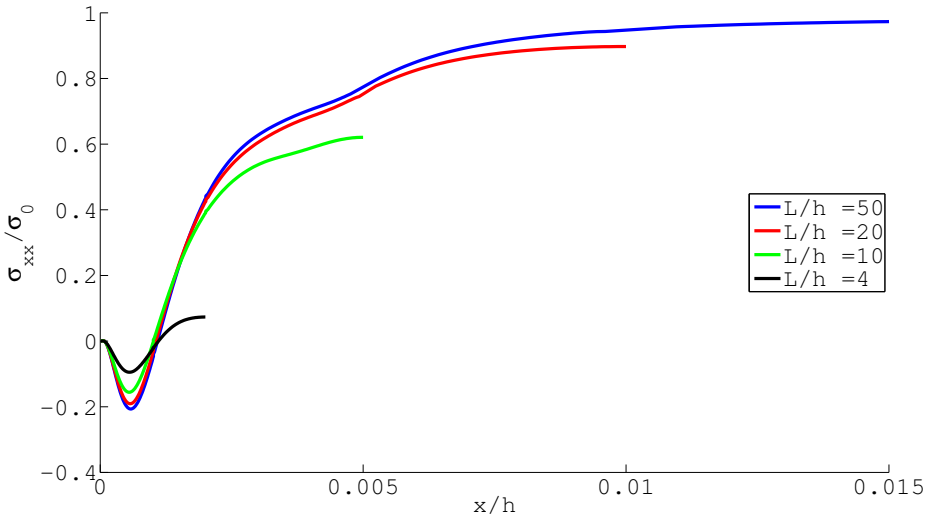

Figure 5.24: Surface stresses in crack array between the cracks, $\sigma/\sigma_y = 5$

the stress distributions show the same trend. For $L/h = 50$ and $L/h = 20$ the curves are virtually identical. This is in good correlation with earlier results saying that for large crack spacings, no effect of the next cracks can be seen. For $L/h = 10$ and $L/h = 4$, the stress distributions show the same trend but the magnitude of σ_{xx}/σ_0 is smaller. This is explained by the shield-off effect of the adjacent cracks.

Due to bending of the film, the surface stresses reaches a minimum value close to the crack tip. This minimum is reached at nearly the same location for all graphs $4 \leq L/h \leq 50$. The surface stress then increases until it reaches maximum for $x/h = 0.5L/h$ which is midway between two adjacent cracks. From this location, the surface stress will decrease towards the adjacent crack, but this is not simulated.

When the cracks are closer spaced, the stresses do not follow the same trend. Film bending then dominates the stress state in the film and the stresses reach a minimum value half way between two adjacent cracks. This implies that for close spaced cracks, a new crack would not be likely to nucleate since the surface of the film is in a compressive stress state.

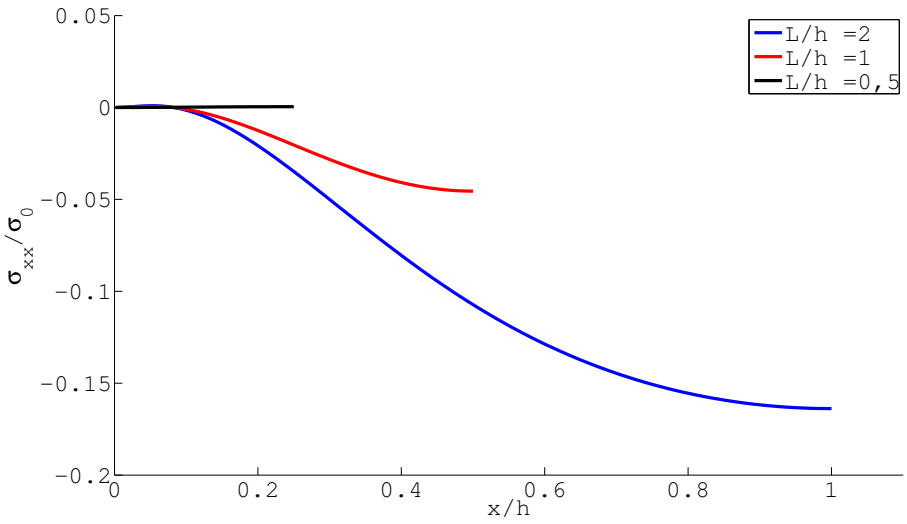

Figure 5.25: Surface stresses in crack array between the cracks, closeup. $\sigma/\sigma_y = 5$

Relaxation distance and shear lag model

The plots in figure 5.24 shows that it takes a distance some times the film thickness to build up the prescribed σ_0 when moving away from the crack. For large-scale yielding, this effect is explained with the shear lag mode, see section 4.2. An analysis of this distance is made with the current FEM model to compare with the shear lag model.

A "relaxation distance" δ_{relax} is defined as the distance x/h away from the crack face where the surface stresses in the film has recovered to 90% of the nominal stress σ_0. The result can be seen in figure 5.26 In the shear lag model, the distance for stress build-up is defined by the slip length:

$$\frac{L_{slip}}{h} = \sqrt{3}\frac{\sigma_0}{\sigma_y} \tag{5.15}$$

Figure 5.26 shows that the shear lag overestimates the distance needed for stress recovery compared to the values calculated in the current FEM analysis. The shear lag model is a simple model based on a yielding interface and not large-scale yielding in the entire substrate as such. The effect of film bending shown in figure 5.23 is not taken into consideration in the shear lag model. For small-scale yielding, the FEM results give a larger recovery distance than the shear lag model. The shear lag model is intended for use in large-scale yielding, $\sigma_0/\sigma_y > 10$ and the difference for the small-scale yielding is in good correlation with this.

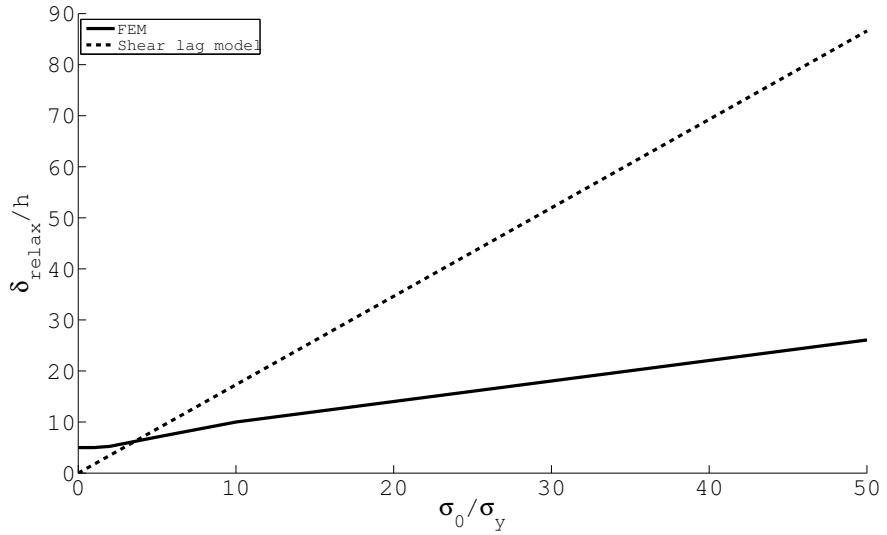

Figure 5.26: Comparison of FEM relaxation distance and shear lag model

For more distinct yielding, the shear lag model give substantial larger recovery distances than the FEM values. This implies that the shear lag model is not very accurate to describe the cracking mechanisms on a crack array when large-scale yielding is present.

Part III

Coupling of stresses and crack mechanisms

Chapter 6

Fracture toughness determination

6.1 Introduction

The scope of this analysis is to establish a method to determine the thin film fracture toughness Γ_f from the crack patterns arising from a Rockwell indentation of the film/substrate system. An example of the radial crack pattern arising from a Rockwell indentation can be seen in figure 6.1. This

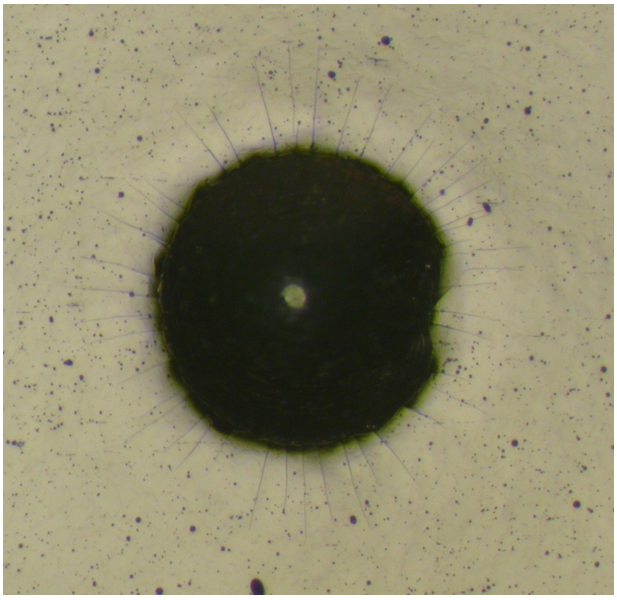

Figure 6.1: Radial cracks spreading from a $15kg$ Rockwell C indentation of a Al_2O_3 film on a AISI 316L substrate, (Madsen, 2010)

is done by linking the models for thin film stresses presented in chapter 2 with the models for channelling crack propagation presented and treated in chapter 4. In this chapter, these results are applied to the indentation case, where the cracks spread out radially from the indentation. It is assumed that the results are also applicable for radial propagation. This assumption is accurate if the indentation radius R_i is large compared to the crack length c and the crack spacing L.

6.2 Theory

The fracture toughness of the film can be evaluated using the fracture criterion

$$\mathcal{G}_{ss} = \Gamma_f \tag{6.1}$$

Where $\mathcal{G}_{ss}$ is the steady-state energy release rate and Γ_f is the fracture toughness of the coating.

In chapter 4, a number of models for propagation of arrays and single channelling cracks are treated and compared. The models can all be presented in the form.

$$\frac{L}{h} = F\left(h, \sigma(r), E_{film}, \nu_{film}, \Gamma_f\right) \tag{6.2}$$

The film thickness h, the film elastic properties E_{film}, ν_{film} and the crack spacing L/h are known values in the analysis. In general, the film stress can consist of two components, $\sigma(r) = \sigma_0 + \sigma_{\theta\theta}(r)$. Here $\sigma_{\theta\theta}(r)$ is the circumferential stress given by the FEM analysis description in section 3.3 and σ_0 is the equi-biaxial residual stress. Assuming that the cracks are initiated at the indentation edge $r = R_i$ and arrest at $r = R_i + c$ where c is the crack length, the expression in equation 6.2 can be written for two values of L/h and $\sigma(r)$.

$$\frac{L_0}{h} = F\left(h, \sigma(r = R_i), E_{film}, \nu_{film}, \Gamma_f\right) \tag{6.3}$$

and (6.4)

$$\frac{L_1}{h} = F\left(h, \sigma(r = R_i + a), E_{film}, \nu_{film}, \Gamma_f\right) \tag{6.5}$$

Given the two values of L/h for crack initiation (L_0/h) and crack arrest (L_1/h) the two unknown values σ_0 and Γ_f can be determined.

Crack regimes as a function of residual stress

Thin film can experience residual stresses of significant magnitude. These stresses often arise from the mismatch in the coefficient of thermal expansion between substrate and film. For thin films and very shallow indentation depth, the material length scale and grain size may have influence on the stresses. As discussed previously in section 2.6, this effect is not included here. The equi-biaxial residual stress can be described by a dimensionless number t:

$$t = \frac{\sigma_0(1-\nu^2)}{E_f} \tag{6.6}$$

If cracks are initiated at the indentation edge, the crack propagation may fall into three different regimes depending on the sign and magnitude of the residual stresses.

(a) For no residual stress, for small compressive stresses and for tensile residual stresses below a critical value, $\sigma_{0,critical}$, the cracks will arrest some distance from the indenter when the circumferential stress drops below a value σ_{arrest}. The value of σ_{arrest} is determined from the models for crack propagation and interaction.

(b) If the residual stresses are higher than $\sigma_{0,critical}$ the cracks will not arrest and the film suffers complete failure by unlimited channelling cracking.

(c) For compressive stresses of high magnitude, the film stresses may not become high enough to initiate crack growth and no radial cracks will form.

A schematic illustration of the different cracking regimes can be seen on figure 6.2.

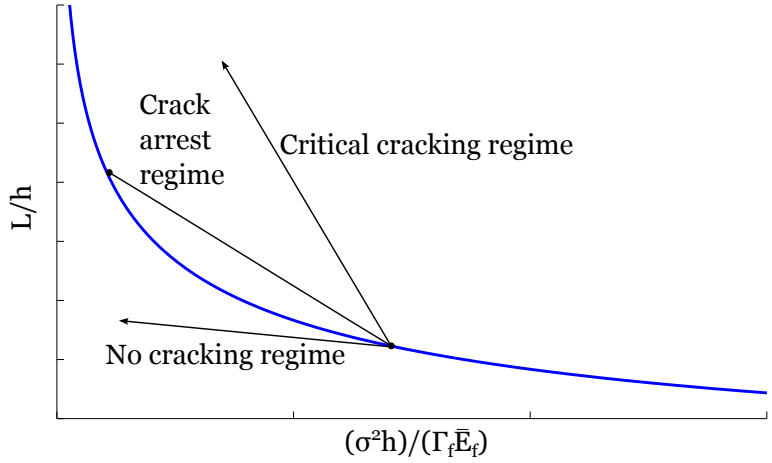

Figure 6.2: Schematic illustration of the different cracking regimes

6.3 Implementation of analysis

Two different film/substrate systems are analysed. The first system is a TiN film of an ASP23 tool steel substrate. The second is a Al_2O_3 film on aa AISI 316L stainless steel substrate.

TiN-ASP23

The mechanical properties for the system can be seen in table 6.1. Not all values are given for the current system. The given values are the film thickness h and the substrate hardness H. The Young's modulus E, Poisson's ratio ν and film fracture toughness Γ_f are taken from literature for a similar system (Holmberg et al., 2003). The substrate yield stress σ_y is calculated from the hardness value.

	E $[GPa]$	ν $[-]$	σ_y $[MPa]$	H $[H_v]$	Γ_f $[J/m^2]$
Film (TiN)	300	0.3	-	-	149
Substrate (ASP23)	210	0.3	2681	820	-

Table 6.1: Elastic and plastic properties for the simulated TiN-ASP23 system

No yield stress value or post-yield material behaviour is given for the analysed ASP23 tool steel substrate. For that reason, the material is as-

sumed to be elastic-perfectly plastic. The yield stress is determined from the indentation hardness. For metals, an approximate relation between the yield strength σ_y and the indentation hardness H is given by (Johnson, 1970a; Tabor, 1951).

$$\sigma_y \approx \frac{H}{3} \tag{6.7}$$

The Vickers hardness is given in kg_f/mm^2 and the Vickers hardness value must thus be converted to MPa

$$\sigma_y = \frac{H_v \cdot 9.81 \frac{m}{s^2}}{3} \tag{6.8}$$

The input yield strength for the FEM analysis is then determined to $\sigma_y = 2681 MPa$

The indentation radial crack pattern can be see on figure 6.3-6.4.

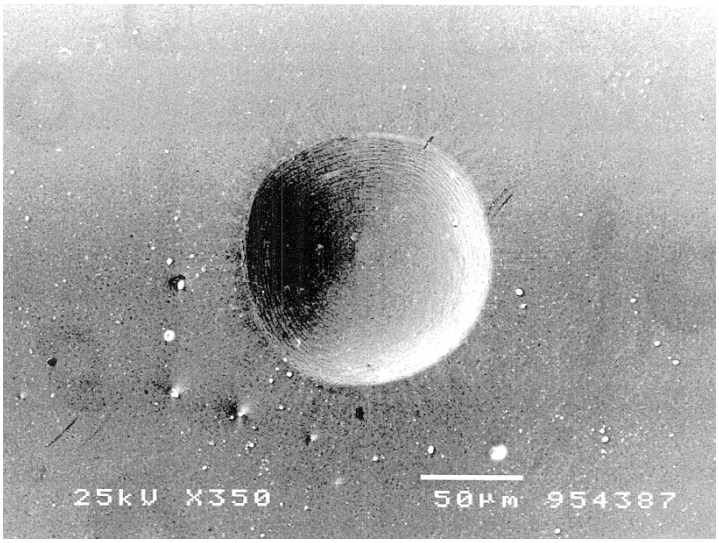

Figure 6.3: $10kg$ Rockwell A indentation of $2\mu m$ TiN on tool steel (ASP23) indentation radius is approx $60\mu m$, (Thomsen, 1998)

The crack pattern data obtained from the indentation pictures are listed in table 6.2

R_i	c	L_0	L_1	h
$[\mu m]$	$[\mu m]$	$[\mu m]$	$[\mu m]$	$[\mu m]$
62.5	28.7	6.6	10.1	2

Table 6.2: indentation crack values from figure 6.3

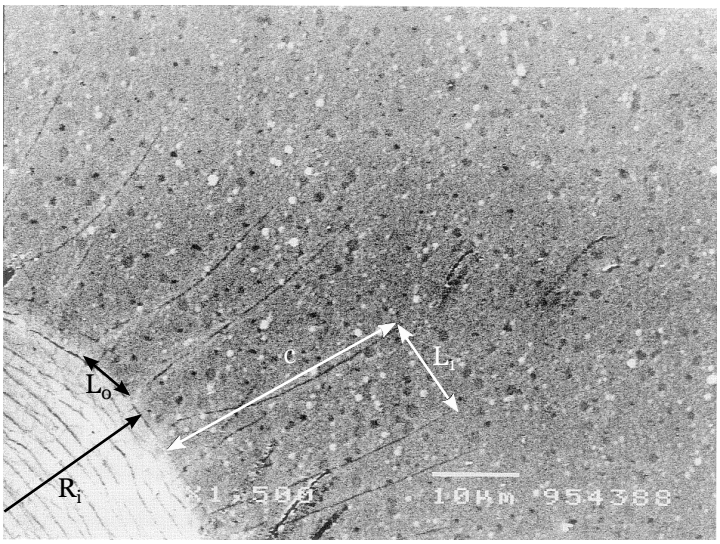

Figure 6.4: Figure 6.3, closeup

Al_2O_3-316L

Another system is also simulated. This system is an Al_2O_3 film deposited on an AISI 316L stainless steel substrate. The properties for this system can be seen in table 6.3. For the substrate, a build-in material model is used which includes the yield stress and the post-yielding plastic response for the material. The material model is from (Doege et al., 1986). The Poisson's ratio for the film is unknown and is assumed to be $\nu_f = 0.3$. The used value for Γ_f is given in (Steffensen et al., 2013). Young's modulus for the Al_2O_3 film is measured by (Madsen, 2010). The analysed crack pattern

	E $[GPa]$	ν $[-]$	σ_y $[MPa]$	Γ_f $[J/m^2]$
Film (Al_2O_3)	213 ± 40*	0.3	-	109
Substrate (AISI 316L)	210	0.3	473	-

Table 6.3: Elastic and plastic properties for the simulated Al_2O_3-AISI 316L system. *: the film Young's modulus is the reduced modulus, $E^* = E/(1-\nu^2)$

can be seen in figure 6.5. Values of crack length and spacing are listed in table 6.4.

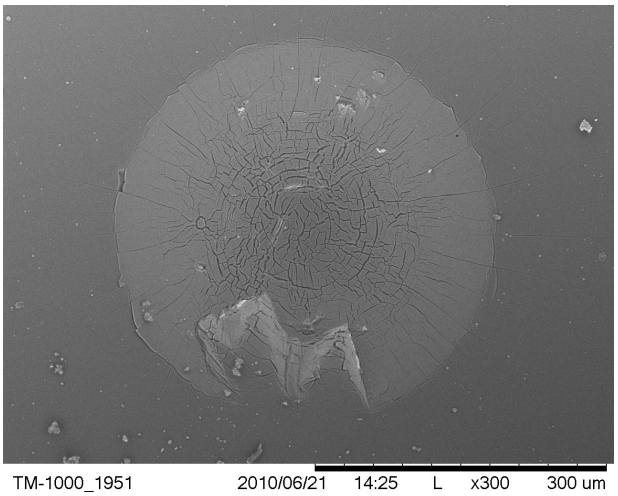

Figure 6.5: $15kg$ Rockwell indentation of a $4.1\mu m$ Al_2O_3 film on an AISI 316L stainless steel substrate

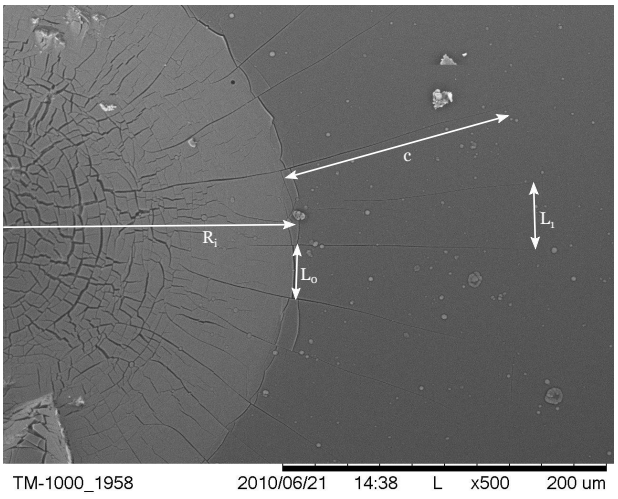

Figure 6.6: Figure 6.5, closeup

R_i	c	h	L_0/h	L_1/h
$[\mu m]$	$[\mu m]$	$[\mu m]$	$[-]$	$[-]$
196	114.6	4.1	5.9	9.1

Table 6.4: indentation crack values from figure 6.5

6.4 Results and discussion

Input surface stresses

The film stresses applied in the analysis are determined by an FEM analysis of the Rockwell indentation, see section 3.3. Two different analyses are carried out. One is a full FEM model of the film-substrate system with the film attached. The film is assumed perfectly elastic and the substrate is assumed elastic-plastic. The film hoop stress $\sigma_{\theta\theta}$ is then found as a direct result from the FEM analysis. Secondly, an indentation of the substrate material without the film applied is simulated. Assuming that the film is perfectly bonded to the substrate, the film stresses can be found from equation 3.3:

$$\begin{aligned}\sigma_{\theta\theta}(r) &= \frac{E}{1-\nu^2}\left(\frac{u(r)}{r} + \nu\frac{du(r)}{dr}\right) \\ &= \frac{E}{1-\nu^2}\left(\epsilon_{\theta\theta}(r) + \nu\epsilon_{rr}(r)\right)\end{aligned} \tag{6.9}$$

The radial and circumferential strains in equation 6.9 are given from the FEM results. This can be done by assuming a perfect bond between the film and substrate giving that the substrate displacement are transferred to the film through the interface. It is also assumed that the film is very thin so that there is no through-thickness strain variation in the film.

TiN-ASP23

The circumferential stress for the analysis with film can be seen in figure 6.7.

For the analysis without film, the film stresses are the found from equation 6.9. The results can be seen in figure 6.8.

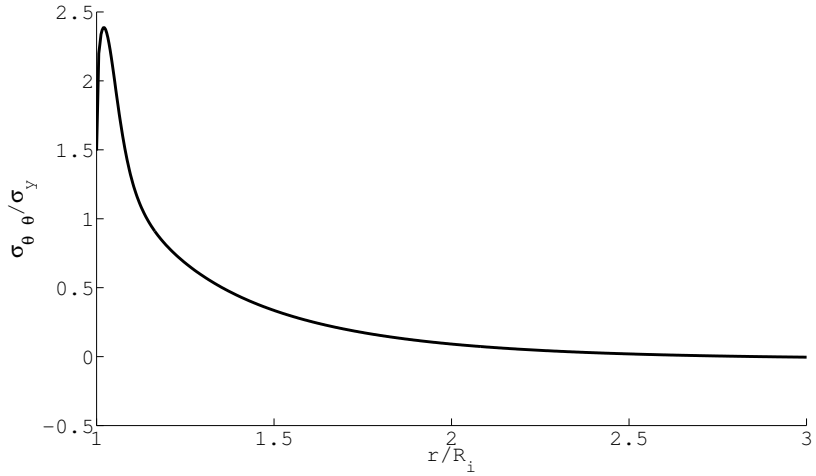

Figure 6.7: Hoop stress distribution for indentation of TiN-ASP23, model with film

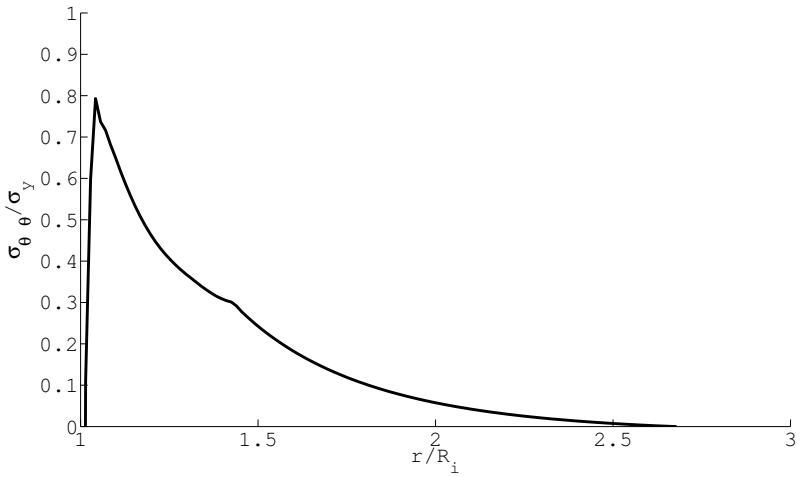

Figure 6.8: Hoop stress distribution for indentation of TiN-ASP23, stresses found from model without film

Al_2O_3-316L

Similar analyses are carried out for the Al_2O_3-316L system. The stress distribution for the analysis with film can be seen on figure 6.9. An analysis

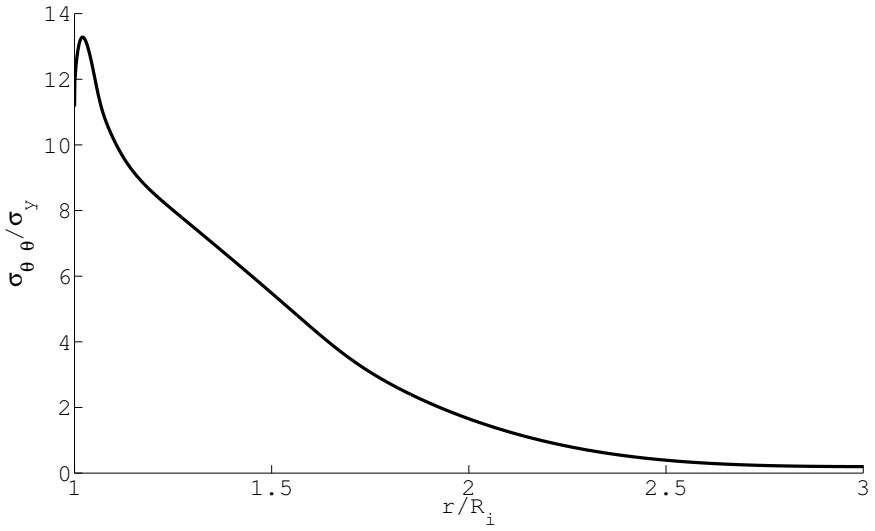

Figure 6.9: Hoop stress distribution for indentation of Al_2O_3-316L, model with film

of the substrate without film as described for the TiN-ASP23 system is also carried out. The stress distribution for this analysis can be seen in figure 6.10.

The stress distributions for the two systems show similar trends. $\sigma_{\theta\theta}$ has maximum value a small distance away from the indentation edge and decreases monotonically with the distance from the indenter. For all the cases analysed, it can be seen that the stresses have a peak value at small distance away from the indentation edge at $r/R_i \approx 1.007$. In this analysis it is assumed that the peak stress determines the crack energy release rate at initiation and thus the peak stress is taken as the stress at $r = R_i$ and $L = L_0$. A specific initiation criterion is not treated here, and thus setting the stress maximum different from the indentation edge would mean the cracks should initiate here instead of at the indentation edge. For that reason, in the following analyses it is assumed that the maximum hoop stress occurs at the indentation edge.

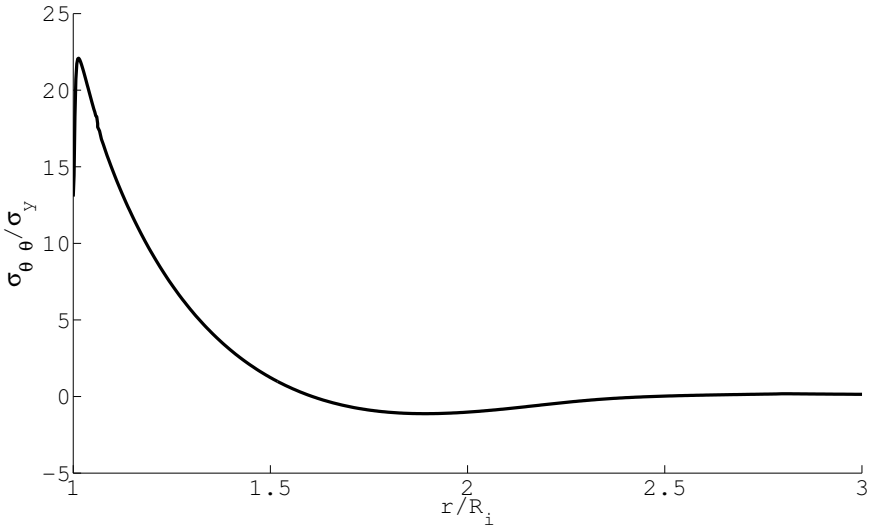

Figure 6.10: Hoop stress distribution for indentation of Al_2O_3-316L, model without film

Crack driving force plots

In order to visualise the crack driving force and the corresponding crack pattern the driving force causes, the current crack driving force given by the FEM analyses presented in figures 6.7-6.10 is presented in a plot similar to figure 4.13. Here the normalised crack spacing L/h is plotted as a function of the normalised crack driving force $(\sigma^2 h)/(\Gamma_f \bar{E}_f)$. The models presented and compared in section 4.2 can be divided in three categories. The model from (Thouless, 1990) is based on the energy release rate for an array of cracks propagating simultaneously. This argument gives a minimum bound for the crack spacing. A second argument from (Thouless et al., 1992) uses an energy argument and gives the crack spacing that minimizes the total energy in the cracked film. This argument gives an upper bound for the crack spacing. A third argument is similar to the first argument but assumes that the advancing crack propagates between two already existing cracks. This argument gives a crack spacing intermediate to the upper and lower bound. These three general models are shown with the current crack driving force in figures 6.11-6.14 for the TiN-ASP23 system and figures 6.16-6.19 for the Al_2O_3-316L system. The solid lines are the described theoretical crack propagation models. Two horisontal black dash-dot line are drawn at L_0/h and L_1/h which are the crack spacings at the indentation edge and crack arrest respectively. A vertical black dash-dot line is drawn at

$(\sigma^2 h)/(\Gamma_f \bar{E}_f) = 1.976^{-1}$ which is the nondimensional driving force for a single channelling crack (Beuth, 1992). This means that at this value, the crack spacing L/h should be greater than $L/h \approx 8$ as described in section 4.2.

TiN

The results for the TiN-ASP23 system can be seen in figures 6.12, 6.13 and 6.14.

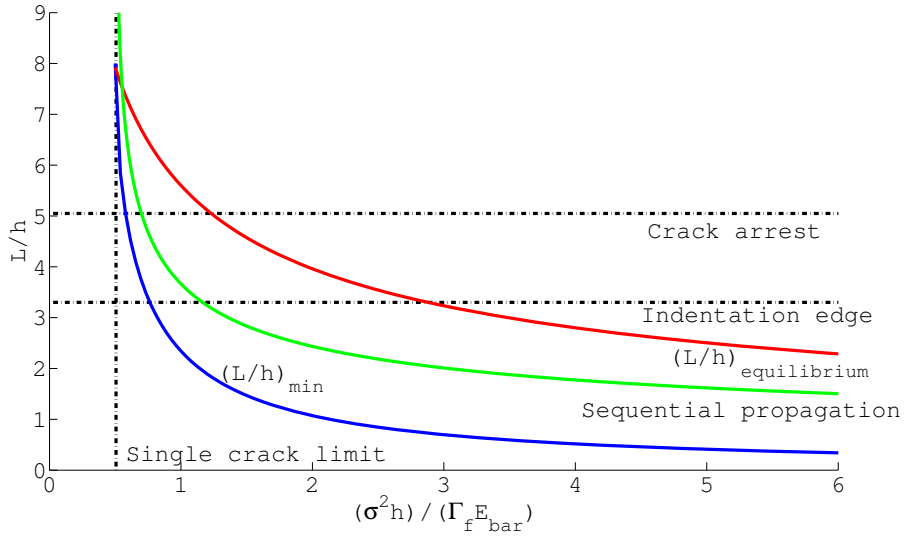

Figure 6.11: Crack spacing models plotted with the cracking limit for the TiN system

The crack driving force vs crack spacing is plotted for different values of the normalised residual stress t. It can be seen that an increasing value of t shifts the crack driving force curves to the right.

As explained in figure 4.13 and seen on figure 6.2, film cracking occurs when the driving force vs crack spacing plot is above and to the right of the cracking model graphs. For a crack pattern as seen on the pictures, the cracks are expected to initiate and arrest on the graph for the crack propagation model and in between the two endpoints to be in the area to the right and above the crack model graph. This is indicated as the "crack arrest regime" on figure 6.2. For the crack pattern plotted in figures 6.12-6.14, this behaviour is not clearly seen for any of the plotted residual stress values. The plot assumes that the cracks initiate at the indentation edge. Figure 6.15 shows figure 6.6 again. As seen, the cracks have initiated closer

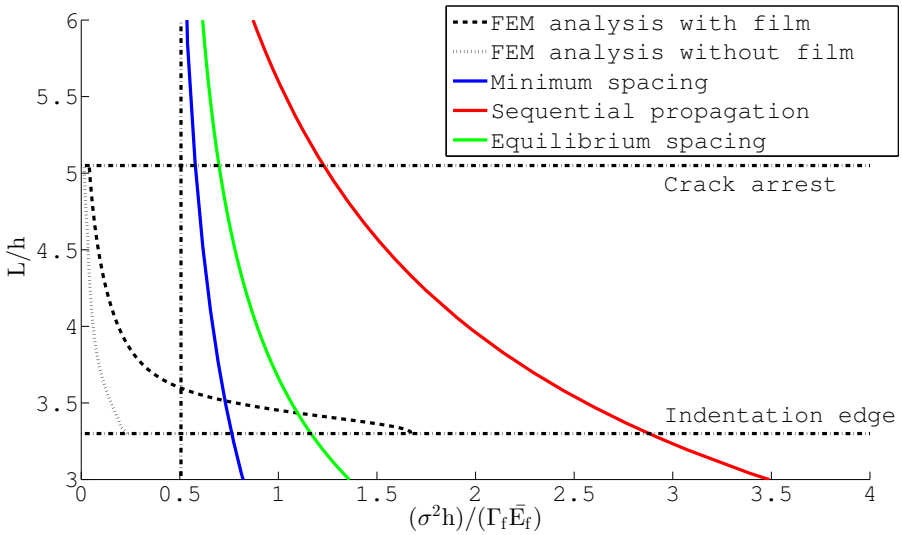

Figure 6.12: Normalised crack spacing as a function of normalised crack driving force for TiN-ASP23 system, , $t = 0$

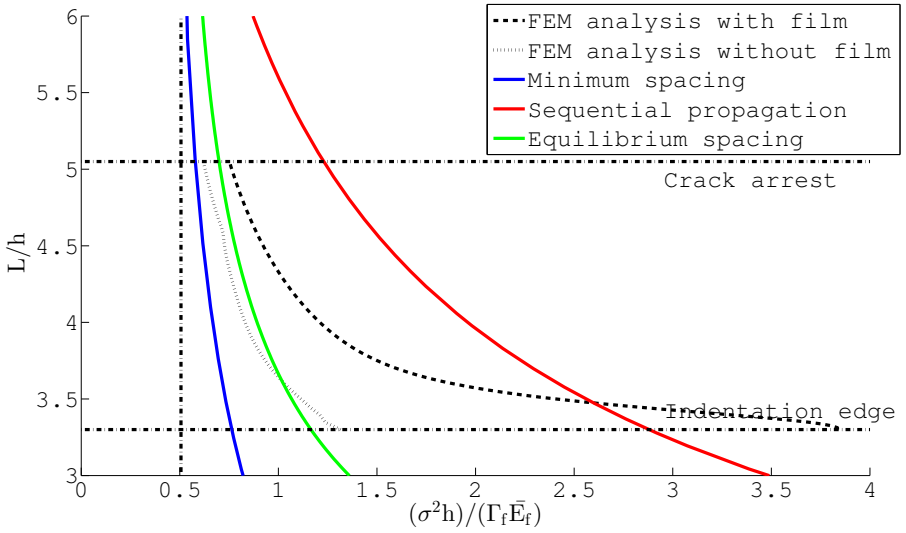

Figure 6.13: Normalised crack spacing as a function of normalised crack driving force for TiN-ASP23 system, , $t = 0.01$

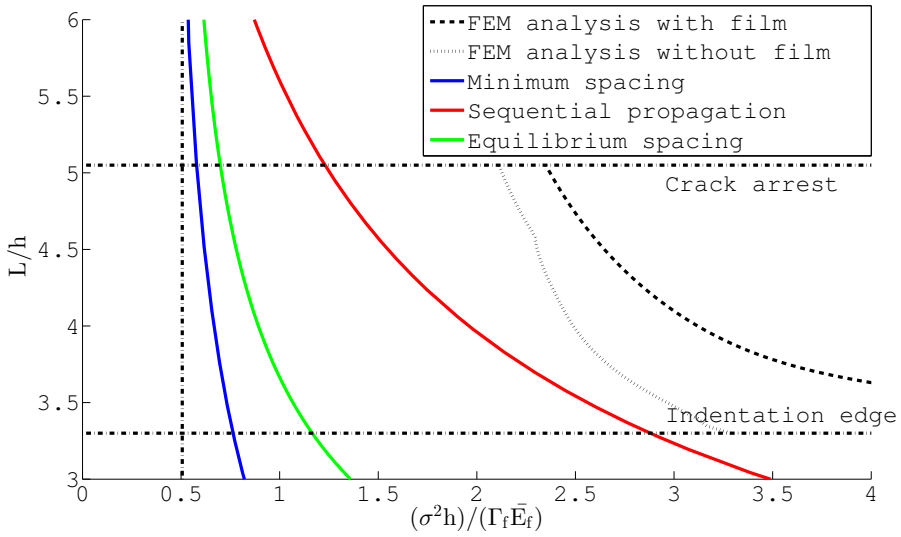

Figure 6.14: Normalised crack spacing as a function of normalised crack driving force for TiN-ASP23 system, , $t = 0.02$

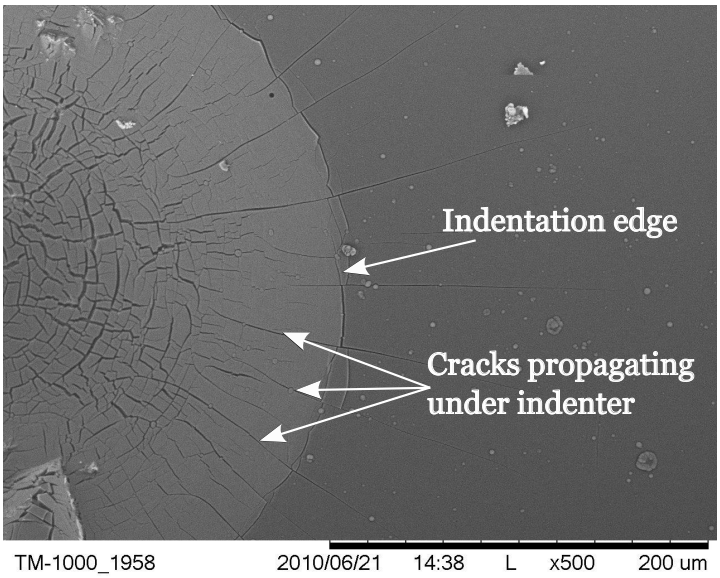

Figure 6.15: Crack propagating under indenter, Al_2O_3-AISI 316L system

to the indentation centre than the current indentation edge. When approaching the centre of the indentation crater, the crack pattern becomes disordered and reliable information of the crack pattern at this position is difficult. In the current analysis, the reliability of data for crack initiation is thus difficult to asses. This means that reliable data for the crack spacing vs crack driving force can only be obtained at crack termination and thus that the current analysis can only provide information of one of the two quantities, film residual stresses and the film fracture toughness. Residual stress must be determined in a separate analysis by e.g. a wafer bending test where the film is deposited on a thin wafer that bends under influence of the thin film residual stress (Freund and Suresh, 2004). For other film/-substrate systems however, the original assumption of crack initiation at the indentation edge may hold true and the general approach should not be discarded based on this one observation.

The information at crack termination can be used to determine the film fracture toughness. The crack driving force vs crack spacing information at crack termination can be seen as a point on the $L/h = L_1/h$ line plotted in figure 6.11 where the driving force vs crack spacing graphs intersect the L_1/h line.

In the current analysis, a fracture toughness value from the literature is used to construct the plot in order to visualise the analysis. Thus, the plot can be used to evaluate how accurately the model can predict the fracture toughness.

Not much difference is observed between the two types of film stress determination, (1) the direct FEM output from an analysis with film and (2) film stresses determined from equation 6.9 from substrate surface strains from an indentation without film. When approaching crack termination at $L/h = L_1/h$, the crack driving force plot for the two methods are virtually identical. The determined fracture toughness value for this analysis is dependent on the used crack propagation model. For the upper and lower bound for crack spacing shown here and a crack spacing of $L_1/h = 5.1$, the $(L/h)_{min}$ model predicts a crack driving force which is only 53% of the values predicted by the equilibrium crack spacing models which gives an upper bound. This is a large difference and more investigation into which model provides an accurate result is needed.

As described by (Beuth, 1992) for a single channelling crack and (Xia and Hutchinson, 2000) for crack arrays, elastic mismatch between film and substrate may have influence on the crack driving force. For The TiN-ASP23 system, $E_f/E_s = 1.4$. A system with a relative stiff film increases the channelling crack driving force (Beuth, 1992; Xia and Hutchinson, 2000). The elastic mismatch is expressed through the Dundur's parameters α and

β as described in section 4.1. For the TiN-ASP23 system, $\alpha = 0.17$ and $\beta = 0.044$. For a single crack, the elastic mismatch is described through the factor $g(\alpha, \beta)$ described in equation 4.12:

$$\mathcal{G}_{ss} = \frac{1}{2}\frac{\sigma^2 h}{\bar{E}_f}\pi g(\alpha, \beta) \tag{6.10}$$

For no elastic mismatch $\frac{1}{2}\pi g(\alpha, \beta) = 1.976$. Using linear interpolation on the tabulated values of $g(\alpha, \beta)$ from (Beuth, 1992) and assuming $\beta = 0$ gives $g = 1.42$ and $(1/2)\pi g(\alpha, \beta) = 2.24$. This is an increase in the crack driving force of 13%.

The influence of elastic mismatch on the interaction of parallel crack are described by (Xia and Hutchinson, 2000) through a characteristic length l, $l \equiv (\pi/2)g(\alpha, \beta)h$. The channelling crack driving force is the given equation 4.26:

$$\mathcal{G}_{ss} = \frac{l\sigma^2}{\bar{E}_f}\tanh\left(\frac{L}{2l}\right) \tag{6.11}$$

For no elastic mismatch, $l = 1.976h$ and for the TiN-ASP23 system $l = 2.24h$. Inserting these values in equation 6.11 at crack termination where $L_1 h = 5.05$ gives an increase in the crack driving force of 12%. Including this effect in the analysis would shift the crack model curves to the right and increase the determined film fracture toughness with the calculated 12%.

Residual stress also have a significant influence on the result. The residual stresses in the current TiN film are not given, but residual stresses in TiN films are typically compressive and in the range of $-0.006 < t < -0.0009$ (Höhl et al., 1992; Mogensen et al., 1998; Thomsen et al., 1998). This range for compressive stresses does not correspond very well to the fracture pattern seen in figure 6.11. Compressive stress decreases the crack driving force. In figure 6.11 the curves for small tensile ($t = 0.01$) and no ($t = 0$) residual stress lies to the left and below the cracking model curves and thus no cracking is predicted. This means that either is the proposed film fracture toughness value used to create the plot too high, or the FEM stress values is of too low magnitude. Using the current analysis to estimate the fracture toughness predicts a value of Γ_f in the range $4.9-10.5 J/m^2$. Accounting for the elastic mismatch increases this value with 12% to $\Gamma_f = 5.5 - 11.8 J/m^2$ corresponding to $K_{IC} = 1.3 - 2.0 MPa\sqrt{m}$. Values found in literature are in the range $4.51 - 7 MPa\sqrt{m}$ (Feng et al., 2005; Holmberg et al., 2003).

Al_2O_3

A plot similar to figure 6.11 is constructed for the Al_2O_3-AISI 316L system in figures 6.16-6.19. As previously described the plots are constructed using

the stresses from the FEM analyses shown in figures 6.9 and 6.10 and a literature value inserted for the fracture toughness Γ_f.

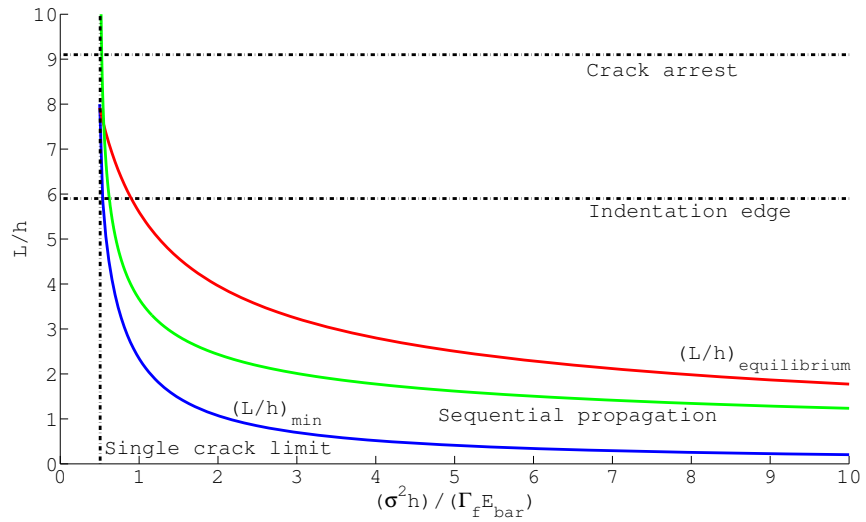

Figure 6.16: Crack spacing models plotted with the cracking limit for the Al_2O_3 system

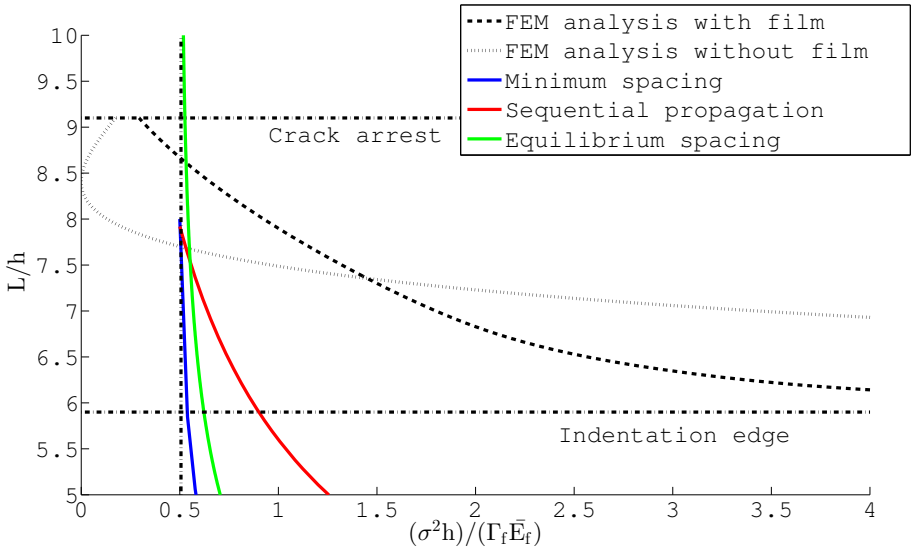

Figure 6.17: Normalised crack spacing as a function of normalised crack driving force for Al_2O_3-AISI 316L system, $t = -0.005$

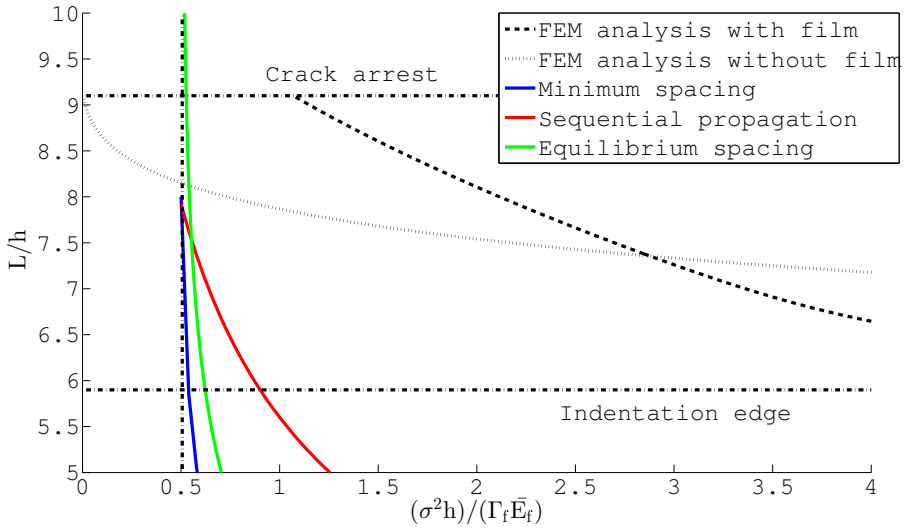

Figure 6.18: Normalised crack spacing as a function of normalised crack driving force for Al_2O_3-AISI 316L system, $t = 0$

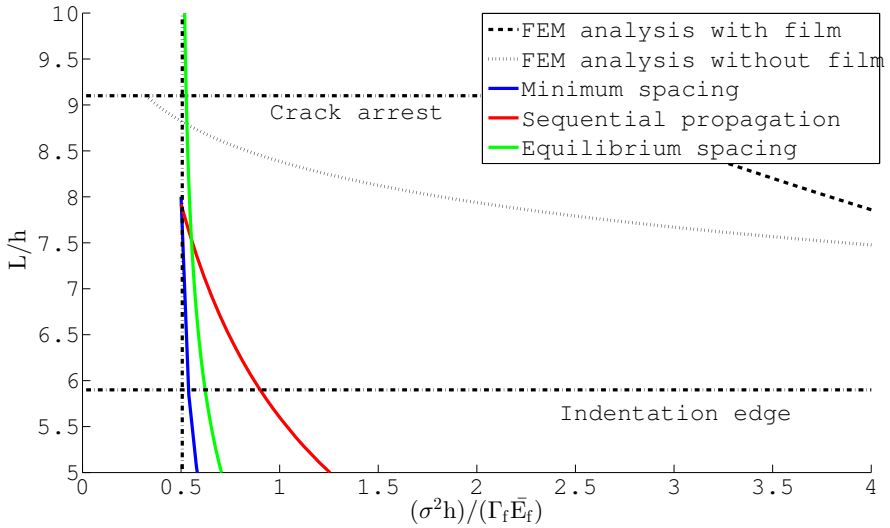

Figure 6.19: Normalised crack spacing as a function of normalised crack driving force for Al_2O_3-AISI 316L system, $t = 0.005$

As seen on figure 6.11 for the TiN system, the assumption of crack initiation at the indentation edge for the Al_2O_3system does not correlate with the theoretical models for crack propagation. Again, the cracks have initiated closer to the indentation edge than the current indentation edge and thus reliable information of crack initiation is difficult.

For the Al_2O_3 film crack pattern, the crack spacing at crack termination is $L_1/h = 9.1$. This is larger than the value of $L/h \approx 8$ that normally is given as the maximum spacing for which the cracks interact (Thouless, 1990). This means that the crack termination criteria here is given by the single crack driving force. The three plotted models for crack driving force vs crack spacing are also virtually equal to the single crack driving force line at $L/h \geq 8$. Thus focus is on the crack termination seen as the point where the crack driving force crosses the L_1/h line.

The results show good agreement with theory. For the plotted values for compressive or no residual stress, $t = -0.005$ and $t = 0$, the crack driving force curve coincides with the L_1/h line close to the expected single crack driving force limit point. The reasons for this much better agreement between the theory and the results are found in the same arguments used to explain the large difference for the TiN film. For the Al_2O_3-AISI 316L FEM analysis, a built-in material model for the AISI 316L substrate was available in the used FEM code. This material model includes the yield stress and the post-yield behaviour for the substrate. This indicates that the material response is more accurate than for the approximate value used for the ASP23 substrate. Also, the film Young's modulus is determined experimentally for the current film and is not a literature value, providing accurate input for this value as well. Finally, the used fracture toughness value Γ_f is found on an Al_2O_3-AISI 316L system similar to the currently analysed (Steffensen et al., 2013). This also indicate more accurate input for this value.

For a given value of t, the crack driving force is plotted for the film stress determined from an FEM analysis with film and one with film stresses determined from an FEM analysis without substrate. The two analyses differs more than it was the case for the TiN film. The reason for this is found in the FEM results. For the Al_2O_3 film, the analysis without film provides a higher peak value for the hoop stress $\sigma_{\theta\theta}$ giving a higher crack driving force close to the indentation crater. However, for the film-free analysis, $\sigma_{\theta\theta}$ decreases more rapidly than for the analysis with film. At crack arrest distance, the FEM analysis with film indicates higher value for $\sigma_{\theta\theta}$ and thus a higher driving force at crack arrest. This is different from the TiN film results where the crack driving force for the two cases were very similar also for smaller distance to the indentation edge. This

may be explained by the difference in the two material models used. The different post-yield material response used in the two models apparently have influence on the overall response of the two systems.

Figure 6.16 indicates that no or compressive residual stress of small magnitude is present in the film. Wafer bending tests on two Si wafers have shown that the analyses film is stress free to the accuracy of the used method (Madsen, 2010). Stainless steel has a larger thermal expansion coefficient than Si (Krex, 2007, p243), (Freund and Suresh, 2004, p94). This implies compressive residual stresses in the Al_2O_3-AISI 316L system as the steel substrate will contract more during cooldown after deposition. Since deposition parameters are not available here, this issue is not investigated any further. Though not quantified any further, compressive residual stresses in the film is a very plausible scenario.

Assuming no residual stresses in the film, the Al_2O_3 fracture toughness can be estimated to be $\Gamma_f = 190 J/m^2$ giving $K_{IC} = 6.4 MPa\sqrt{m}$ which is in very good correlation to the proposed literature value of $K_{IC} = 6.4 MPa\sqrt{m}$. Introducing compressive residual stress in the film will result in a higher estimated fracture toughness value. A value for the accuracy of the results is not given here, as the current experimental data are insufficient and further investigation is needed.

General remarks

A large difference in the accuracy of the results found for the TiN and the Al_2O_3 is observed. This is somewhat expected. The analysis of the TiN film is based on much less detailed information than the Al_2O_3 analysis. Young's modulus for the TiN film is found from literature since it is not given for the current film. Also, material data for the ASP23 substrate is estimated as a elastic-perfectly plastic material with yield strength given by a hardness value. Inaccurate material models for substrate and film may have significant influence on the determined film stresses. The film stress value is a quadratic factor in the crack driving for expression and thus an inaccuracy in the stress value is critical.

From the observations described above, it can be concluded that a correct substrate material model and correct thin film elastic data are crucial to obtaining a reliable result. If accurate data are available, the proposed Rockwell indentation crack pattern method may be a plausible and very useful method for determining thin film fracture toughness.

Chapter 7

Conclusion

The work of this thesis is focused on numerical analysis of indentation-induced stresses in thin films, analytical models for fracture and fracture patterns in thin films and the coupling of these two areas in order to estimate thin film fracture toughness. Numerous methods exist but the reliability of many of the methods are debatable and virtually all the method requires specially prepared samples or advanced equipment for the analysis.

During this study, a method to determine thin film fracture toughness from the radial crack pattern arising from the edge of a Rockwell indentation is developed and analysed. The method couples nonlinear FEM analysis of the indentation process with linear elastic models for the thin film crack pattern. A channel cracking and crack interaction criterion is used to determine the thin film fracture toughness.

The indentation problem and the stresses arising from the indentation has been treated. A number of theoretical solutions has been investigated. No theoretical solution that gives a precise picture of the stress state around the indentation is found. An FEM model is developed to examine the indentation process more thoroughly. The FEM model includes contact, large displacements, large strains and plasticity. For validation, the model is compared with a model from literature. The indentation process is simulated in two different cases. Firstly, an indentation of the substrate without film is simulated. The stress in the elastic region is found to be in good agreement with theoretical models. It is shown that this model does not give a realistic presentation of the circumferential stresses. A model for a film-substrate system with the film included in the FEM analysis is investigated. The influence of indentation depth on the accuracy of the results is analysed and no significant influence of indentation depth is found. For small indentation depths, film bending can have influence on the stress state through the thickness of the film. It is shown that film bending does not have in-

fluence on the results in the current analysis. It is shown that for constant indentation depth, the substrate yield strength has no influence on the film stresses. However, for a given indenter force, a higher yield strength causes lower indentation depths and thus lower film stresses.

A detailed description of the driving mechanisms and important parameters dictating the crack propagation is given. Mechanisms regarding delamination are briefly covered. A number of theoretical models for the propagation of parallel arrays of cracks are described and compared. The propagation of a crack from the film surface towards the film-substrate interface in analysed in detail. A number of factors are investigated in this analysis. For decreasing substrate yield strength, the crack driving force increases. This is due to the smaller constraint effect of the substrate. An effect of energy dissipation in the substrate plastic zone that would cause decreasing crack driving force is not seen. The effect of crack spacing on a crack depth vs driving force plot is investigated. This analysis includes substrate plasticity and the results differ from results for an elastic substrate. This shows that the smaller constraint from a plastically deformed substrate gives higher crack driving force for large crack spacings. For dense crack arrays, the plastic zone does not evolve as much and the influence of substrate plasticity is much smaller. Close to the crack the film is bent upwards. This effect is investigated. The results show that very close to the crack, the film surface is in compression, and for small crack spacings, new cracks are unlikely to initiate due to this effect. From the film bending analysis, a distance for which the film stress has recovered to its initial value is fund. This distance is compared to the simple shear-lag model for interface yielding. A large difference between these two results is seen.

The indentation model and the film cracking models are coupled to create a model for determining the thin film fracture toughness. The stresses given by the FEM indentation model are used as input for the crack array models investigated previously. The model is tested on two different film-substrate systems. One is a TiN film on an ASP23 tool steel. The other is a Al_2O_3 film on a AISI 316L stainless steel. A hypothesis for this analysis was, that both the thin film residual stress and fracture toughness could be determined. The cracks were thought to initiate at the indentation edge and thus a value for the crack driving force could be determined at two locations, at both crack initiation and crack arrest. The analysis indicates that in some systems, the cracks may initiate much closer to the indentation centre than the current indentation edge and thus reliable information of crack initiation is not available. This means that for the systems available for the current study, only fracture toughness or residual stress can be determined by the current method and not both of these as in the case when information at

crack initiation and arrest can be utilized. For other systems, the crack initiation mechanism may be different and the approach to also determine residual stress should not be rejected only based on the current results. The analysis shows very good results for the Al_2O_3 system while the results for the TiN system differs more from the expected. This is explained by the much more detailed information on the mechanical properties available for the Al_2O_3 system. For the TiN system, literature values for the film Young's modulus is used and the substrate material is assumed elastic-perfectly plastic. For the Al_2O_3 system, the Young's modulus is measured for the current film and a built-in material model for the substrate material is available.

The current thesis shows that the proposed method for determining thin film fracture toughness from the radial crack pattern arising from a Rockwell indentation of a film-substrate system has promising potential. However, the current experimental work is insufficient to give a final conclusion for the feasibility of this method. A comprehensive experimental study is necessary to investigate the initial findings more thoroughly.

Bibliography

Abdul-Baqi, A. and Van der Giessen, E. Numerical analysis of indentation-induced cracking of brittle coatings on ductile substrates. *International Journal of Solids and Structures*, 39(6):1427–1442, 2002.

Agrawal, D. C. and Raj, R. Measurement of the ultimate shear strength of a metal-ceramic interface. *Acta Metallurgica*, 37(4):1265–1270, 1989.

Ambrico, J. and Begley, M. The role of initial flaw size, elastic compliance and plasticity in channel cracking of thin films. *Thin Solid Films*, 419 (1-2s):144–153, 2002.

Atkins, A. G. and Tabor, D. Plastic indentation in metals with cones. *Journal of the Mechanics and Physics of Solids*, 13(1954), 1965.

Begley, M. R., Evans, A. G., and Hutchinson, J. W. Spherical impression of thin elastic films on elastic-plastic substrates. *International Journal of Solids and Structures*, 36(18):1662–1677, 1999.

Beuth, J. L. Cracking of thin bonded films in residual tension. *International Journal of Solids and Structures*, 29(13):1657–1675, 1992.

Beuth, J. L. and Klingbeil, N. W. Cracking of thin films bonded by elastic-plastic substrates. *Journal of the Mechanics and Physics of Solids*, 44(9): 1411–1428, 1996.

Biot, M. A. Bending of an infinite beam on an elastic foundation. *Journal of Applied Mechanics*, 4:1–8, 1937.

Biwa, S. and Storåkers, B. An analysis of fully plastic brinell indentation. *Journal of the Mechanics and Physics of Solids*, 43(8):1303–1333, 1995.

Bobji, M. S. and Biswas, S. K. Determination and study of the strength of the blister field generated by conical indentation. *Philosophical Magazine A*, 73(2):399–413, 1996.

Boussinesq, J. Application des potentials à l'etude de l'equilibre et du movement des solides élastiques. *Gauthier-Villars*, 45:108, 1885.

Chen, J. and Bull, S. J. Modelling the limits of coating toughness in brittle coated systems. *Thin Solid Films*, 517(9):2945–2952, 2009.

Cook, R. F. and Pharr, G. M. Direct observation and analysis of indentation cracking in glasses and ceramics. *Journal of the American Ceramic Society*, 73(4):787–817, 1990.

De Boer, M. P. and Gerberich, W. W. Microwedge indentation of the thin film fine line - I. Mechanics. *Acta Materialia*, 44(8):3169–3175, 1996.

De Guzman, M. S., Neubauer, G., Flinn, P., and Nix, W. D. The role of indentation depth on the measured hardness of materials. In *MRS Proceedings*, volume 308, pages 613–618. Cambridge Univ Press, 1993.

Delannay, F. and Warren, P. On crack interaction and crack density in strain-induced cracking of brittle films on ductile substrates. *Acta Metallurgica et Materialia*, 39(6):1061–1072, 1991.

Doege, E., Meyer-Nolkempe, H., and Saeed, I. *Fliesskurvenatlas metallischer Werkstoffe*. Hanser Verlag, 1986.

Drory, M. D. and Hutchinson, J. W. Measurement of the adhesion of a brittle film on a ductile substrate by indentation. *Proceedings of the Royal Society A: Mathematical, Physical and Engineering Sciences*, 452 (1953):2319–2341, 1996.

Dundurs, J. Effect of elastic constants on stress in a composite under plane deformation. *Journal of Composite Materials*, 1:310–322, 1967.

Dundurs, J. Edge-bonded dissimilar orthogonal elastic wedges under normal and shear loading. *Journal of Applied Mechanics*, 36:650–652, 1969.

Evans, A. G. and Charles, E. A. Fracture toughness determinations by indentation. *Journal of the American Ceramic Society*, 59(7-8):371–372, 1976.

Feng, W., Yan, D., He, J., Zhang, G., Chen, G., Gu, W., and Yang, S. Microhardness and toughness of the TiN coating prepared by reactive plasma spraying. *Applied Surface Science*, 243(1-4):204–213, 2005.

Fischer-Cripps, A. C., Lawn, B. R., Pajares, A., and Lanhua, W. Stress analysis of elastic-plastic contact damage in ceramic coatings on metal substrates. *Journal of the American Ceramic Society*, 79(10):2619–2625, 1996.

Flamant. *Compt. rend.*, 114:1465, 1892.

Fleck, N. A. and Hutchinson, J. W. Strain gradient plasticity. *Advances in Applied Mechanics*, 33:295–359, 1997.

Fleck, N. A., Muller, G. M., Ashby, M. F., and Hutchinson, J. W. Strain gradient plasticity: Theory and experiment. *Acta Metallurgica et Materialia*, 42(2):475–487, 1994.

Freund, L. B. and Suresh, S. *Thin film materials : Stress, defect formation and surface evolution*. Cambridge University Press, 2004.

He, M.-Y. and Hutchinson, J. W. Kinking of a crack out of an interface. *Journal of Applied Mechanics*, 56(2):270–278, 1989.

Hill, R. *The Mathematical Theory of Plasticity*. Oxford University Press, 1 edition, 1950.

Hill, R., Lee, E. H., and Tupper, S. J. The theory of wedge indentation of ductile materials. *Proceedings of the Royal Society of London. Series A*, 188(1013):273–289, 1947.

Hill, R., Storåkers, B., and Zdunek, A. B. A theoretical study of the brinell hardness test. *Proceedings of the Royal Society A: Mathematical, Physical and Engineering Sciences*, 423(1865):301–330, 1989.

Höhl, F., Stock, H.-R., and Mayr, P. Examination of residual stress, morphology and mechanical properties of sputtered TiN films. *Surface and Coatings Technology*, 54-55:160–166, 1992.

Holmberg, K. Tribological analysis of TiN and DLC coated contacts by 3d fem modelling and stress simulation. *Wear*, 264(9-10):877–884, 2008.

Holmberg, K., Laukkanen, A., Ronkainen, H., Wallin, K., and Varjus, S. A model for stresses, crack generation and fracture toughness calculation in scratched TiN-coated steel surfaces. *Wear*, 254(3-4):278–291, 2003.

Hu, M. and Evans, A. The cracking and decohesion of thin films on ductile substrates. *Acta Metallurgica*, 37(3):917–925, 1989.

Huang, J., Kim, B. C., Takayama, S., and Thouless, M. D. The control of crack arrays in thin films. *Journal of Materials Science*, 49(1):255–268, 2013.

Huang, Y., Gao, H., Nix, W. D., and Hutchinson, J. W. Mechanism-based strain gradient plasticity–II. Analysis. *Journal of the Mechanics and Physics of Solids Me*, 48:99–128, 2000.

Hutchinson, J. and Suo, Z. Mixed mode cracking in layered materials. *Advances in applied mechanics*, 29:63–191, 1992.

Jang, J. and Pharr, G. M. Influence of indenter angle on cracking in Si and Ge during nanoindentation. *Acta Materialia*, 56(16):4458–4469, 2008.

Jensen, H. M., Hutchinson, J. W., and Kim, K.-S. Decohesion of a cut prestressed film on a substrate. *International Journal of Solids and Structures*, 26(9):1099–1114, 1990.

Johnson, K. L. The correlation of indentation experiments. *Journal of the Mechanics and Physics of Solids*, 18:115–126, 1970a.

Johnson, K. L. The correlation of indentation experiments. *Journal of the Mechanics and Physics of Solids*, 18:115–126, 1970b.

Johnson, K. L. *Contact Mechanics*. Cambridge University Press, 1987.

Krex, H. E. *Maskin Ståbi*, volume 9. Nyt Teknisk Forlag, 2007.

Krueger, R. Virtual crack closure technique: History, approach and applications. *Applied Mechanics Reviews*, 57(2):109–143, 2004.

Li, X., Diao, D., and Bhushan, B. Fracture mechanisms of thin amorphous carbon films in nanoindentation. *Acta materialia*, 45(11), 1997.

Liechti, K. M. and Chai, Y. S. Asymmetric shielding in interfacial fracture under in-plane shear. *Journal of Applied Mechanics*, 59(2):295–304, 1992.

Lockett, F. J. Indentation of a rigid/plastic material by a conical indenter. *Journal of the Mechanics and Physics of Solids*, 11(5):345–355, 1963.

Ma, Q. and Clarke, D. R. Size dependent hardness of silver single crystals. *Journal of Materials Research*, 10:853–863, 1995.

Madsen, N. D. Microsopy pictures of rockwell indenation of an Al_2O_3-aisi316l film/substrate system. Aarhus University, unpublished work, 2010.

Malzbender, J. and de With, G. Modeling of the fracture of a coating under sliding indentation. *Wear*, 239(1):21–26, Apr. 2000.

Marshall, D. B. and Evans, A. G. Measurement of adherence of residually stressed thin films by indentation. I. Mechanics of interface delamination. *Journal of Applied Physics*, 56(10):2632, 1984.

McElhaney, K. W., Vlassak, J. J., and Nix, W. D. Determination of indenter tip geometry and indentation contact area for depth-sensing indentation experiments. *Journal of Materials Research*, 13(5):1300–1306, 1998.

Michel, M. D., Muhlen, L. V., Achete, C. A., and Lepienski, C. M. Fracture toughness, hardness and elastic modulus of hydrogenated amorphous carbon films deposited by chemical vapor deposition. *Thin Solid Films*, 496 (2):481–488, 2006.

Michler, J. Analysis of coating fracture and substrate plasticity induced by spherical indentors: Diamond and diamond-like carbon layers on steel substrates. *Thin Solid Films*, 381(1):119–134, 2001.

Møller, P. *Overfladeteknologi*. Ingeniøren|bøger, 1 edition, 2003.

Møller, P. and Pleth, L. P. *Advanced Surface Technology*. Møller & Nielsen, 1 edition, 2013.

Mogensen, K. S., Thomsen, N. B., Eskildsen, S. S., and Mathiasen, C. A parametric study of the microstructural , mechanical and tribological properties of PACVD TiN coatings. *Surface and Coatings Technology*, 99:140–146, 1998.

Moon, M.-W., Chung, J.-W., Lee, K.-R., Oh, K. H., Wang, R., and Evans, A. G. An experimental study of the influence of imperfections on the buckling of compressed thin films. *Acta Materialia*, 50(5):1219–1227, 2002a. Figure reprinted with permission from Elsevier.

Moon, M. W., Jensen, H. M., and Hutchinson, J. W. The characterization of telephone cord buckling of compressed thin films on substrates. *Journal of the Mechanics and Physics of Solids*, 50:2355–2377, 2002b. Figure reprinted with permission from Elsevier.

Marc Volume A. Theory and User Information. MSC.Software Corporation, www.mscsoftware.com, 2012.

Nakamura, T. and Kamath, S. Three-dimensional effects in thin film fracture mechanics. *Mechanics of Materials*, 13(1):67–77, Mar. 1992.

Nix, W. D. and Gao, H. Indentation size effects in crystalline materials: A law for strain gradient plasticity. *Journal of the Mechanics and Physics of Solids*, 46(3):411–425, 1998.

Oliver, W. C. and Pharr, G. M. An improved technique for determining hardness and elastic modulus using load and displacement sensing indentation experiments. *Journal of Materials Research*, 7(6):1564–1583, 1992.

Pharr, G. M. Measurement of mechanical properties by ultra-low load indentation. *Materials Science and Engineering: A*, 253(1-2):151–159, 1998.

Shenoy, V. B., Schwartzman, A. F., and Freund, L. B. Crack patterns in brittle thin films. *International journal of fracture*, 109(1):29–45, 2001.

Steffensen, S. and Jensen, H. M. Energy release rate for circular crack due to indentation in a brittle film on a ductile substrate. *European Journal of Mechanics - A/Solids*, 43:133–141, 2014.

Steffensen, S., Madsen, N. D., and Jensen, H. M. Numerical estimation of fracture toughness from indentation-induced circumferential cracking in thin films on ductile substrates. *International Journal of Solids and Structures*, 50(20-21):3406–3417, 2013.

Suo, Z. and Hutchinson, J. W. Interface crack between two elastic layers. *International Journal of Fracture*, 43:1–18, 1990.

Tabor, D. *The Hardness of Metals*. Oxford University Press, 1951.

Tada, H., Paris, P., and Irwin, G. *The Stress Analysis of Cracks Handbook*. ASME, 3 edition, 2000.

Thomsen, N. B. Microsopy pictures of rockwell indentation of various film/-substrate systems. Danfoss A/S, unpublished work, 1998.

Thomsen, N. B., Horsewell, A., Mogensen, K. S., Eskildsen, S. S., Mathiasen, C., and Bøttiger, J. Residual stress determination in PECVD TiN coatings by X-ray diffraction: A parametric study. *Thin Solid Films*, 333: 50–59, 1998.

Thouless, M. D. Crack spacing in brittle films on elastic substrates. *Journal of the American Ceramic Society*, 73(7):2144–2146, 1990.

Thouless, M. D., Olsson, E., and Gupta, A. Cracking of brittle films on elastic substrates. *Acta Metallurgica et Materialia*, 40(6):1287–1292, 1992.

Thurn, J. and Cook, R. F. Mechanical and thermal properties of physical vapour deposited alumina films part i thermal stability. *Journal of Materials Science*, 39(15):4799–4807, 2004.

Timoshenko, S. and Goodier, J. N. *Theory of elasticity*. McGraw-Hill, 3 edition, 1951.

Tvergaard, V. *Plasticity and creep in structural materials*. Technical University of Denmark. Department of Mechanical Engineering . Solid Mechanics, 2001.

VDI 3198. Verein Deutscher Ingenieure, August 1992.

Vidakis, N., Antoniadis, A., and Bilalis, N. The VDI 3198 indentation test evaluation of a reliable qualitative control for layered compounds. *Journal of Materials Processing Technology*, 143–144:481–485, 2003.

Wang, J. S., Sugimura, Y., Evans, A. G., and Tredway, W. K. The mechanical performance of DLC films on steel substrates. *Thin Solid Films*, 325:163–174, 1998.

Weppelmann, E. and Swain, M. V. Investigation of the stresses and stress intensity factors responsible for fracture of thin protective films during ultra-micro indentation tests with spherical indenters. *Thin Solid Films*, 286:111–121, 1996.

Whitehead, A. J. and Page, T. F. Nanoindentation studies of thin film coated systems. *Thin Solid Films*, 220(1-2):277–283, 1992.

Xia, Z. and Hutchinson, J. Crack patterns in thin films. *Journal of the Mechanics and Physics of Solids*, 48(6-7):1107–1131, 2000.

Yoffe, E. H. Elastic stress fields caused by indenting brittle materials. *Philosophical Magazine A*, 46(4):617–628, 1982.

Zak, A. R. and Williams, M. L. Crack point stress singularities at a bimaterial interface. *Journal of Applied Mechanics*, 30:142–143, 1963.

Zhang, S. and Zhang, X. Toughness evaluation of hard coatings and thin films. *Thin Solid Films*, 520(7):2375–2389, 2012.